Micro Energy Harvesting from Low-Frequency Vibrations
Towards Powering Pacemakers with Heartbeats

Blad, Thijs

DOI
10.4233/uuid:eeebed12-090f-4a4b-8450-d05a763fc9da

Publication date
2021

Document Version
Final published version

Citation (APA)
Blad, T. (2021). *Micro Energy Harvesting from Low-Frequency Vibrations: Towards Powering Pacemakers with Heartbeats*. [Dissertation (TU Delft), Delft University of Technology].
https://doi.org/10.4233/uuid:eeebed12-090f-4a4b-8450-d05a763fc9da

Important note
To cite this publication, please use the final published version (if applicable).
Please check the document version above.

MICRO ENERGY HARVESTING FROM LOW-FREQUENCY VIBRATIONS

TOWARDS POWERING PACEMAKERS WITH HEARTBEATS

MICRO ENERGY HARVESTING FROM LOW-FREQUENCY VIBRATIONS

TOWARDS POWERING PACEMAKERS WITH HEARTBEATS

Proefschrift

ter verkrijging van de graad van doctor
aan de Technische Universiteit Delft,
op gezag van de Rector Magnificus prof. dr. ir. T.H.J.J. van der Hagen,
voorzitter van het College voor Promoties,
in het openbaar te verdedigen op
donderdag 4 November 2021 om 12:30 uur

door

Thijs Willem Albert BLAD

Master of Science in Mechanical Engineering,
Technische Universiteit Delft, Nederland,
geboren te Oranjestad, Aruba.

Dit proefschrift is goedgekeurd door de promotoren.

Samenstelling promotiecommissie bestaat uit:

Rector Magnificus,	voorzitter
Prof. dr. ir. J.L. Herder,	Technische Universiteit Delft, promotor
Dr. ir. R.A.J. van Ostayen,	Technische Universiteit Delft, copromotor
Onafhankelijke leden:	
Prof. dr. ir. A. van Keulen,	Technische Universiteit Delft
Prof. dr. ing. H. Vallery,	Technische Universiteit Delft
Prof. dr. S.P. Magleby,	Brigham Youngs University, Verenigde Staten
Dr. ir. M. Schenk,	University of Bristol, Verenigd Koninkrijk
Prof. dr. P.G. Steeneken,	Technische Universiteit Delft, reservelid
Overig lid:	
Dr. N. Tolou,	Flexous Mechanisms, Industry supervisor

Keywords: Vibration energy harvesting, Compliant mechanisms, Buckling
Printed by: Repro van de Kamp
Front & Back: Marit van de Kamp

ISBN 978-94-6366-468-4

An electronic version of this dissertation is available at
http://repository.tudelft.nl/.

“How often I found where I should be going only by setting out for somewhere else.”

Richard Buckminster Fuller

CONTENTS

SUMMARY

Miniaturized vibration energy harvesters can provide an alternative to batteries in powering the billions of low power devices we use today by extracting power from ambient motion. Especially for implanted medical devices, these alternative power sources may be an attractive option to overcome the limitations on longevity and the replacement costs and inconvenience that result from the use of batteries.

Devices based on piezoelectric transducers were found to be especially suited for this purpose due to their high energy densities, miniaturization capabilities and ease of implementation. However, the application of these devices in environments where the ambient motion contains mostly low-frequency vibrations has proven to be difficult due to the inherent stiffness of the piezoelectric material. As there are many sources of these low-frequency motions, including human motion, the development of a method to design energy harvesters for these environments would have large commercial potential and great opportunities for future exploitation.

Therefore, the main objective of this thesis is to develop an effective strategy for vibration energy harvesting from low-frequency motion. Formulating a clear strategy allows us to provide perspective on the current state-of-the-art, and a focus for the future research directions of the field. The second objective is to develop the enabling technologies necessary to implement this strategy in miniaturized applications.

The approach assumed in this thesis is to apply the principle of stiffness compensation to offset the stiffness of piezoelectric energy harvesters. Compliant ortho-planar mechanisms were identified as the most promising embodiment for the design of miniaturized piezoelectric energy harvesters. In order to combine this embodiment with the method of stiffness compensation, new mechanism designs will be developed. Finding a reliable and repeatable method to introduce the required preloading at small scales was identified as one of the key challenges.

This initially resulted in the design of three mechanisms that are the most simple topologies for which stiffness compensation could be achieved in compliant ortho-planar mechanisms. The designs consist of beams with wide and narrow sections and it was demonstrated that their stiffness could be tuned by manipulating the relative lengths of these sections. This result provided an initial validation of the approach taken in this thesis and inspired further development. These designs were used to develop the miniaturized energy harvesters. In these devices, the mechanical designs were implemented in flexible piezoelectric transducers that were fabricated using micro-machining processes. The resulting energy harvesters

demonstrated near zero-stiffness characteristics and were able to harvest energy from a low-frequency actuation. To address the challenge of preloading at small scales, a method called package induced preloading was developed.

Further development of the designs yielded the mechanisms in which the stiffness could be almost completely compensated which resulted in the first statically balanced compliant ortho-planar mechanism. This mechanism was implemented in a piezoelectric vibration energy harvester where it compensated the stiffness of a piezoceramic transducer. The energy harvester demonstrated a relevant efficiency when excited by a low-frequency motion of sub 1 Hz. This shows that stiffness compensation can be used to develop miniaturized vibration energy harvesters for low-frequency motion.

SAMENVATTING

Micro vibration energy harvesters zijn geminiaturiseerde apparaten waarmee op kleine schaal energie opgewekt kan worden uit trillingen. Deze systemen bieden een alternatief voor batterijen om de miljarden draadloze apparaten die we vandaag de dag gebruiken van stroom te voorzien. Met name voor geïmplanteerde medische apparaten kunnen deze alternatieve stroombronnen een aantrekkelijke optie zijn vanwege de beperkte levensduur en de hoge vervangingskosten van batterijen.

Apparaten op basis van piëzo-elektrische transducers zijn bijzonder geschikt voor deze toepassing door hun hoge energiedichtheden, miniaturisatiemogelijkheden en eenvoudige implementatie. De toepassing van deze apparaten in een omgeving waar de bewegingen voornamelijk laagfrequente trillingen bevat, is echter moeilijk vanwege de stijfheid van het piëzo-elektrische materiaal. Aangezien er veel praktische toepassingen zijn waarin we deze laagfrequente bewegingen vinden, waaronder menselijke beweging, zou de ontwikkeling van een manier om energy harvesters voor juit deze omgevingen te ontwikkelen een groot commercieel potentieel hebben.

Het hoofddoel van dit proefschrift het ontwikkelen van een effectieve strategie voor het opwekken van energie uit deze laagfrequente bewegingen. Het formuleren van een duidelijke strategie stelt ons in staat om de huidige oplossingen in perspectief te plaatsen en een focus te bieden voor de toekomstige onderzoeksrichtingen binnen dit vakgebied. Het tweede doel is om de technologieën te ontwikkelen die nodig zijn om deze strategie in geminiaturiseerde toepassingen te implementeren.

Om deze doelen te behalen wordt een aanpak voorgesteld om de stijfheid van piëzo-elektrische materiaal te compenseren door middel van compliante mechanismen met een negatieve stijfheid. Compliante ortho-planaire mechanismen zijn geïdentificeerd als het meest geschikte type compliante mechanismen voor de ontwikkeling van de piëzo-elektrische energy harvesters op microschaal. Om dit type mechanisme te combineren met de voorgestelde stijfheidscompensatie zullen nieuwe methodes moeten worden ontwikkeld. Het vinden van een betrouwbare en herhaalbare methode om de vereiste voorspanning op microschaal te introduceren is een van de belangrijkste uitdagingen.

Dit resulteerde aanvankelijk in drie nieuwe ontwerpen waarin stijfheidscompensatie kan worden toegepast binnen een zo eenvoudig mogelijke configuratie. De ontwerpen bestaan uit een enkele ligger waarin brede en smalle segmenten elkaar afwisselen. Door te spelen met de lengtes van de brede en smalle segmenten kon de stijfheid van het systeem worden

gecompenseerd. Dit resultaat zorgde voor een eerste validatie van de aanpak van dit proefschrift en inspireerde tot verdere ontwikkeling. In de volgende stap werden micro energy harvesters ontwikkeld door de ontworpen mechanismen te implementeren in flexibele piëzo-elektrische transducers die werden vervaardigd met microfabricage. De energy harvesters vertoonden een grote mate van stijfheidscompensatie en waren in staat om energie te oogsten uit een laagfrequente actuatie. Om de uitdaging van het voorspannen op microschaal te overwinnen, werd een methode ontwikkeld die package induced preloading wordt genoemd.

Verdere ontwikkeling leverde wederom nieuwe ontwerpen op voor mechanismen waarin de stijfheid volledig kan worden gecompenseerd. Als resultaat hiervan beschrijft dit proefschrift het eerste statisch gebalanceerde compliante ortho-planaire mechanisme ter wereld. Dit mechanisme werd geïmplementeerd in een energy harvester waar het de stijfheid van een piëzokeramische transducer compenseerde. De energy harvester demonstreerde een relevante efficiëntie wanneer deze werd aangedreven middels een laagfrequente beweging van minder dan 1 Hz. Dit toont aan dat stijfheidscompensatie kan worden gebruikt om micro energy harvesters te ontwikkelen voor laagfrequente bewegingen.

PREFACE

This thesis is aimed at the development of mechanical designs of miniaturized vibration energy harvesters for low-frequency motion, and the chapters of this thesis outline the critical path of this development. The chapters present the research activities that follow the proposed approach to address the objectives laid out for this study in a roughly chronological order. The chapters are relatively self-contained and can be read individually as they were originally prepared as individual articles. Chapters two, three, four and five present published or accepted work of which the manuscripts have only been reformatted to correct grammatical errors and fit the layout of the thesis. Chapter six, which outlines a methodology to generate and replicate heartbeat motion signals in the lab, is to be submitted to a future conference. Chapter seven presents ongoing work on the design and simulation of a MEMS demonstrator and is intended to be submitted once the MEMS prototypes have been fabricated and tested.

Besides the research activities reported in the chapters of this thesis, various other projects have been undertaken which are related to the work of this thesis.A graphical overview of all projects and publications related to this thesis is shown in Figure 1 on the next pages. Energy harvesting research at the Department of Precision and Microsystems Engineering started already in 2011 but remained limited to only a handful of M.Sc. projects up to 2017. Over the course of this study, the research efforts in this direction were increased significantly through many projects that originated from the ideas outlined in this thesis. From 2017 onward, the depicted M.Sc. and B.Sc. projects have been initiated and supervised by the author of this thesis. A number of these projects have yielded publications that are not included as chapters in this thesis. Instead, they are listed together with the M.Sc. theses and the B.Sc. reports in the thesis project output at the end of this thesis.

The work presented in the chapters of this thesis is to be attributed to the author, unless stated otherwise. Such is the case in chapters four and six, where part of the work was carried out by others. Chapter four resulted from a collaboration project and in chapter six work from a graduation project was combined with work from the author. Throughout the whole thesis, acknowledgments of contributions by others and references to work of others have been included as consciously as possible.

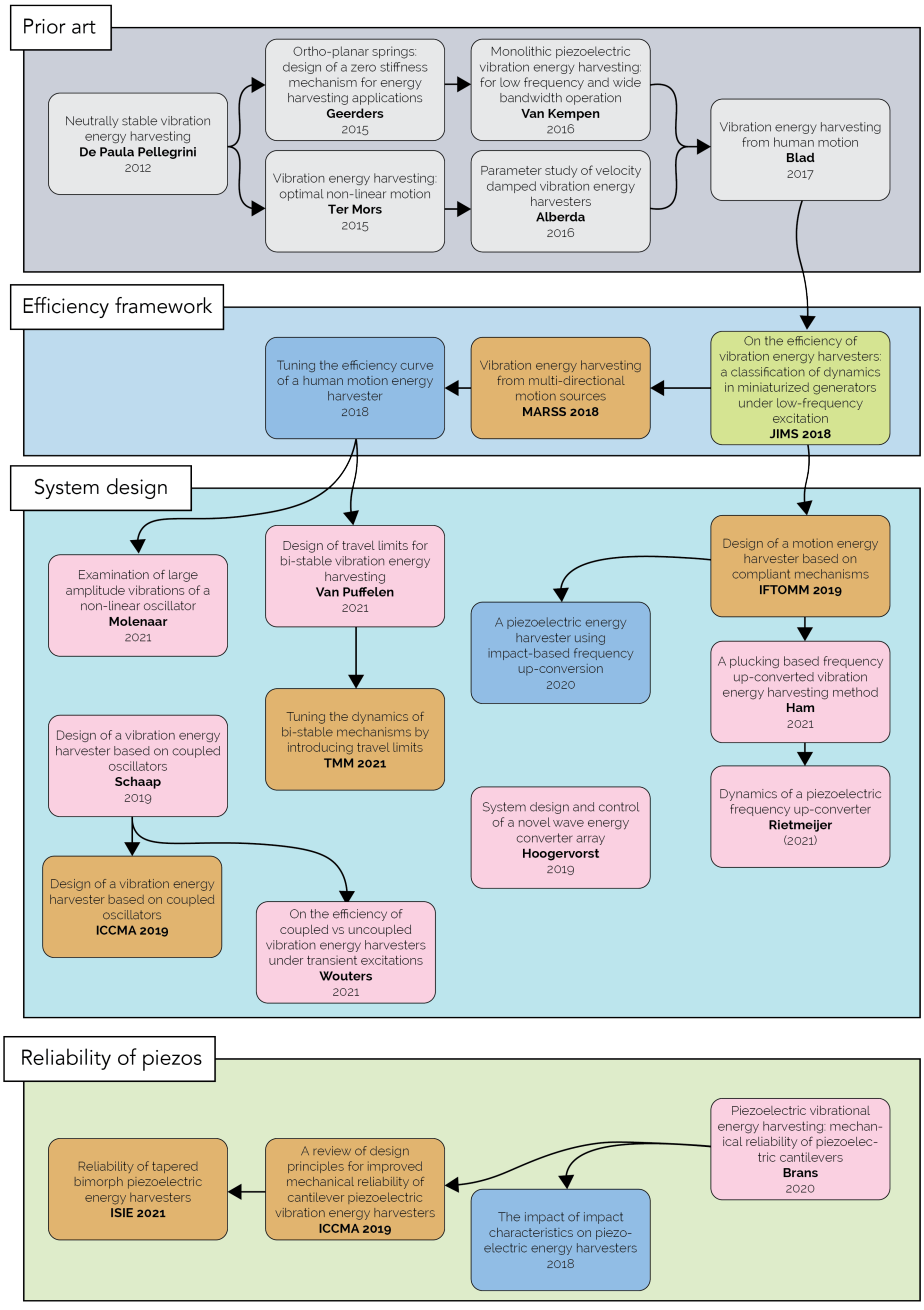
Prior art
Neutrally stable vibration energy harvesting
De Paula Pellegrini
2012
Ortho-planar springs: design of a zero stiffness mechanism for energy harvesting applications
Geerders
2015
Vibration energy harvesting: optimal non-linear motion
Ter Mors
2015
Monolithic piezoelectric vibration energy harvesting: for low frequency and wide bandwidth operation
Van Kempen
2016
Parameter study of velocity damped vibration energy harvesters
Alberda
2016
Vibration energy harvesting from human motion
Blad
2017
Efficiency framework
On the efficiency of vibration energy harvesters: a classification of dynamics in miniaturized generators under low-frequency excitation
JIMS 2018
Vibration energy harvesting from multi-directional motion sources
MARSS 2018
Tuning the efficiency curve of a human motion energy harvester
2018
System design
Design of a motion energy harvester based on compliant mechanisms
IFTOMM 2019
A piezoelectric energy harvester using impact-based frequency up-conversion
2020
A plucking based frequency up-converted vibration energy harvesting method
Ham
2021
Dynamics of a piezoelectric frequency up-converter
Rietmeijer
(2021)
Design of travel limits for bi-stable vibration energy harvesting
Van Puffelen
2021
Examination of large amplitude vibrations of a non-linear oscillator
Molenaar
2021
Tuning the dynamics of bi-stable mechanisms by introducing travel limits
TMM 2021
Design of a vibration energy harvester based on coupled oscillators
Schaap
2019
System design and control of a novel wave energy converter array
Hoogervorst
2019
Design of a vibration energy harvester based on coupled oscillators
ICCMA 2019
On the efficiency of coupled vs uncoupled vibration energy harvesters under transient excitations
Wouters
2021
Reliability of piezos
Piezoelectric vibrational energy harvesting: mechanical reliability of piezoelectric cantilevers
Brans
2020
A review of design principles for improved mechanical reliability of cantilever piezoelectric vibration energy harvesters
ICCMA 2019
Reliability of tapered bimorph piezoelectric energy harvesters
ISIE 2021
The impact of impact characteristics on piezoelectric energy harvesters
2018

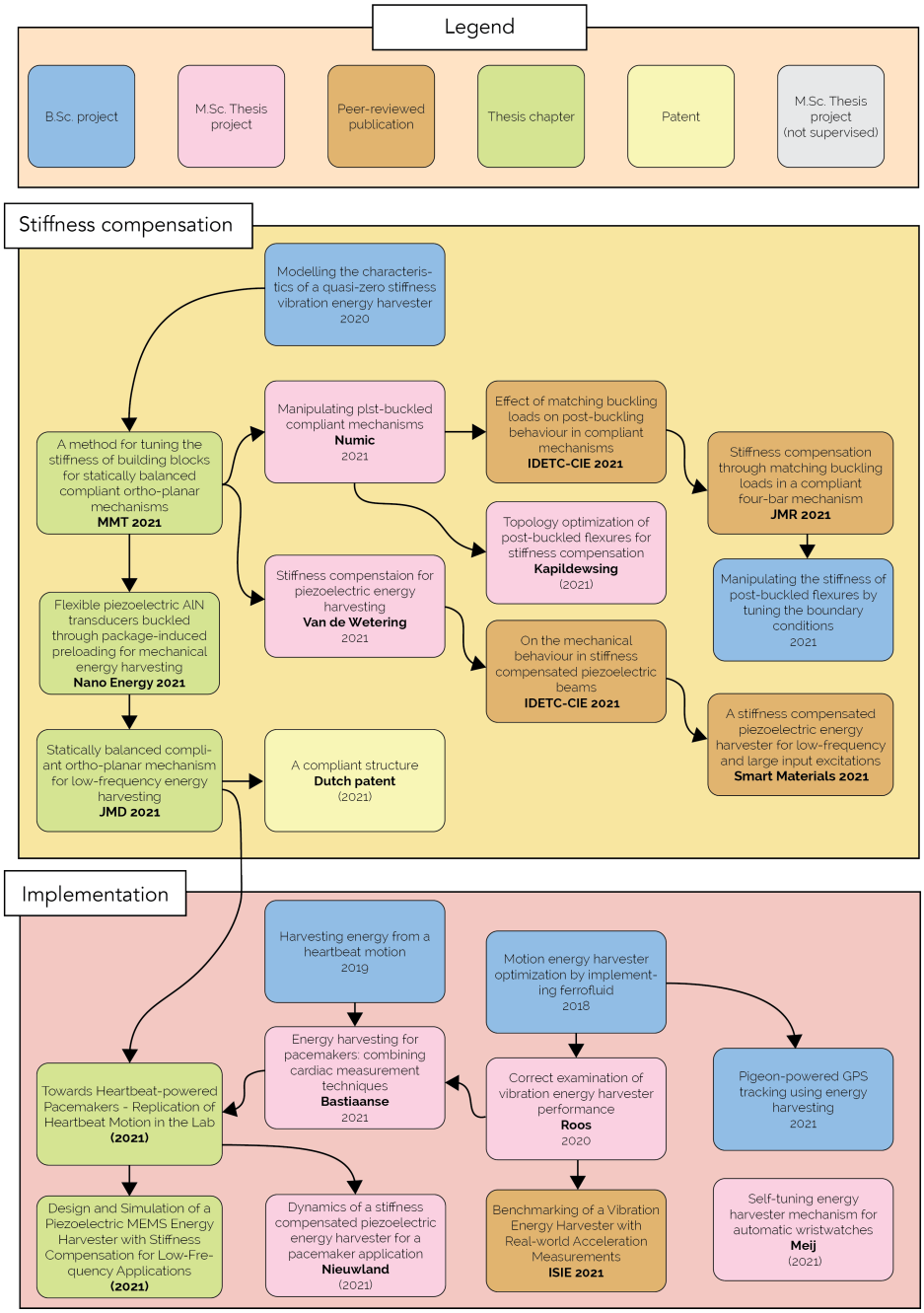

Figure 1: Graphical overview of the different projects and publications related to this thesis. From 2017 onward, the depicted B.Sc. and M.Sc. thesis projects have been supervised by the author of this thesis; M.Sc. theses are presented with the name of the author; a date between brackets indicates the work is yet to be published. All projects and publications are listed in the thesis project output at the end of this thesis.

1 INTRODUCTION

This chapter introduces the reader to vibration energy harvesting by providing a perspective on the motivation and possible applications of the technology. The development of miniaturized generators for low-frequency applications is introduced as the focus of this study, the challenges are identified and an approach based on the design of stiffness compensation in compliant ortho-planar mechanisms is presented. The research objective and goals of the thesis are defined and the structure of this thesis is outlined.

1.1 MOTIVATION AND APPLICATION

> *If you want to find the secrets of the universe, think in terms of energy, frequency and vibration.*
>
> Nikola Tesla

Billions of wireless electronic devices are currently powered by batteries. In many of these cases, batteries dominate the size, limit the lifetime, and introduce significant maintenance costs when they have to be replaced. Besides costs, battery replacement may otherwise be undesirable due to risks or regulations. For instance, implanted pacemakers typically last around seven years, and the surgery required to replace the batteries incurs not only great costs but also considerable risks [1, 2]. Great improvements in miniaturization and longevity can be achieved if we can overcome the limitations of batteries by using alternative power sources.

Recent advances have led to considerable reductions in size and power consumption for electronic circuits, such that power sources such as energy harvesting may be considered as a suitable alternative to batteries. Energy harvesting encompasses all process by which energy is extracted from ambient sources is a field that has been receiving great interest as a potential inexhaustible source for low-power devices. These ambient sources are light, radio-frequency electromagnetic radiation, thermal gradients and motion and while each application should be evaluated individually to find the best energy-harvesting method, the general opinion from the literature is that kinetic energy in the form of motion or vibration is generally the most versatile and ubiquitous ambient energy source available [3]. The systems that aim to derive power from this source are grouped by the term vibration energy harvesters, and these systems are the topic of this thesis. The main focus is the development of effective, miniaturized vibration energy

harvesting system in applications where the vibration environment contains mostly low-frequency motion.

The study is motivated by the limitations of batteries imposed on implanted medical devices such as pacemakers, where longevity considerations demand the trade-off between device size and the need for replacement surgeries [4]. As an example, the leadless pacemaker is considered, a recent development in pacemaker technology. The self-contained device is up to 90% smaller than traditional systems and can be implanted directly into the right ventricle, which offers great advantages in terms of placement procedure and lowers the risk of several complications [5]. However, the smaller size comes at the cost of battery capacity and therefore the leadless pacemaker is currently only feasible for a limited range of pacing capabilities. In this application, a convincing case can be made for energy harvesting as the beating of the heart consistently provides ambient motion which can be harvested to power the pacemaker [6]. Moreover, as this power source is virtually inexhaustible, it could allow the development of pacemakers that last a lifetime.

Other significant applications are wireless sensor networks comprised of numerous small wireless nodes that can be deployed into an environment to collect and transmit information [7, 8]. In areas such as structural health monitoring [9], environmental and machinery condition monitoring [10–12], precision agriculture [13], and healthcare [14] these networks can be applied to cut costs, increase productivity and improve safety. However, powering the self-contained nodes remains one of the major challenges limiting the practical implementation of these networks, especially when the nodes are positioned at inaccessible or dangerous locations and in harsh environments. For many of these applications, vibration energy harvesting may provide a suitable alternative power source to overcome these challenges [15].

Effective application of vibration energy harvesters requires the systems to be susceptible to the ambient motion [16]. Typically, the ambient motion is dissected using spectral analysis such that the frequency and power of the vibrations that make up the motion can be identified, and the energy harvester can be designed accordingly. Real-world vibration environments are generally characterized by mostly low-frequency content of up to 100 Hz, and many desirable applications such as human motions contain mostly frequencies below 10Hz [3, 17, 18]. Moreover, in the real world, vibration environments are rarely constant and both their frequency content as well as their power may change over time [19, 20]. As a result, vibration energy harvesters may suffer from variable and unpredictable levels of available power [21]. The main problem related to miniaturization of vibration energy harvesting for low-frequency applications is governed by the scaling laws of the dynamics of these devices [22]. When the oscillators are scaled down, their masses scale down at an increased rate compared to their stiffness, and their natural frequencies increase. As a result, these miniaturized devices can

quickly become unresponsive to the incoming vibrations and lose effectiveness. Therefore, the main challenge in the design of a miniaturized energy harvester for real-world applications is to enable the device to respond to low-frequency motion without the need for large attached masses.

1.2 APPROACH

> *"The real voyage of discovery consists not in seeking new landscapes, but in having new eyes."*
>
> Marcel Proust

This section will present the approach taken in this thesis by outlining three desired properties of the vibration energy harvester: efficient, applicable to low-frequency motion, and miniaturized. First, the evaluation of performance in vibration energy harvesters will be discussed together with methods to achieve high efficiencies. Next, the idea of leveraging compliant mechanisms to compensate the inherent stiffness of structures, and thereby allow harvesting from low-frequency motion, will be outlined. Last, ortho-planar mechanisms will be presented as the most promising embodiment for implementation at small scales.

EVALUATING AND ACHIEVING EFFICIENCY

The efficiency of a vibration energy harvester describes how well it can transform mechanical energy in the form of motion or vibration into useful electrical output power. This generally involves a chain of processes that can be generalized in the following steps. First, energy is extracted from the driving motion and stored in the system as kinetic or potential energy. Next, a transducer is used to convert the kinetic or potential energy into electrical energy, and finally the electrical energy is conditioned and stored such that it can be used as a power source. Achieving a high efficiency requires the optimization of each step in the chain and is therefore a multidisciplinary challenge [23].

A very important design choice is the selection of the *transducer*, which is the embodiment of one or more physical processes that convert the mechanical vibrations to electrical power. Of all the transduction processes, piezoelectricity [1] has received the greatest attention in research and is generally considered to be the most promising transduction process for miniaturized vibration energy harvesting devices. The main reasons for this

[1] Piezoelectricity is a form of coupling between the mechanical and the electrical domains that is observed in specific crystals, ceramics and polymers. The coupling consists of the *piezoelectric effect*, which describes the phenomenon in which an electrical charge is induced on the material surface due to mechanical stress, and the inverse piezoelectric effect, which describes the phenomenon in which strain is induced in response to an applied electric field.

are the large power densities, miniaturization capabilities and ease of application [24, 25]. For these reasons, the approach taken in this thesis is to focus on the use of piezoelectric transducers.

An important notion adopted in this thesis is that there is no absolute way to address the efficiency of a vibration energy harvester. In the most general sense, the efficiency could be defined as the portion of input energy that is returned as a useful output of the system. In vibration energy harvesters this quantity could be found by measuring the electrical output and comparing it to the total work done on the system by the driving motion. However, such a metric would only give us information how well the energy that has entered the system is being used (i.e. the second and third step in the chain) and it does not provide information on how well the system is able to capture energy from the driving motion. For example, a system with an eigenfrequency close to the frequency at which a driving motion is applied, may capture a lot more energy from this motion compared to a system with a much higher or lower eigenfrequency.

Finding a metric to address the efficiency of the first step, which means finding the energy that could have been captured from a particular motion, results in the following under-defined problem. The driving motion is often assumed to be unaffected by the dynamics of the energy harvester and can therefore (theoretically) supply an infinite amount of power. A popular approach to solving this problem is the adoption of figures of merit in which the actual power output is compared to that of an imaginary (optimized) device which operates under the same set of boundary conditions [3, 16, 26–28]. However, the underlying assumptions on which these optimized devices are constructed may not be relevant for all operating conditions. For example, in the cases where the amplitude of the driving motion exceeds the size of the device, infeasibly large amounts of damping may be required [16]. Such figures of merit should therefore never be considered as absolute scales on which efficiencies can be evaluated, but merely as gold standards on which performance can be benchmarked.

HARVESTING LOW-FREQUENCY MOTION

The field of compliant mechanisms encompasses the mechanisms that achieve force and motion transmission through the deflection of flexible members [29, 30]. Compared to rigid link mechanisms, which consist of rigid members connected through joints, compliant mechanisms offer the following main advantages. They can be fabricated as single-piece (i.e. monolithic) structures, which greatly reduces the number of parts, enables the use of new production processes and allows them to be fabricated at small scales [31, 32]. Moreover, due to the lack of friction and play, compliant mechanisms have a better mechanical efficiency, reliability and precision [33]. Furthermore, compliant mechanisms allow for a very natural integration with piezoelectric material because the mechanical stresses can be designed to be spread out over large areas of the mechanism. As a result, a

lot of piezoelectric material can be deformed which allows for the design of energy harvesters that very efficiently use their volume.

However, a drawback of compliant mechanisms is their inherent stiffness, a property which describes the extent to which the mechanism resists deformation. Due to this stiffness, the mechanisms may require large forces to achieve the desired range of motion. During this motion a significant part of the input energy is stored as strain energy in the deforming flexible members, and is thus not used for the intended function of the mechanism [34]. Moreover, the best piezoelectric materials are inflexible ceramics and their integration further increases the stiffness [35]. As a result, piezoelectric energy harvesters are often only applied in environments with high-frequency vibrations.

In order to overcome this problem, the stiffness of the mechanism may be reduced by compensating the stored strain energy by releasing strain energy in another part of the mechanism. This principle is known as stiffness compensation, and it requires an initial portion of energy to be introduced in the mechanism through a process called preloading [36]. During motion, this energy flows from the preloaded parts to the deforming parts of the mechanism such that less input energy is required compared to an uncompensated system. Moreover, when stiffness compensation is designed such that the total potential energy in a mechanism remains constant, such a mechanism can be called *statically balanced* and has the property that it demonstrates zero-stiffness behavior [37].

The approach assumed in this thesis is to apply the principle of stiffness compensation to offset the stiffness of piezoelectric energy harvesters. Adopting this approach should lead to the following two favorable outcomes. The first outcome is that it allows piezoelectric energy harvesters to be designed for low-frequency motion, enabling new applications. The second outcome is that it provides a tuning parameter for the coupling factor of existing piezoelectric transducers. The coupling factor indicates how effective a piezoelectric transducer converts applied mechanical energy into electrical energy, and a high coupling factor is usually desirable for applications where the unconverted energy cannot be easily recovered [38, 39]. If the stiffness of the transducer can be fully compensated, this coupling factor could theoretically approach unity. As a result, all applied mechanical energy can be converted into electrical energy.

MINIATURIZATION OF ENERGY HARVESTERS

As energy harvesters are to be applied in miniaturized applications, they must be able to be produced at small scales. For this purpose, microfabrication processes for micro-electromechanical systems (MEMS) can be leveraged and for many piezoelectric materials, standardized processes are already available [40, 41]. In this way, miniaturized energy harvesters can be fabricated in which the mechanical components, transducer and power electronics for conditioning and storage are integrated

[42, 43]. Moreover, as piezoelectric transducers allow for monolithic micro-scale systems, the cost of these devices to be sufficiently low for mass scale deployment [25].

However, the planar nature of the microfabrication methods comes with two significant challenges related to the design of the energy harvester. First, the mechanical elements that make up the oscillating mechanism must be fabricated from a single plane which greatly limits the feasible designs to planar mechanisms only. Secondly, the deposition of piezoelectric material is limited to this plane as well. While it might in theory be possible to develop processes to deposit piezoelectric material on the sidewalls of a structure, this is not possible with current microfabrication methods of piezoelectric transducers. As a result, it is difficult to effectively deform large areas of piezoelectric material with in-plane motion. Therefore, the desired mode of operation for these mechanisms is in a direction out-of-plane.

Mechanisms that fit both these constraints are identified as ortho-planar mechanisms [44, 45]. Besides their natural compatibility with the microfabrication processes, these mechanisms have the advantage that they can be very compact. Moreover, compared to in-plane mechanisms they allow for a larger range of motion as their parts do not collide with each other. Therefore, compliant ortho-planar mechanisms can be identified as the most promising embodiment for the design of miniaturized piezoelectric energy harvesters. The approach taken in this thesis is to generate designs in which stiffness compensation can be integrated in a compliant ortho-planar mechanism to reduce the out-of-plane stiffness such that the micro-scale systems can be applied in vibration energy harvesters for low-frequency applications.

A key challenge in such a system is the introduction of the required preload at such small scales. Due to the high precision that is required, physical handling without causing damage is very difficult and economically unjustifiable [46, 47]. Alternative approaches have been explored, such as shaking [48] or leveraging the stresses resulting from the deposition of thin-films during the fabrication process [49, 50]. The approach explored in this thesis is to introduce the preload by incorporating dedicated preloading features in the design which can be engaged by packaging. The main advantage of this approach is that while it can be applied in a very reproducible fashion, the amount of preloading can always be tuned by changing the design of the package. Moreover, as this method does not requiring tuning of the microfabrication processes, it can be used for prototyping.

LIMITATIONS

This section will elaborate on topics not explicitly discussed in the chapters of this thesis, but nevertheless important to the topic of vibration energy harvesting. The issues of power conditioning and storage and the reliability of piezoelectric transducers are addressed successively.

It is readily acknowledged that vibration energy harvesters are rarely used as standalone devices, and that real-world applications will typically integrate them in bigger system that include power management electronics and a form of energy storage [51]. This implies that using a simple resistive load to determine the electrical power output of the transducer, a method used in most research reporting vibration energy harvesters, falls short in some aspects. First of all, it disregards the electrical losses that occur during the conditioning and storage of the generated power, which can lead to overestimation of the performance in a realistic application. Next, by using a passive and fixed-value resistive load, the opportunities of using active power processing techniques are not considered. In literature, various of such techniques have been demonstrated to be able to improve the output power of the harvester significantly [3, 52, 53]. In such cases, the resistive load may actually underestimate the performance of the energy harvester in a real-world application. While the author agrees that the development of a complete systems should be preferred over the study of standalone transducers, it is also felt that one step should be taken at a time. The complex interactions between the various components of the complete system may overshadow a clear focus on the mechanical design of the transducer for low-frequency applications. Therefore, the scope of this thesis is limited to the study of the vibration energy harvesters as standalone devices only.

Proposing energy harvesters as an alternative to batteries for devices with a lifespan of possibly years naturally puts great demands on the reliability of the developed systems. After all, nothing is gained if the device is equally likely to fail due to a broken energy harvester compared to a depleted battery. In the development of piezoelectric energy harvesters, the aim to maximize their power output usually demands the piezoelectric cantilevers to be operated close the point of yielding. This may result in micro-cracks and fatigue in the piezoelectric layer and results in poor reliability [54, 55]. Reliability was explored in [56, 57] but not addressed further in the scope of this thesis.

1.3 RESEARCH OBJECTIVE AND GOALS

The main objective of this thesis is to develop an effective strategy and the necessary technologies to enable vibration energy harvesting from low-frequency motion with miniaturized devices. The development of a strategy involves mainly exploratory research aimed at identifying and generalizing the vast amount of approaches described in literature, and evaluating their performance. Formulating a clear strategy allows us to provide perspective on the current state-of-the-art, and a focus for the future research directions of the field. The development of the enabling technologies ranges from proposing new design methods to the optimization of fabrication processes. The purpose is to bring these technologies to

society by implementing them in useful applications. An example of such an application is the heartbeat-powered leadless pacemaker.

In this thesis, a series of goals are formulated that build towards the main objective. These goals are formulated as follows and are addressed in each of the subsequent chapters.

- Generalize the results from experimental literature and compare the performances of different energy harvesting strategies.
- Develop a theory and design method for the synthesis of stiffness-compensated mechanisms.
- Implement stiffness compensation in a piezoelectric energy harvester that is fabricated using microfabrication processes.
- Design a statically balanced compliant ortho-planar mechanism on which a piezoelectric transducer can be integrated for low-frequency vibration energy harvesting.
- Develop a method to test energy harvesters for a heartbeat-powered pacemaker under real-world conditions by replicating a comparable vibration environment in the lab.
- Implement the statically balanced design in silicon manufacturing process.

1.4 THESIS OUTLINE

Chapter two presents an analysis of the performance of experimental work on vibration energy harvesting reported in literature. The reported generators are classified based on the strategy that is used and new metrics are introduced to assess their performance in terms of efficiency and bandwidth. The results from this analysis give a general insight in the effectiveness of the different strategies under various operating conditions.

Chapter three will present a new theoretical framework describing the relation between the critical loads and the post-buckled force-deflection relation of a beam. Based on this theory, a synthesis method is proposed for the design of stiffness compensation in buckled compliant mechanisms. Furthermore, the method is applied to design new compliant ortho-planar mechanisms in which the stiffness characteristics can be tuned. Finally, these mechanisms are fabricated and their force-deflection relations are validated experimentally.

Chapter four demonstrates the implementation of the compliant ortho-planar designs in functional MEMS energy harvesters. The devices are fabricated from a flexible kapton substrate on which a piezoelectric layer of AlN is patterned through microfabrication processes. In order to introduce the required preloading at the small scale, a new method called package-induced preloading is developed in which the flexible mechanisms are laminated over a package with a geometry extending out-of-plane. The

resulting devices are the first piezoelectric MEMS energy harvesters in which stiffness compensation is reported.

Chapter five reports an improved design of the compliant ortho-planar mechanisms shown in chapter three which was used to develop the first-ever statically balanced compliant ortho-planar mechanism. The design, in which two flexures are mounted at right angles to balance the out-of-plane deflection of a cantilever, is subsequently applied to a piezoelectric energy harvester. The resulting device was tested experimentally for low-frequency motion and demonstrated a six-fold increase in power output compared to a version in which the flexures were removed.

Chapter six describes the utilization of the stiffness-compensated energy harvester in a heartbeat-powered pacemaker. To this end, the vibration environment of the heartbeat motion as experienced by a pacemaker will be analyzed. Furthermore, a method will be developed to reproduce this environment in the lab such that energy harvester prototypes can be tested experimentally in conditions comparable to the real-world.

Chapter seven continues with the micro-scale implementation of a the design presented in chapter five. Through simulation it will be shown that a device with an eigenfrequency of <30 Hz can be achieved without the need for a big mass, which is a remarkable result for a MEMS device of this size.

Chapter eight provides a discussion of the material presented in the previous chapters, outlines the main contributions and considers their impact in a broader perspective. A graphical representation of the structure of this thesis is shown in Figure 1.1.

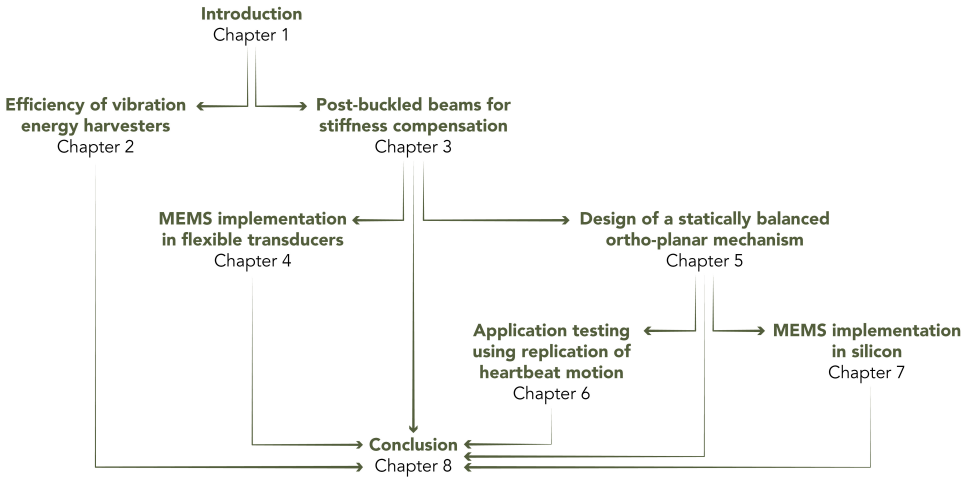

Figure 1.1: Structure of the thesis chapters.

2 EFFICIENCY OF VIBRATION ENERGY HARVESTERS

Although motion energy harvesting at the small scales has been a research topic for over 20 years, the implementation of such generators remains limited in practice. One of the most important contributing factors here is the poor performance of these devices under low-frequency excitation. In this research, a new metric is proposed to evaluate the performance and bandwidth of generators at low frequencies. For that, a classification based on the dynamics was made. It was found that the highest efficiencies were found in single degree of freedom resonators where a large motion amplification was achieved. Smaller generators can be designed by limiting the motion through end-stops at the cost of a reduced efficiency. Moreover, it was argued that upon miniaturization, resonators could be outperformed by generators using a frequency up-conversion principle.

2.1 INTRODUCTION

Motion energy harvesting with miniaturized devices has been studied for over 20 years since the early work of Williams and Yates in 1996 [59] which investigated the piezoelectric, electromagnetic, and electrostatic transduction mechanisms for the purpose of vibration-to-electric energy conversion. Devices that incorporating such a transduction mechanisms are called motion energy harvesters and have received much interest as they may provide an alternative to batteries. Especially for biomedical applications such as pacemakers, hearing aids, insulin pumps and various sensors the elimination of a dependency on batteries can offer a huge quality of life improvement to patients. Despite the vast amount of research on the topic, the implementation of miniaturized motion energy harvesters remains limited in practical applications [60]. One of the main contributing factors is that the performance of these systems is poor when excited by a low-frequency driving motion such as human motion (< 10 Hz) [61].

In prior art, a few design strategies were proposed to effectively harvest energy from these low-frequency motions. Bowers et al. (2009) [62] argued

This chapter originally appeared as T.W.A. Blad, N. Tolou, *On the efficiency of energy harvesters: A classification of dynamics in miniaturized generators under low-frequency excitation* in the Journal of Intelligent Material Systems and Structures **16**, 30 (2019) [58].

that the commonly used resonant generators need to be very large to be effective at low frequencies. As an alternative, a 4 cm^3 concept based on rolling magnets was proposed for which a maximum average output power of 1.44 mW was shown when carried in a pocket during running. Galchev et al. (2011) [63] developed a piezoelectric system based on the frequency up-conversion (FupC) principle pioneered by Kulah and Nafaji [64]. The 3.75 cm^3 prototype was able to generate an average power of 13.6 μW from a vibration of 10 Hz at 1 g . In the work of Geisler et al. (2017) [65] non-linearities are introduced to constrain the internal motion and limit the size of generator. Excited by a 6 Hz vibration at 2 g, the 9 cm^3 prototype showed an average power of 6.57 mW. It was estimated that only up to 36% of the theoretical power output was attainable as a result of the displacement constraints.

However, with existing methods it is not possible to generalize the results from these studies and compare the performances of the used design strategies on an abstract level. Without such a proper comparison it remains unclear what specific challenges need to be solved to achieve a high efficiency. The research objective of this work is to classify these generators by their dynamics and compare the efficiencies between the groups. For this purpose a new metric will be proposed. Firstly, the metric presents a modification to an existing efficiency metric that adds a sensitivity to generator shape and material. Secondly, a new parameter is introduced which is called the motion ratio and relates the excitation amplitude to the dimension of the generator in the direction of the driving motion.

In section 2.2 the methods are explained and the new metrics are introduced. Section 2.3 presents the classification and section 2.4 presents the results of the reported generators and identifies the respective groups. Section 2.5 discusses the observations that can be made from the results and the conclusions are presented in section 2.6.

2.2 METHODS

PERFORMANCE EVALUATION

For the comparison of different devices or harvesting strategies there are a number of performance metrics available. Excellent investigations and discussions of these metrics were presented by Mitcheson et al. [3] and Liu et al. [27]. The *volume figure of merit* (FoM_V) was introduced as a metric that could make a fair comparison between different types and sizes of generators under different vibration conditions. This metric compares the useful power output of a generator to the power output of an imaginary generator cube of the same volume, V, driven by the same vibration conditions. To set a baseline, the proof-mass of this generator is assumed to be made from gold.

Although the FoM_V normalizes the output power to the total volume, the shape of this volume is not taken into account. This is a problem because the

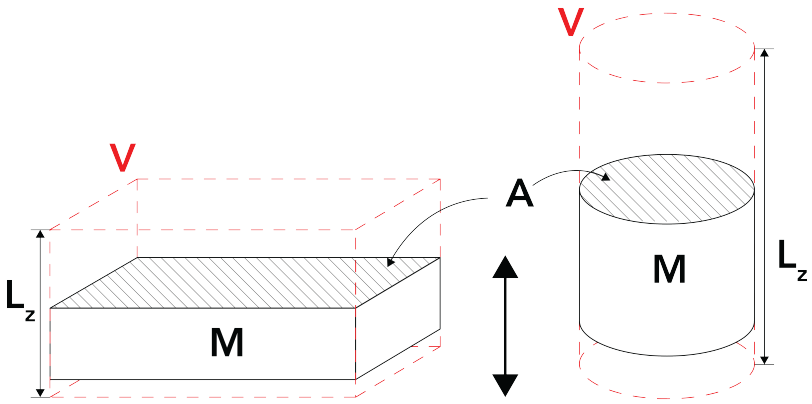

Figure 2.1: Two imaginary generators with an equal total volume, V, and mass, M. A greater power output can be expected from the cylindrical generator due to its larger dimension in the direction of the driving motion, L_z.

power output of the generator scales with $P \propto L^2$ in the direction of the driving motion and $P \propto L$ in the perpendicular dimensions [3]. Consider the example of Figure 2.1, where two imaginary generators are sketched with an equal volume, V, and mass, M. In this example a larger power output can be expected from the cylindrical generator due to its greater L_z dimension. This leads to an unfair comparison where some designs are already ahead in terms of FoM_V due to their shape, regardless of their dynamic performance.

In order to make this comparison more fair, a variation on the FoM_V is proposed, which will be named the generator figure of merit (FoM_G). In this metric, the $V^{\frac{4}{3}}$ is replaced by the product VL_z, to take into account both the volume, and the shape of the generator. Furthermore, the real density of the proof mass material is included instead of the density of gold. This ensures that the efficiency fully depends on the design of the generator, and not on the selection and/or availability of the proof mass material. The following expression is obtained.

$$\text{FoM}_\text{G} = \frac{P_\text{avg}}{\frac{1}{16} Y_0 \rho_\text{M} V L_z \omega^3} * 100\% \tag{2.1}$$

Where Y_0 and ω are the amplitude and frequency of the driving motion, V is the total volume occupied by the device, L_z is the dimension of the generator along the direction of the applied motion, ρ_M is the density of the proof mass material and P_avg is the average output power.

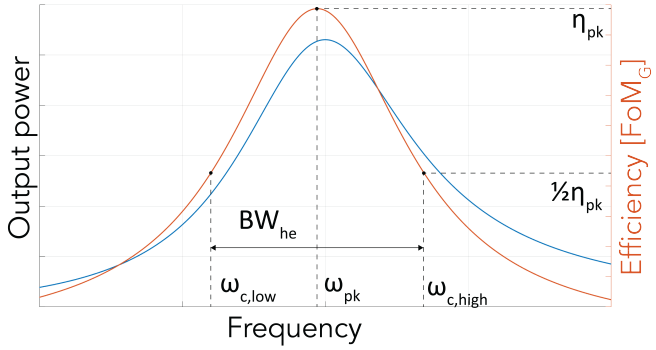

Figure 2.2: Example frequency-output power (blue) and frequency-efficiency graph (orange) of an energy harvester. The peak efficiency, η_{pk}, and normalized half-efficiency bandwidth, BW_{nhe}, indicated in the figure are important properties for the performance evaluation of the generator.

PEAK EFFICIENCY AND NORMALIZED HALF-EFFICIENCY BANDWIDTH

In a great deal of the experimental work, the power output of a generator prototype is presented for a range of input conditions, typically through frequency sweep (with constant acceleration). From this data a frequency-efficiency graph can be constructed by calculating Equation (2.1) for every data point, as shown in Figure 2.2. For the assessment of the performance of the generators, two properties will be evaluated: the peak efficiency, η_{pk}, and the normalized half-efficiency bandwidth, BW_{nhe}. In contrast to previous metrics, the peak performance and bandwidth are therefore derived from the efficiency as calculated by the FoM_G instead of from the raw output power.

The peak efficiency (η_{pk}) is defined as the maximum efficiency obtained by the generator. Please note that this point does not necessarily coincide with the point at which a maximum output power is achieved. Although a fair comparison can be made between the efficiencies of different designs, η_{pk} only reflects the maximum efficiency at one particular frequency. Therefore, no bandwidth information is included in this property. For this reason a second property is derived from the frequency-efficiency graph. The normalized half-efficiency bandwidth (BW_{nhe}) is defined by the following expression.

$$BW_{\text{nhe}} = \frac{BW_{\text{he}}}{\omega_{\text{pk}}} = \frac{\omega_{\text{c,high}} - \omega_{\text{c,low}}}{\omega_{\text{pk}}} \tag{2.2}$$

Where BW_{he} is the half efficiency bandwidth between the higher ($\omega_{\text{c,high}}$) and lower ($\omega_{\text{c,low}}$) corner frequencies and ω_{pk} is the frequency at which η_{pk} is found.

THE MOTION RATIO

The dynamics of the energy harvester are for a great deal determined by the L_z dimension of the generator, and the amplitude of the driving motion, Y_0. For example, many generators make use of resonance induce an relative displacement that is greatly amplified w.r.t. the amplitude of the driving motion [26]. Naturally, these dynamics are only possible if $L_z >> Y_0$ for obvious reasons. Therefore, it is proposed here to look at the ratio between the vibration amplitude and this dimension. This ratio is defined here as the motion ratio, λ, of the generator.

$$\lambda = \frac{L_z}{2Y_0} \tag{2.3}$$

LITERATURE SEARCH METHOD

Relevant scientific literature on the topic of energy harvesting was searched in the database of Scopus. Only publications of experimental nature where both λ and the FoM_G could be found are included in the dataset. This means that the relevant parameters were directly reported, could be calculated, or could be estimated from graphs or figures. For example, the generator volume was stated directly, or calculated based on the reported dimensions of the device. Sometimes, a particular design was tested under multiple conditions and therefore appears multiple times in the table, with different λ and FoM_G. It should be noted that the dataset is predominantly oriented towards generators operating at a frequency below 100 Hz because it was expected that low motion ratios would rarely be found at higher frequencies due to small vibration amplitudes ($Y_0 \propto \frac{1}{\omega^2}$). Moreover, it should be noted that a great portion of the literature fails to report a complete set of the important parameters of the generator and the testing conditions required to calculate the FoM_G. The dataset reported here is therefore only a fraction of the total amount of experimental work.

2.3 CLASSIFICATION OF GENERATOR DYNAMICS

Based on the dynamics found in the reported energy harvesters a classification is proposed where the generators are split in the following groups. The designs found in literature are sketched and grouped in Figures 2.3 and 2.4 according to the classification. In these figures, the dotted lines indicate the windings of a coil and represent an electromagnetic transducer in combination with the magnets sketched as white-gray rectangles; the gray patches with dashes represent a piezoelectric transducer and the gray lines are flexible elements; the light-gray rectangles are rigid bodies and the dark-gray rectangles are the inertial masses. Finally, the double-sided arrow represents the vibration direction and is imposed in all the points marked as grounded.

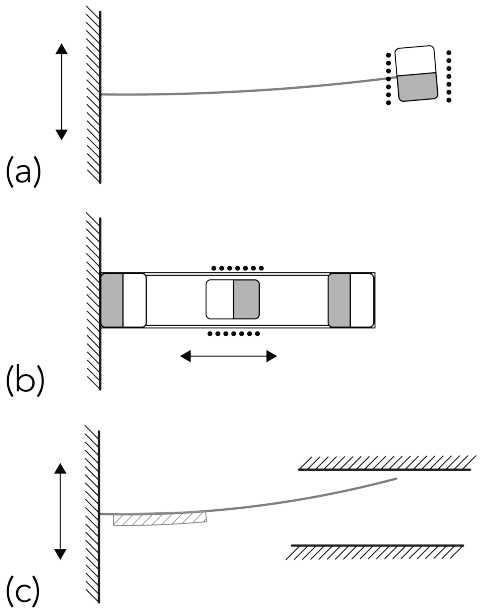

Figure 2.3: Sketches of single degree-of-freedom energy harvesters; (a) without end-stops; (b) with magnets acting as soft-stops; (c) with mechanical contacts acting as hard-stops.

SINGLE DEGREE OF FREEDOM GENERATORS

This subsection groups all energy harvesters that have a single degree of freedom which is used directly for energy conversion.

The first group that can be found among the reported devices are the single degree-of-freedom (SDoF) that operate without end-stops. In Figure 2.3(a) the working principle of the generator reported by Beeby et al. [28] is sketched. In this design a magnet at the tip of a thin beam moves relative to a fixed coil, inducing a current. These generators can be modeled as a linear mass-spring-damper system with mass M, stiffness K and damping coefficient C. The following equation of motion can be found.

$$M\ddot{z} + C\dot{z} + Kz = M\omega^2 Y_0 \sin(\omega t) \tag{2.4}$$

Where z is the relative internal displacement and ω and Y_0 are the frequency and amplitude of the driving motion, respectively. These generators are typically designed operate at resonance where they greatly amplify the driving motion and achieve high efficiencies.

Next are the non-linear energy harvesters that rely on a gradually increasing stiffness to limit the internal motion. An example of such a system is the design reported by Geisler et al. [65] which is sketched in Figure 2.3(b). In this design a moving magnet experiences a repulsive force from the

oppositely poled magnets at the ends. The dynamics of such a system can be modeled by the Duffing equation shown in Equation (2.5) [66].

$$M\ddot{z} + C\dot{z} + \alpha z + \beta z^3 = M\omega^2 Y_0 \sin(\omega t) \tag{2.5}$$

Where α controls the linear stiffness and the stiffening effect is controlled by $\beta \geq 0$. Moreover, systems where $\alpha > 1$ have one stable position, and a bi-stable system is obtained for $\alpha < 1$.

In the third group there are the energy harvesters with a very rapid stiffening effect at the end of their range of motion. These stiffening effects are for example the result of a mechanical contact, as is the case in the design of [67] which is sketched in Figure 2.3(c). In this design the proof mass mounted on the tip of a piezoelectric beam makes contact with mechanical elements on the top and bottom during excitation. The dynamics of these systems can be modeled by the piece wise linear equation of motion given in Equation (2.6). Where C_h and K_h are the damping coefficient and stiffness of the housing, respectively. Solutions to this equation of motion can be found through numerical methods.

$$\begin{aligned}
&\textbf{for } z \geq Z_l: \\
&M\ddot{z} + (C + C_h)\dot{z} + (K + K_h)z - K_h Z_l = M\omega^2 Y_0 \sin(\omega t) \\
&\textbf{for } -Z_l < z < Z_l: \\
&M\ddot{z} + C\dot{z} + Kz = M\omega^2 Y_0 \sin(\omega t) \\
&\textbf{for } z \leq -Z_l: \\
&M\ddot{z} + (C + C_h)\dot{z} + (K + K_h)z + K_h Z_l = M\omega^2 Y_0 \sin(\omega t)
\end{aligned} \tag{2.6}$$

FREQUENCY UP-CONVERTERS

Additionally, there are systems that use an inertial mass to excite a secondary oscillator in its natural frequency which is increased w.r.t the frequency of the driving motion. The relative motion of the secondary oscillator is than used for energy conversion.

The first group of frequency up-converters (FupC) use the impact of an impact member to excite the secondary oscillators. An example of such a system is the generator reported by Dechant et al. [68] and is shown in Figure 2.4(a). In this design, a piezoelectric membrane is mounted between a proof mass (dark) and an impact member (light). Under a driving motion the impact member is displaced until it makes contact with the mechanical stops at the end of its range of motion. As a result, the proof mass experiences an impulse-like response and begins to oscillate in its own natural frequency. This system can be modeled as a two-DoF system with the following equations of motion.

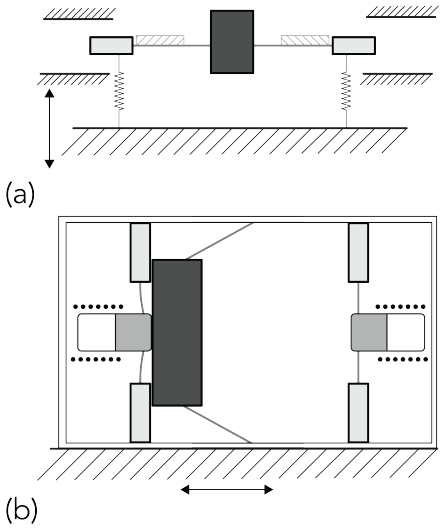

Figure 2.4: Sketches of frequency up-converting energy harvesters; (a) using impact; (b) using plucking.

$$\text{Equation } 2.6 + C_2 d\dot{z} + K_2 dz = M\omega^2 Y_0 \sin(\omega t) \tag{2.7}$$
$$M_2 \ddot{z}_2 + C_2 d\dot{z} + K_2 dz = M_2 \omega^2 Y_0 \sin(\omega t)$$

Where Equation 2.6 is the relevant left side of Equation (2.6), z_2 is the relative internal displacement of the proof mass w.r.t. the housing, $dz = z - z_2$ is the relative internal displacement between the impact member and the proof mass and C_2, K_2 and M_2 are the damping coefficient and stiffness of the connection between the two bodies, and the mass of the proof mass, respectively.

The final group contains the FupC that excite their secondary oscillator through plucking. An example was reported by Galchev et al. [69] and is sketched in Figure 2.4(b). The design consists of an inertial mass which snaps back and forth between the two secondary oscillators, attaching magnetically. When the inertial mass detaches, the secondary oscillator starts oscillating at its natural frequency and generate power through electromagnetic induction. The dynamics in such a system can be modeled as three oscillators with the following equations of motion.

$$\text{Equation } (2.6) + F_u(du) + F_v(dv) = M\omega^2 Y_0 \sin(\omega t) \tag{2.8}$$
$$M_u \ddot{u} + C_u d\dot{u} + K_u u + F_1(du) = M_u \omega^2 Y_0 \sin(\omega t)$$
$$M_v \ddot{v} + C_v d\dot{v} + K_v v + F_2(dv) = M_v \omega^2 Y_0 \sin(\omega t)$$

Where u and v and du and dv are the positions of the secondary oscillators w.r.t. the housing and w.r.t. the inertial mass, respectively. M_u, C_u, K_u and M_v, C_v, K_v are the mass, damping coefficient and stiffness of the secondary oscillators and F_u and F_v are the interaction forces between the secondary oscillator and the inertial mass.

2.4 RESULTS

Table 2.1 presents the classification of the reported generators and the calculated values for λ, η_{pk} and BW_{nhe}. The color coding of the groups is used in Figures 2.5 and 2.6, where the motion ratios of the generators are plotted against their peak efficiency η_{pk} and normalized half-efficiency bandwidth BW_{nhe}, respectively. To visualize the domains in which the generators of the different groups were reported, shaded areas were added to the figures. Based on the reported data, the following observations can be made.

SINGLE DEGREE OF FREEDOM GENERATORS

The majority of the reported generators are of the SDoF class which covers a wide spread in motion ratios, efficiencies and bandwidths. While efficiencies range from 0.001% to 27.5%, most work reports values between 0.1% and 1%. The normalized half-efficiency bandwidths ranged from 0.01 to 1.78.

In the group without end-stops 3 generators were found. The motion ratio's found for this group are at the right of the spectrum presented in Figure 2.5. It can be observed that within this group the efficiency and motion ratio are correlated. The efficiency of 28% reported by [28] is the highest efficiency (according to FoM_G metric) reported in energy harvesting literature. This work was also the only instance where bandwidth information was reported for this group. The half-efficiency bandwidth was 0.53 Hz around a ω_{pk} = 52 Hz yielding a normalized half-efficiency bandwidth of BW_{nhe} = 0.01.

Table 2.1: The performance properties of the generators categorized in two classes and five groups based on their dynamics.

Class	Group	Motion ratio (λ)	Efficiency (η_{pk})	Bandwidth (BW_{nhe})	References
SDoF	Without end-stops	27-453	0.08-27.5%	0.01	[28, 70, 71]
	With soft-stops	7.62-409	0.26-7.72%	0.2-0.58	[65, 72–77]
	With hard-stops	0.56-65.9	0.001-1.17%	0.1-1.78	[67, 78–82]
FupC	Using impact	0.35-14.54	0.011-0.83%	0.071-0.72	[68, 83–85]
	Using plucking	0.025-14.13	0.002-1.66%	0.336-3.08	[63, 69, 86–88]

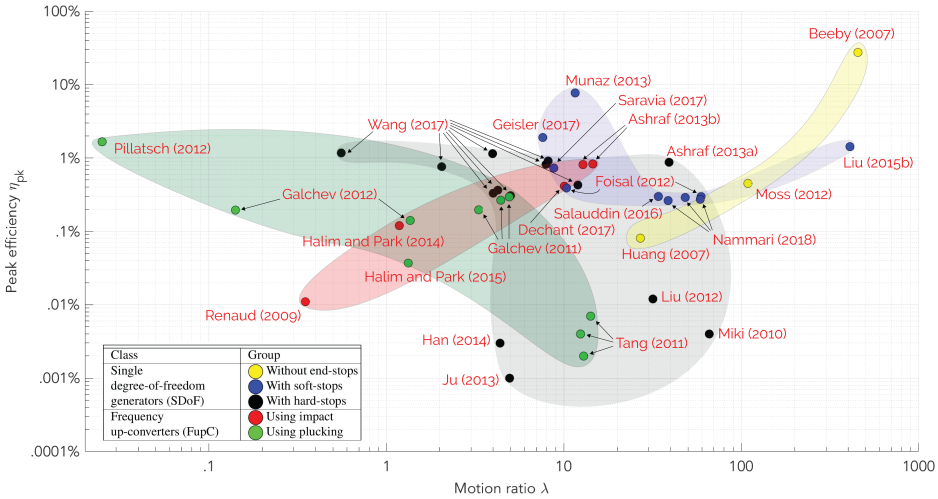

Figure 2.5: Motion ratio (λ) versus peak efficiency (η_{pk}) of reported generators by generator type. The shaded areas indicate the ranges in which the generators of different groups were reported; the arrows indicate a source which tested prototypes under multiple vibration conditions.

The devices with soft-stops were reported 7 times with motion ratios ranging between 7.62 and 409. The efficiencies of these devices ranged from 0.26% to 7.72% and the normalized half-efficiency bandwidths ranged from 0.2 to 0.58. In the work of Salauddin et al. [74] the effect of the motion ratio on the efficiency was specifically tested by varying the amplitude of the diving motion for a fixed frequency. It was found that when the motion ratio was decreased from 56.81 to 34.09, the efficiency increased from 0.2% to 0.3%.

In the group with hard-stops 6 generators were reported. With motion ratios between 0.56 and 65.9 and efficiencies from 0.001 to 1.17% this group covers a large part of Fig 2.5. Moreover, in this group normalized half-efficiency bandwidths were reported between 0.1 and 1.78. Wang et al. [78] reports testing their prototypes under 6 conditions varying the motion ratios at fixed frequencies and found that for small motion ratio's ($\lambda < 1$) a small increase in efficiency was found for their prototypes increased as the motion ratio was increased.

FREQUENCY UP-CONVERTERS

The FupC class generators are reported predominantly on the left side of Figure 2.5, with motion ratio's of 15 or less. Their motion ratios range from 0.025 to 14.54 and efficiencies are reported between 0.002 and 1.66%. The normalized half-efficiency bandwidths ranged from 0.071 to 3.08.

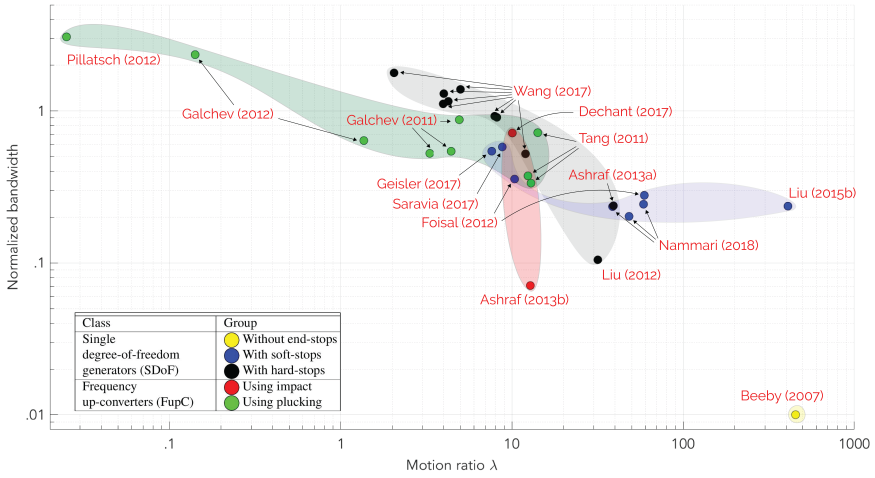

Figure 2.6: Motion ratio (λ) versus normalized half-efficiency bandwidth (BW_{nhe}) of reported generators by generator type. The shaded areas indicate the ranges in which the generators of different groups were reported; the arrows indicate a source which tested prototypes under multiple vibration conditions.

In the group that uses impact, 4 generators were found. The motion ratios of these devices ranged from 0.35 to 14.54 and their efficiencies between 0.011 and 0.83%. The normalized half-efficiency bandwidths ranged between 0.071 and 0.72. Moreover, the prototype reported by Ahsraf et al. [85] was also tested for a fixed frequency. When the motion ratio was decreased from 248 to 13, the efficiency increased from 0.088% to 0.83%.

Lastly, 5 examples of frequency up-converters using plucking were found. Their motion ratios ranged from 0.025 to 14.13 and efficiencies between 0.002 and 1.66% were reported. The normalized half-efficiency bandwidths were reported between 0.336 and 3.08. The prototype of Pillatsch et al. [87] reported the lowest motion ratio and largest normalized bandwidth found in literature at $\lambda = 0.025$ and $BW_{\text{nhe}} = 3.06$, respectively.

2.5 Discussion

The wide spread in efficiency of the reported energy harvesters can be attributed to the number of variables that contributing to the final efficiency. First of all there are great differences in the degree of optimization and overall quality of the transduction elements, the mechanical structures and the power conditioning circuitry. Next there are great differences in the types of dynamics that are employed and the operating conditions under which they are evaluated.

For example, in linear systems the maximum power output coincides with the maximum efficiency at the resonance point and it is common practice to evaluate the performance at this point. However, for non-linear systems this is not necessarily true and the performance is commonly evaluated at the point of maximum output power, which is not necessarily the point of maximum efficiency. Finally, at least some of the spread can be attributed to the uncertainty that comes with the estimation of some of the parameters that were not explicitly reported by the authors of the experimental work. When the references are grouped by publication year it can be found that the efficiencies of the reported generators converge over time. This can be an indication of the maturing of the field. Moreover, it is likely that the adoption of established strategies and designs is the main contributor in this aspect.

SINGLE DEGREE OF FREEDOM GENERATORS

When generators in this group without end-stops are driven at resonant condition, amplification of the driving motion is achieved with a ratio that (for $t \to \infty$) only depends on the total damping in the system. Moreover, the portion of output power to the total energy dissipated in the system is only dependent on the ratio between the electrical damping and the parasitic damping. The electrical damping has to be provided by the transduction mechanism and is limited in practice by for example magnetic flux density, maximum tensile stress or dielectric breakdown in electromagnetic, piezoelectric and electrostatic transducers. As a result, in order to maximize the fraction of useful output power (and thus the efficiency) the amplification factor should be maximized. However, maximizing the amplification factor leads to a very narrow bandwidth, which can also be observed from Figure 2.6 where the device from this group performs has by far the smallest normalized bandwidth.

In practice, the upper limit for the amplification factor also depends on the dimensions of the generator and is therefore directly related to the motion ratio of the device. As a result, it can be expected that SDoF generators without end-stops demonstrate higher efficiencies at larger motion ratios. This is supported by the data shown in Figure 2.5 where a clear correlation is found between efficiency and motion ratio in the SDoF generators without end-stops. Furthermore, none of these systems were found for lower motion ratios which indicates that these are not favorable conditions for a SDoF system without end-stops.

Within the group of SDoF generators with soft-stops two embodiments are found. In Figure 2.5 two groups of points can be observed around $\lambda = 10$ and between $30 < \lambda < 60$. In these devices the stiffening effect is a result of a magnetic suspension. The footprint of such a suspension is relatively small and therefore these embodiments were found to be relatively efficient in terms of volume. The other embodiment uses a mechanical element to facilitate the stiffening effect. Since the footprint of the mechanical element is relatively large, it was found that the efficiency of this design was lower in

terms of volume.

In terms of dynamics, the same principles as with the SDoF generator without end-stops hold. Therefore, it should be expected that higher efficiencies are demonstrated at larger motion ratios. However, the normalized bandwidths of generators using soft-stops are much larger compared to generators without end-stops. In general, the use of soft-stops allows for an increased bandwidth and a lower motion ratio and therefore a greater degree of miniaturization at the cost of a reduced efficiency.

SDoF generators with hard-stops are found in different embodiments and are found in a broad range of motion ratios and efficiencies. Compared to the soft-stop, the ratio between the travel stiffness and the hard-stop stiffness can be extremely large which allows for very small motion ratios and therefore a large degree of miniaturization. In general, the kinetic energy of the mass upon engaging the hard-stop is lost which may greatly hurt the efficiency of these systems. In terms of bandwidth it can be seen from Figure 2.6 that large normalized bandwidths can be obtained for these devices. Furthermore, it was observed that increased bandwidths are found for lower motion ratios.

Within the class of SDoF generators it can be observed that the different groups are reported at different ranges of motion ratios, efficiencies and bandwidths. SDoF generators without end-stops are only reported at larger motion ratios, report the greatest efficiency and the narrowest bandwidth. At very small motion ratios, exclusively SDoF generators with hard-stops were reported. Although their reported bandwidths are much greater, their efficiencies are generally lower due to the loss of kinetic energy when the hard-stops engage. Between those groups the soft-stopped generators are reported. In this group generators are reported with slightly lower motion ratios compared to those without end-stops, but greater efficiencies compared to those with hard-stops. In general, a correlation can be found between the motion ratio and the efficiency of SDoF generators.

FREQUENCY UP-CONVERTERS

In the group of FupC generators two embodiments can be found. First there are the systems where an inertial mass impacts on the secondary oscillator. In Figure 2.5 the two lowest efficiencies of this group are linked to these embodiments. Next, there are the systems where the secondary oscillator is mounted on top of an impact member, which impacts on an end-stop. It was found that these systems reported larger efficiencies compared to the other group.

In the group of plucking FupC generators three embodiments were found. The two generators with the smallest motion ratios made use of a secondary oscillator that was latched magnetically to an inertial body and detached upon excitation. These designs demonstrated the greatest normalized bandwidths of all reported energy harvesters. One design based on mechanical contact was reported and is found in Figure 2.5 in the middle

of the group. The two designs with the largest motion ratios used piezoelectric beams with a magnet at the tip that was repelled by a magnet on the passing inertial mass.

Between the groups of FupC no convincing evidence was found that one group would have an advantage compared to the other in term of motion ratio, efficiency or bandwidth.

COMPARISON BETWEEN SDOF AND FUPC GENERATORS

The most striking difference between the groups of SDoF and FupC generators is the motion ratio at which they are reported; SDoF systems are mostly reported on the right side of Figure 2.5, while FupC systems dominate the left side. At the larger motion ratios the SDoF systems report higher efficiencies compared to the FupC. Reasons for this could be the significantly larger amount of reported work on SDoF generators and the increased complexity of the dynamics of FupC. However, at the lower motion ratios it could be argued that FupC systems may be more efficient than SDoF systems. For example, in the results of the two works of Ashraf et al. a SDoF generator and FupC are reported with a similar design, shape and volume and tested under similar conditions [79, 85]. At a motion ratio of approximately $\lambda = 12$, the efficiencies of the SDoF generator and the FupC were 0.30% and 0.80%, respectively.

Another important property of the energy harvester is the bandwidth. Although SDoF generators have the highest peak efficiency, they are very sensitive to changes in the frequency of the driving motion. As a result, their practical use is greatly limited by the narrow range of frequencies where this efficiency is achieved. The non-linearities as a result of the end-stops, or the use of a FupC strategy can greatly improve the efficiency over a much wider bandwidth. This can also be clearly observed from the differences between the groups in Figure 2.6.

RECOMMENDATIONS

The first recommendation is to consider the motion ratio at an early stage in the design process of the generator, similar to the frequency ratio ($\frac{\omega}{\omega_n}$), because it greatly influences what dynamics can be used in the device. Next, it is recommended for authors of experimental work on energy harvesters to report at least the following device properties: The dimensions, the total (packaged) volume, the moving mass and the travel range of the mass. Additionally, the following variables should be reported under all test conditions: The frequency and acceleration (or amplitude) of the driving motion and the power output. These parameters are necessary to perform proper analysis of the performance of the reported generator. It may be desirable to evaluate the wideband performance of an energy harvesting system in a single metric. An example of such a metric could be the product of η_{pk} and BW_{nhe}. However, reflecting all of these properties in a single figure may lead to the loss of important information and is therefore not

recommended as a stand-alone figure of merit. The last recommendation is to systematically benchmark the performance of typical generator designs under varying conditions and at different scales to gain insight in the design parameters and their sensitivities. This can be used to develop more accurate models to estimate the performance of vibration energy harvesters and will be the focus of future work.

2.6 CONCLUSION

Although motion energy harvesting at the small scales has been a research topic for over 20 years, the implementation of such generators remains limited in practice. One of the most important contributing factors here is the poor performance of these devices under low-frequency excitation. In this research, the efficiencies and bandwidths of small scale generators are studied through two new metrics. The generator figure of merit, FoM_G, is a variation of an existing efficiency metric which can facilitate a better comparison between generators by making it independent of shape and material. From this metric the peak efficiency (η_{pk}) and the normalized half-efficiency bandwidth (BW_{nhe}) can be derived, and used as important properties to characterize the maximum efficiency and bandwidth of the generator. The motion ratio, λ, is a new metric which describes the relation between the excitation amplitude and the dimension of the generator in the direction of the driving motion. Furthermore, a classification of the dynamics is proposed where the systems are identified as either SDoF generators or FupC and categorized further in one of the five groups. It was found that SDoF generators reported the highest efficiencies, but were mainly found at large motion ratio's and had a very narrow bandwidth. Through the use of end-stops lower motion ratios and larger bandwidths could be achieved at the cost of a reduced efficiency. The efficiency of FupC generators was on average found to be lower compared to SDoF systems. However, their typical motion ratios were also much lower and it was found that at these lower motion ratios FupC systems can outperform SDoF generators in terms of both efficiency and bandwidth.

3 POST-BUCKLED BEAMS FOR STIFFNESS COMPENSATION

This chapter describes a method for tuning the stiffness of building blocks for statically balanced compliant ortho-planar mechanisms. Three post-buckled mechanisms are proposed where the flexural rigidity can be manipulated over a part of their length in order to tune the ratio between the first two critical loads. A sensitivity analysis using finite element simulation showed that the best balancing performance is obtained in these mechanisms when this ratio was maximized. The results were validated experimentally by capturing the force-deflection relations.

3.1 INTRODUCTION

Compliant ortho-planar mechanisms (COMs) are planar mechanisms that allow out-of-plane motion through the deflection of flexible members [45]. The advantages of COMs over their conventional counterparts are the ease of their manufacturing process, their compactness and resistance to wear [29]. At the scale of micro-electromechanical systems (MEMS) these mechanisms can be applied in accelerometers [90], actuators [91] and micro energy harvesters [81, 92]. However, a disadvantage of miniaturized compliant mechanisms is that a significant part of the input energy is stored as strain energy in the deflecting flexible components [34]. This can lead to a low range of motion, poor mechanical efficiency and high natural frequencies [93]. Especially for micro energy harvesting applications, these drawbacks can greatly reduce the overall efficiency [58].

In order to overcome this problem, the stiffness of the mechanism can be reduced by static balancing. Static balancing uses a negative stiffness element as a balancer that counteracts the positive stiffness of the mechanism. As a result, zero stiffness can be obtained over a certain working range if the positive stiffness is of the same magnitude as the negative stiffness [37]. Negative stiffness can be obtained in compliant mechanisms by preloading a flexible element in postbuckling [36]. A MEMS gravimeter is demonstrated by Middlemiss et al. [94] that features a proof mass on top of an anti-spring mechanism. With increasing displacement, the anti-spring

This chapter originally appeared as T.W.A. Blad, R.A.J. van Ostayen, N. Tolou, *A method for tuning the stiffness of building blocks for statically balanced compliant ortho-planar mechanisms* in Mechanism and Machine Theory 126 (2021) [89]

softened and the system was able to reach a resonant frequency of 2.3 Hz in the vertical orientation. Another statically balanced compliant mechanism (SBCM) was developed and studied by Tolou et al. [95]. This mechanism was fabricated using deep reactive-ion etching and achieved a near zero stiffness characteristic over a small range of motion. Kuppens et al. [49] demonstrated a SBCM in which the preloading was induced by a MEMS compatible thin film process. The resulting mechanism combined the positive stiffness of a linear guidance mechanism with a postbuckled flexure to achieve static balancing.

However, all these SBCMs had a degree of freedom (DOF) in the plane from which they were manufactured, resulting in missing out on the advantages of COMs. In this work, a method is presented to tune the stiffness of mechanisms that can be used as buckling blocks in the design of statically balanced compliant ortho-planar mechanisms (SBCOMs).

In Section 3.2 the method is introduced for tuning the stiffness of mechanisms consisting of post-buckled beams. Furthermore, the mechanical design of the prototypes and the experimental methods are discussed. The results are shown in Section 3.3 and discussed in Section 3.4. Section 3.5 lists the most important conclusions.

3.2 METHODS

BUCKLING OF A SLENDER BEAM

Figure 3.1 schematically depicts a slender beam with a uniform cross section with a length, L, and flexural rigidity of EI. The initially flat beam can be buckled by compressing the beam over a distance of dL, a process which is called preloading and results in the beam assuming a post-buckled shape that extends out of plane. The out-of-plane displacement as a function of the axial coordinate, $y(x)$, corresponding to an applied axial load, P, is governed by the following differential equation [96].

$$\frac{\mathrm{d}^4 y}{\mathrm{d}x^4} + \frac{P}{EI}\frac{\mathrm{d}^2 y}{\mathrm{d}x^2} = 0 \tag{3.1}$$

Where EI is the flexural rigidity of the section which is a combination of the elastic modulus, E, and the second moment of inertia around the bending axis, I. This is a homogeneous fourth-order differential equation for which the general solution is given as follows.

$$y(x) = A\sin(\frac{\Lambda}{\sqrt{EI}}x) + B\cos(\frac{\Lambda}{\sqrt{EI}}x) + Cx + D \tag{3.2}$$

Where A,B,C,D are unknown constants that depend on the boundary conditions of the beam and Λ are the eigenvalues corresponding to the critical loads of the beam such that $\Lambda^2 = P_{crit}$. These critical loads are the compressive loads at which the system will lose stability and buckle. Any

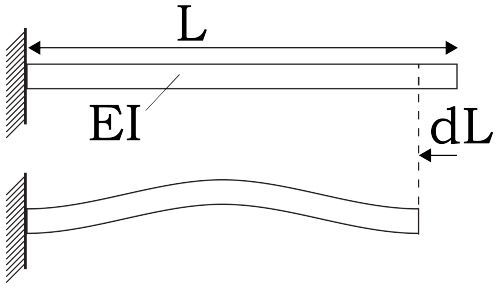

Figure 3.1: Slender beam with a uniform cross-section that can be preloaded in the axial direction to achieve the buckled shape extending out of plane.

continuous system has an infinite number of critical loads, $P_{crit,i}$, where i denotes the number of the critical load and corresponding buckling mode. The critical loads are ordered by increasing magnitude such that the first critical load, $P_{crit,1}$, is the load corresponding to lowest value. The transcendental eigenvalue problem can be expressed by the following equation [97].

$$\mathbf{T}(\Lambda)\mathbf{z} = 0 \tag{3.3}$$

Where **T** is a matrix consisting of transcendental functions in Λ, and z is a constant eigenvector containing A,B,C,D. The critical loads of the beam are represented by the non-trivial solutions of Λ for $\mathbf{z} \neq \mathbf{0}$, and the mode shapes can be found by substituting the result in Equation (3.2). Solving this eigenvalue problem for a beam with fixed boundary conditions at both ends yields the following first and second critical loads.

$$P_{crit,1} = \frac{(2\pi)^2 EI}{L^2} \tag{3.4}$$

$$P_{crit,2} = \frac{(2.85\pi)^2 EI}{L^2} \tag{3.5}$$

When the preload is applied, the axial force, P, on the beam rapidly increases until the first critical load is reached and the beam begins to buckle. Due to the slenderness of the beam the critical load is reached almost instantly [98]. Beyond the point of buckling, the axial force remains equal to the first critical load and the displacement field of the beam is described by the first buckling mode, which is the lowest energy configuration. In this configuration the beam is in a stable equilibrium where the potential energy, $E_{eq,stable}$, is equal to the work done by the preloading, W, which can be found by the following equation.

$$W = \int_0^{dL} P\mathrm{d}x \approx P_{crit,1} dL \tag{3.6}$$

When the beam is actuated in the out-of-plane direction, an unstable equilibrium can be found where the displacement field of the beam is described by the second buckling mode. Similar to the stable equilibrium, the axial force (i.e. the reaction force on the fixed boundary condition) is equal to the second critical load in this configuration [99]. Moreover, the potential energy in this configuration is equal to the work that would be required to preload the beam in the second buckling mode, $E_{eq,unstable} \approx P_{crit,2} dL$.

Therefore, the ratio between the critical loads corresponding to the buckling modes that describe the displacement fields in the stable and unstable equilibria is an important measure to identify the variation of potential energy in the buckled system. This variable is proposed as the critical load ratio, CLR, and can for these beams be found as the ratio between the first and second critical load.

$$CLR = \frac{P_{crit,1}}{P_{crit,2}} \tag{3.7}$$

For the uniform beam it can be found that the CLR = 0.49 and is independent of the geometry of the beam. However, by locally manipulating the flexural rigidity of the beam, the CLR can be tuned. As the CLR approaches unity, the potential energy in the stable and unstable equilibria converge to the same value and therefore static balancing is achieved.

MECHANISMS FOR TUNING THE CRITICAL LOAD RATIO

In order to tune the CLR, the three mechanisms shown in Figure 3.2(a) are proposed. The mechanisms have the same length, L, but their cross-sections are modified such that over a fraction of their length, αL, where $0 < \alpha < 1$, the flexural rigidity is reduced to βEI, where $0 < \beta < 1$. The portions over which the flexural rigidity of the mechanisms is reduced will be called the flexures. In Mechanism A, a single flexure is positioned at the end of the beam; in Mechanism B, a single flexure is positioned in the middle of the beam; and in Mechanism C, two flexures are positioned at the ends of the beam, with each a length $\alpha L/2$.

Mechanisms A, B, and C can be considered as stepped beams with segments of varying lengths and cross-sections in series. The length can be divided in N segments with $x_(n-1) < x < x_n$ for $n = 1 : N$ such that $x_0 = 0$ and $x_N = L$. Moreover, the flexural rigidity of section n is defined as EI_n. The solution to Equation (3.1) now becomes a set of N equations with the form of Equation (3.2) and include the unknown constants A_n,B_n,C_n, and D_n. The fixed boundary conditions at the ends remain, and at the intermediate boundaries between the segments the boundary conditions are found by enforcing continuity and balancing the forces and bending moments. These boundary conditions are formulated as follows.

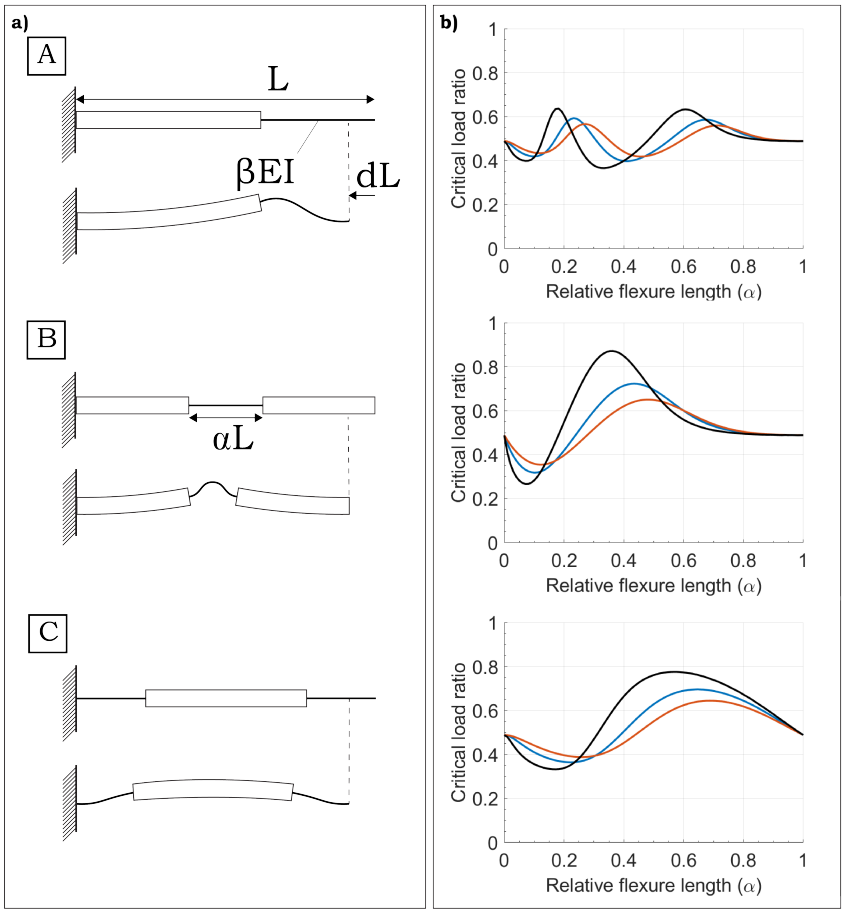

Figure 3.2: a) Proposed mechanisms (A, B, C) in unloaded and post-buckled configurations and b) their critical load ratios as a function of the design parameters α and β;

$$y_n(x_n) = y_{n+1}(x_n) \tag{3.8}$$

$$\frac{\mathrm{d}y_n}{\mathrm{d}x}(x_n) = \frac{\mathrm{d}y_{n+1}}{\mathrm{d}x}(x_n) \tag{3.9}$$

$$\frac{\mathrm{d}^2y_n}{\mathrm{d}x^2}(x_n) = \frac{\mathrm{d}^2y_{n+1}}{\mathrm{d}x^2}(x_n) \tag{3.10}$$

$$\frac{\mathrm{d}^3y_n}{\mathrm{d}x^3}(x_n) = \frac{\mathrm{d}^3y_{n+1}}{\mathrm{d}x^3}(x_n) \tag{3.11}$$

The critical loads can again be found as the non-trivial solutions of Λ for $z \neq 0$ of the transcendental eigenvalue problem of Equation (3.3). In this case, the CLR is a function of only the relative lengths and flexural rigidities of the beam segments, which are defined by the parameters α and β. In Figure 3.2(b), the CLR is plotted for Mechanisms A, B and C as a function of α for three variations of β.

MECHANICAL DESIGN

The mechanisms from Figure 3.2(a) are prototyped from 0.1 mm thick spring steel ($E = 190GPa$) using a Spectra-Physics Talon 355-15 diode pumped solid-state (DPSS) UV laser system with a wavelength of 355 nm and maximum power of 15 W at 50 kHz and are shown in Figure 3.4(a). The relative difference in flexural rigidity was fixed at $\beta = 0.1$, which was realized by manipulating the width of the beam. For all mechanisms the following parameters were fixed: the unloaded length, L, the applied axial displacement, dL, the width of the wide segments, w, the width of the narrow segments (i.e. flexures), w_f, and the thickness, t. The mechanisms were fabricated with flexure lengths, L_f, such that the relative lengths of the flexures, α, correspond to the maxima in CLR found in Figure 3.2(b). For Mechanism A, two maxima were found in the CLR and therefore two prototypes were manufactured. These prototypes will be named A1, corresponding to the optimum with a short flexure and A2, corresponding to the optimum with a long flexure. For each mechanism, a sensitivity analysis is carried out using finite element simulation around the maxima in the CLR, and their force-deflection characteristics were measured experimentally. All parameters are summarized in Table 3.1.

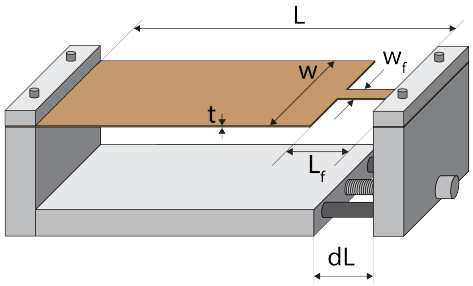

Figure 3.3: Schematic showing the important dimensions of the prototype of Mechanism A in the unloaded position. From this configuration an axial load is applied to induce the buckling of the beam.

Table 3.1: Relevant parameters of the manufactured prototypes.

Fixed parameter	**Symbol**	**Value**
Unloaded device length	L	20 mm
Axial load displacement	dL	0.4 mm
Width of wide segments	w	2 mm
Width of narrow segments	w_f	0.2 mm
Thickness of mechanism	t	100 μm
Design variables	α	L_f
Flexure length A1	0.177	3.54 mm
Flexure length A2	0.605	12.10 mm
Flexure length B	0.361	7.22 mm
Flexure length C	0.563	5.63 mm (each)

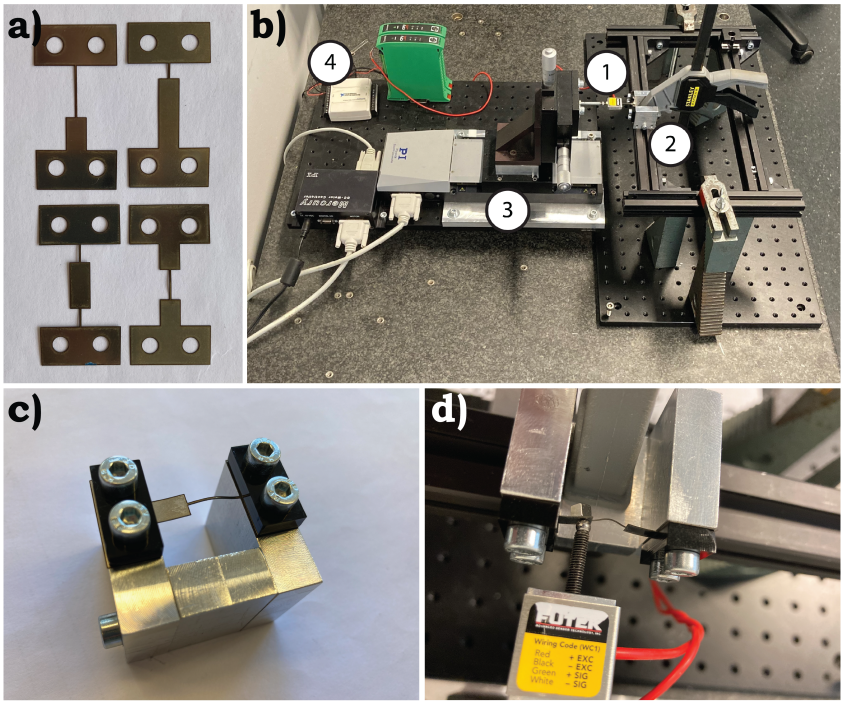

Figure 3.4: Mechanical design of a) the fabricated mechanisms and c) assembled prototype using a frame to apply axial loading and induce buckling and experimental setup for evaluation of force-deflection behavior; b) overview of components d) close-up of rolling contact and magnet at the interface of the flexure to ensure contact in the unstable region.

The beams were clamped in an aluminum frame consisting of a base plate and two sliding sides. The sides are aligned using dowel pins and can be clamped to the base by tightening the bolts on the sides. The assembly process was as follows. First, a spacer with a thickness of 0.4 mm was placed between the sides and the base of the frame and the bolts were tightened. Next, the beam was mounted to the frame by clamping it between the aluminum and a PMMA bracket. In this state the beam is stress-free and therefore not buckled. Next, the bolt on the side is released such that the spacer can be removed and is subsequently tightened again such that the sides of the frame have moved exactly the thickness of the spacer compared to the stress-free configuration. This introduces an axial preload and the beam should buckle out of plane to one of its stable positions. The assembled structure is shown in Figure 3.4(c).

FINITE ELEMENT MODEL

To simulate the mechanical behavior of the post-buckled beams a finite element model was built in ANSYS using beam elements (beam188). The

material is assumed to be perfectly elastic with the following properties (E = 190 GPa, ν = 0.34, ρ = 7.82 gcm^{-3}). Buckling was induced by constraining one end of the beam in all directions, and displacing the other end. Small imperfections were incorporated in the model to prevent the simulation to crash due to singularities in this preloading step. After the buckled shape was achieved, a displacement was applied at the interface of the flexure. During this the reaction forces are recorded at regular intervals to determine the force-deflection behavior.

EXPERIMENTAL CHARACTERIZATION

The force-deflection characteristics of the beams were evaluated experimentally with the setup shown in Figure 3.4(b). For this a FUTEK LRM200 force sensor (1) is connect to the prototype (2) and displaced by a PI M-505 motion stage (3) from which the internal encoder captures position data. Data was recorded using a NI USB-6008 (4) in 100 steps over the range of motion. The probe is fixed to the beam at the interface of the flexure using a rolling contact and a magnet as shown in Figure 3.4(d). This ensures that the probe will remain in contact with the system in the unstable region.

3.3 RESULTS

In Figure 3.5, the force-deflection relations resulting from the simulations are shown for the normalized load ($\tilde{F} = \frac{FL^2}{EI}$) and normalized deflection ($\tilde{d} = \frac{d}{L}$). Figure 3.5(a) shows the relations of the uniform beam and Mechanism A2 and identifies important characteristics of the curve. Figures 3.5(b-e) show the relations for variations in parameter α in Mechanisms A1, A2, B and C, respectively. The relative flexure length is varied by +/- 10% and +/- 20% around the optimum in CLR for each mechanism as shown in Figure 3.2. In Figure 3.6, the measured force-deflection relations are shown. In Table 3.2 the first two critical loads and the CLR is shown for the Mechanisms A1, A2, B and C at the optimum in CLR for each mechanism as shown in Figure 3.2.

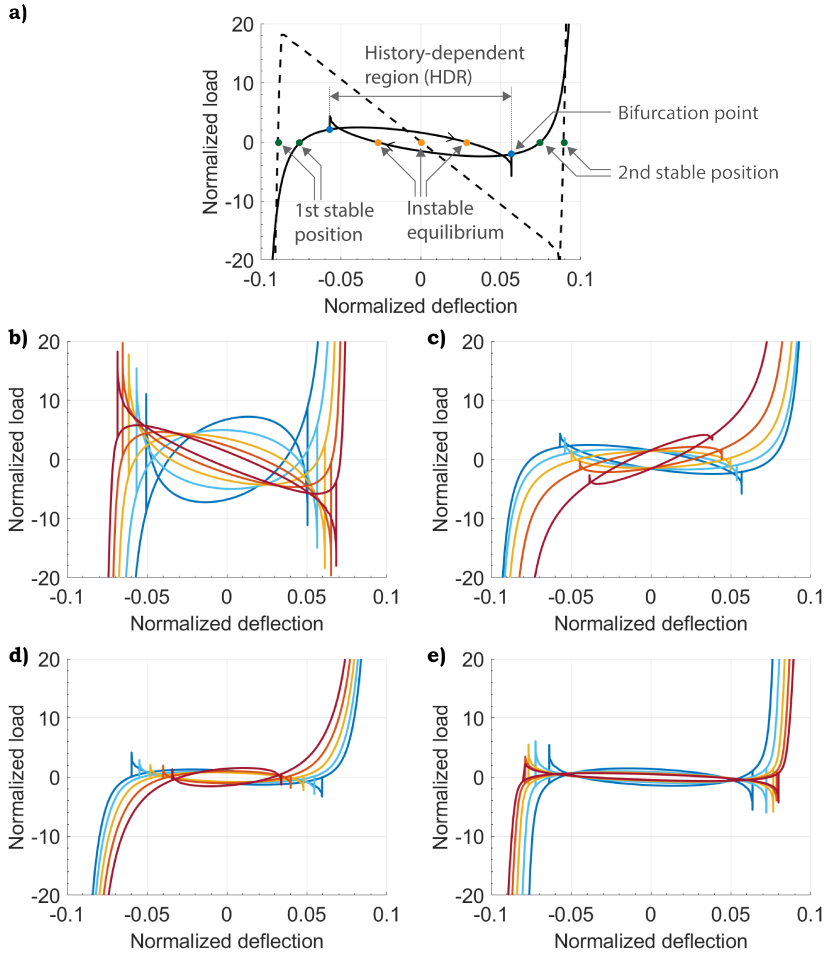

Figure 3.5: a) Identification of important points in the normalized load-deflection relation for uniform beam and Mechanism A2. b-e) Sensitivity analysis of normalized load-deflection relations of b) Mechanism A1, c) Mechanism A2, d) Mechanism B, and e) Mechanism C. The relative flexure length α is varied around the optima found in Figure 3.2(b);
— $\alpha = 0.8\alpha_{opt}$, — $\alpha = 0.9\alpha_{opt}$, — $\alpha = \alpha_{opt}$, — $\alpha = 1.1\alpha_{opt}$, — $\alpha = 1.2\alpha_{opt}$

Table 3.2: Relevant parameters of the manufactured prototypes.

Mechanism	$P_{crit,1}$ [N]	$P_{crit,2}$ [N]	CLR
A1	4.78	7.51	0.64
A2	1.64	2.6	0.64
B	3.24	3.72	0.88
C	2.07	2.67	0.78

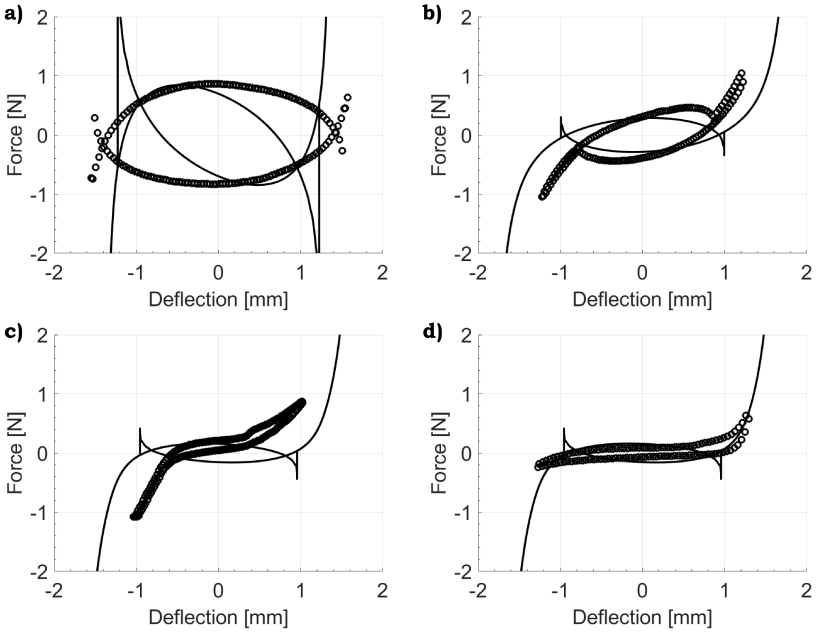

Figure 3.6: Simulated and measured force-deflection relations of a) Mechanism A1, b) Mechanism A2, c) Mechanism B and d) Mechanism C.

3.4 DISCUSSION

FORCE-DEFLECTION RELATION OF BUCKLED MECHANISMS

The nonlinear force-deflection relations of the post-buckled mechanisms shown in Figures 3.5 and 3.6 are characterized by the points identified in Figure 3.5(a). These include two stable equilibrium positions and one or more unstable equilibria. It can be observed that between the stable equilibria the mechanisms are relatively compliant, and the force-deflection relation rapidly steepens for larger displacements. This steepening effect is a result of the mechanisms being straightened and loaded in tension. In the force-deflection relations of the mechanisms, two bifurcation points can be identified between which two load paths are present, corresponding to the two configurations of the mechanisms that can be identified as “knee-up” and “knee-down”. This section of the curve between the bifurcation points is identified as the history-dependent region (HDR). When actuated from one side to the other, there is a point where the mechanisms experience a snap-through bi-stability and change configuration. The two load paths in the HDR are a result of the series configurations of the mechanism topologies and are not observed in the parallel topology used by Kuppens et al. [49]. The main difference is the rotational degree of freedom at the point where the force-deflection relation is measured.

Depending on the mechanism, there is a potential barrier which has to be overcome before the snap-through occurs. This is especially evident in Mechanism A1, and can be seen from the sharp peaks in the force-deflection relation close to the bifurcation points. In the other mechanisms, these peaks are smaller, which indicates that for these mechanisms the potential barrier is lower. Moreover, the area between the load paths in the HDR also varies for each mechanism. It can be seen that for Mechanism C the load paths are relatively close together, and for Mechanism A1 the load paths enclose a much larger area. The size of this area is a measure for the energy captured in the system before the snap-through [99]. When the load paths are further apart, more energy is required to actuate the mechanism and less balancing performance is obtained.

CRITICAL LOAD RATIO AND FORCE-DEFLECTION RELATION

Drawing a line between the bifurcation points finds a general trend in the slope of the HDR, which can slope upwards, slope downwards or can be relatively flat. For Mechanisms A2, B and C it can be observed from Figure 3.5 that mechanisms with an increasingly upwards sloping HDR are obtained when $\alpha > \alpha_{opt}$ and mechanisms with increasingly downwards sloping HDR are obtained for $\alpha < \alpha_{opt}$. Moreover, for these mechanisms the flattest slope of the HDR is obtained at $\alpha = \alpha_{opt}$ (i.e. where the CLR is maximized). Therefore, the CLR can in these cases be used as a tool for finding the design variables that lead to a the greatest degree of static balancing. However, in Mechanism A1 the flattest slope was not found at $\alpha = \alpha_{opt}$, and the opposite effect is observed for the slope of the HDR.

Moreover, the value of the CLR can also give information on how well the mechanisms can be balanced, as the CLR is a measure to identify the variation of potential energy in the buckled system between the stable and the unstable equilibria. Therefore, if a CLR = 1 can be achieved a mechanism is expected to be statically balanced between the stable and unstable equilibrium positions. Not all mechanisms can be statically balanced, but in that case it is expected that when the CLR is maximized a design is obtained with a load-deflection relation closest to statically balanced. It can be observed that the maxima of the CLR curves have greater values for Mechanisms B and C compared to A1 and A2. As a result, these mechanisms have their load paths closer together, require lower actuation forces and therefore show a better balancing performance. However, it is important to note that the CLR only gives a ratio between the variation of potential energy, and it is important to consider the actual values of the critical loads too. As can be found from Table 3.2, the critical loads of Mechanisms A1 and B are greater than the critical loads of Mechanisms A2 and C, respectively. Therefore, the CLR of A1 and A2 may be quite similar while A2 clearly shows a better balancing performance. A similar results was found for Mechanisms B and C, where the CLR of B is higher, but due to the lower critical loads a better balancing performance is found in C.

USAGE OF THE BEAMS AS BUILDING BLOCKS FOR SBCOMS

When the Mechanisms A, B, C are to be used as building blocks for SBCOMs, it is necessary to prevent the rotation of the actuation point to achieve CLR = 1 and the desired static balancing. This can for example be achieved by designing an ortho-planar platform by arranging three of these mechanisms in a rotationally symmetric way and connecting their actuation points. As a result, the rotation is prevented by the added stiffnesses of the two other elements. However, this arrangement requires some modifications to the building blocks in order to relax the in-plane displacements at the actuation point to prevent over-constraints.

3.5 CONCLUSION

In this paper we have proposed and demonstrated a method to tune the force-deflection behavior of buckled mechanisms based on a linear buckling analysis. Through locally manipulating the flexural rigidity of a beam over part of its length, the ratio between the first two critical loads of the mechanism can be tuned. Maximizing this ratio results in the best balancing performance for a given mechanism. A sensitivity analysis was conducted through finite element simulation and the results were validated experimentally. These proposed mechanisms can be used building blocks for statically balanced compliant ortho-planar mechanisms.

4 MEMS IMPLEMENTATION IN FLEXIBLE TRANSDUCERS

There is a high demand for novel flexible micro-devices for energy harvesting from low-frequency and random mechanical sources. The research of new functional designs is required to strategically enhance the performances and to increase the control on mechanical flexibility. In this work we report the fabrication and characterization of bi-stable and statically balanced thin-film piezoelectric transducers based on Aluminum Nitride (AlN). The device consists of a piezoelectric layer sandwiched between two thin Molybdenum electrodes that were deposited on a Kapton substrate by reactive sputtering and patterned by UV lithography. In order to improve the out-of-plane flexibility, the mechanical design is distinguished by a post-buckled flexure that introduces a negative stiffness to compensate the otherwise positive stiffness of the system. The buckling was introduced by a new method, called Package-Induced Preloading (PIP) where the mechanisms are laminated over a package with a geometry extending out-of-plane. The induced buckling resulted in bi-stable and statically balanced mechanisms which demonstrated an enhanced voltage output during a triggered snapping step. A preliminary study shows potential for the statically balanced designs and the PIP method for wind energy harvesting, revealing prospective applications and future improvements for the development of energy harvesters.

4.1 INTRODUCTION

Mechanical energy harvesting is a promising field that, in the last decades, has led to the development of novel micro-devices for scavenging energy from unexploited sources, such as ambient vibrations, tiny motions of the human body or low-speed fluid flows. Among the most commonly adopted transduction mechanisms for energy harvesting, the piezoelectric effect has attracted a huge interest, especially if combined with properties such as mechanical flexibility, adaptability and bio-compatibility [35, 43, 101–108].

This chapter originally appeared as T.W.A. Blad*, M. Mariello*, V.M. Mastronardi, F. Madaro, F. Guido, U. Staufer, N. Tolou, M. De Vittorio, *Flexible piezoelectric AlN transducers buckled through package-induced preloading for mechanical energy harvesting* in Nano Energy 85 (2021) [100].
*Co-first author

Piezoelectric materials directly convert applied strain energy into electrical energy and exhibit high output power densities [25, 43], both, in the form of nanostructured materials [102–104] or as thin films [105–108] . Among well-known piezoelectric thin films (Lead-Zirconium-Titanate [PZT], Zink-Oxide [ZnO], Polyvinylidene fluoride [PVDF], Lithium Niobite [$LiNbO_3$]), Aluminium Nitride [AlN] is a suitable candidate for the development of energy harvesters for low-frequency mechanical sources due to its CMOS-fabrication compatibility, the good piezoelectric properties [109–112], and the ability to be deposited as very thin film (~ 1 µm) onto soft/flexible [113–118] substrates by relatively low-temperature processes such as reactive sputtering [119]. Moreover, as discussed in previous works [110, 120, 121], the material has a low dielectric constant (~ 9-11), high electromechanical coupling coefficient (~ 0.21), high temperature and humidity-resistance [121], and bio-compatibility [35, 121], and does not need poling [113].

According to the most common theoretical models for energy harvesters [3, 16, 122], the highest efficiency is attained at resonance, when the natural frequency of the generator is matched to the dominant frequency of the driving motion. However, for low-frequency high-amplitude motion, resonance may not be optimal for the highest efficiency due to the limited available space [3, 58].

A number of low-frequency MEMS energy harvesters were demonstrated in literature. The design of Liu et al. [67], which featured a PZT cantilever designed in a S-shape, was able to harvest 1.12 nW at its resonant frequency of 27.4 Hz. In the work of Liu et al. [123] a spiral shaped PVDF cantilever was used to harvest 8.1 nW at the resonance frequency of 20 Hz. It was shown that next to the functional properties of the piezoelectric material, the output of piezoelectric energy harvesters greatly depends on the optimization of the system architecture [124–131]. This includes the use of mechanical design principles, such as the use of proof masses or buckling effects [132, 133]. Yang et al. [133] studied the buckling effect and proposed a flexible energy harvester consisting of a PVDF film attached to a shell-shape substrate for energy harvesting from human motion. The folding-unfolding of the curved, pre-stressed substrate provides an increased output power in comparison to a simple flat structure. Dong et al. [134] presented a piezoelectric device, which integrates a buckled beam array design with a porous Poly(vinylidene fluoride-trifluoro ethylene) [PVDF-TrFE] thin film, for energy harvesting from cardiac motion. The maximum output open-circuit voltage and short-circuit current of the device are 4.5 V and 200 nA, respectively, with a peak-power of 49 nW at an optimal resistor load of 50 MΩ. Tao et al. [135] fabricated a thermally induced bi-stable plate made of a carbon nanotube-reinforced composite with integrated piezoelectric patches for broadband energy harvesting. Guido et al. [113] proposed a pre-stressed structure [PSS] based on sputtered AlN thin films, as a piezoelectric skin for energy harvesting from folding/unfolding on human fingers. The pre-stress

leads to a six-fold enhancement of the generation performances with a resulting peak-to-peak voltage of 0.7 V.

A recently adopted method to optimize the architecture of micro-devices exploits the use of negative stiffness to facilitate multi-stable systems or statically-balanced compliant micro-mechanisms [SBCM] [129, 134, 136]. A MEMS oscillator based on SBCM is demonstrated by Middlemiss et al. [94]. It features a proof mass on top of an anti-spring mechanism. With increasing displacement, the anti-spring softened and the system was able to reach a resonant frequency of 2.3 Hz in the vertical orientation. Another SBCM was developed and studied by Tolou et al. [95]. This mechanism was fabricated using deep reactive-ion etching and achieved a near zero stiffness characteristic over a small range of motion. Kuppens et al. [49] demonstrated a SBCM in which the preloading was induced by a MEMS compatible thin film process. The resulting mechanism combined the positive stiffness of a linear guidance mechanism with a post-buckled flexure to achieve static balancing. However, these methods are based on rigid substrates, thermal processes, or mechanical springs for reducing the stiffness, which are not suitable for achieving static balancing in very flexible transducers, therefore new approaches are needed.

In this work, we report on the development of a bio-compatible and lightweight prototype of a flexible energy harvester for low-frequency motions, e.g. for wind energy harvesting. The aim is to combine flexible piezoelectric transducers with the design principles of SBCM to build bi-stable and statically balanced devices that allow for very easy out-of-plane motions. The force-deflection relations were simulated using Finite Element Methods (FEM) and experimentally validated. Prototypes were fabricated with piezoelectric thin films of AlN deposited by reactive DC sputtering onto a soft substrate. The preloading of the device is based on a new approach, hereafter called package-induced preloading (PIP), which allows to induce buckling effects on flexible substrates by exploiting a monolithic support (package) 3D-printed at high-resolution. The prototypes have been characterized to assess the voltage and current generation properties.

4.2 METHODS

MECHANICAL DESIGN

The piezoelectric transducer is shown schematically in Figure 4.1 and consists of a Kapton substrate and a piezoelectric material sandwiched between two electrodes. The following parameters can be identified; the thickness of the Kapton substrate, t_s (25 µm), the thickness of the AlN piezoelectric material, t_{AlN} (~ 1 µm), and the thickness of the Molybdenum (Mo) electrodes, t_e (~ 200 nm). The total thickness of the piezoelectric sandwich is therefore given by $t_p = t_{AlN} + 2t_e$. The choice of Mo as electrode material is due to its properties and suitability for the AlN deposition.

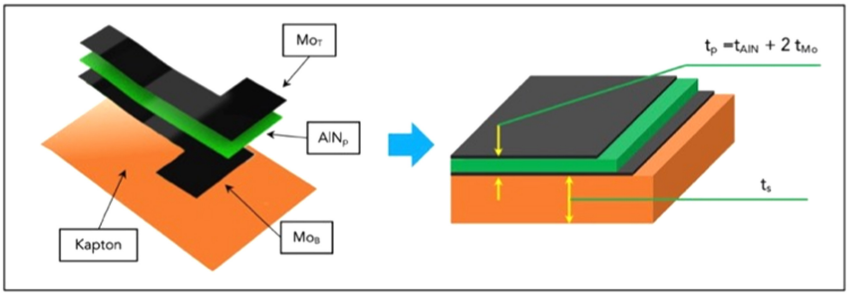

Figure 4.1: Stacking sequence of deposited layers for the AlN-based flexible transducers. The right image shows the thickness parameters for the active AlN/Mo structure and for the Kapton substrate.

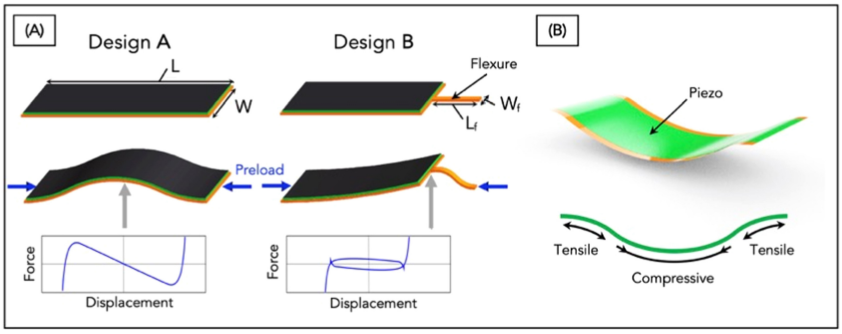

Figure 4.2: (A) Comparison between the standard full configuration (design A) and the modified configuration (design B). The different mode shape for the preloaded device is depicted for the two designs as well as the corresponding force-deflection relations. (B) Charge cancellation effects due to symmetric distribution of stresses in the design A.

Figure 4.2(A) shows the schematic view of the mechanism designs of the piezoelectric energy harvesters and their components. The initially flat mechanisms can be buckled by applying an axial load: this process is called preloading and results in the mechanisms assuming an out-of- plane post-buckled shape. In this post-buckled configuration, design A is a bi-stable mechanism which has a negative stiffness between the stable equilibria. In this design, a significant force must be exerted on the mechanism in order to move it through the unstable equilibrium. In order to achieve a more flexible system, static balancing can be used as a passive method to reduce the stiffness [136]. To achieve static balancing, the common approach is to add a balancer element to the mechanism in order to counteract the forces of the functional mechanism. Such a balancer should have a stiffness opposite to the stiffness of the functional mechanism [49]. In this case, the balancer element can be obtained by selectively removing material, resulting in design B. In particular, material is removed from design A over a part of the length of the mechanism such that only a narrow section (i.e. a flexure) remains. Moreover, the piezoelectric sandwich

is also removed from the flexure. As a result, the post-buckled mechanism is much more compliant and it is identified as statically balanced compared to design A. Essentially, design B consists of two sections of different widths in series. During the preloading, the buckling is concentrated in the flexure due to its lower critical load. This provides a negative stiffness which compensates the positive stiffness of the wide section. The force-displacement relations of designs A and B are sketched in Figure 4.2(A). Besides enhancing the flexibility of the system by lowering the buckling load and reducing the stiffness (slope in the curve), the buckled shape of design B is asymmetric such that voltage cancellation as a result of opposing stresses in the piezoelectric layer is prevented, as occurs instead in design A (Figure 4.2(B)). The following parameters were used in the designs. In both designs the unloaded devices share the same length, L, and width, W. Additionally, in design B the flexure length, L_f, and flexure width, W_f can be identified.

In order to apply the preload, the clamping-points of the ends of the mechanisms must be moved closer to each other. In this work a new method is proposed and implemented for preloading the flat mechanisms. First, a frame was designed around the mechanism to connects its ends. The mechanism and frame are monolithically fabricated together on the same substrate. Next, the frame was laminated over a structure with a geometry extending out of plane (i.e. the package). Folding the frame over the package shortens the in-plane distance between the ends of the mechanism. This distance is reduced to the cord length of the out-of-plane curve along which the frame is folded and is smaller than the initial length L of the mechanism. It is important to note that the mechanism itself is not folded, but assumes one of its equilibrium out-of-plane positions. This process can easily be integrated in a packaging process; hence this method is proposed as package induced preloading (PIP) and is shown in Figures 4.3(A)(i–ii).

The proposed design for the package shown in Figure 4.3(B) consists of ribs extending out-of-plane. The ribs are designed by tracing a path that follows three arcs with equal radii, R, in an up-down-up pattern as shown in Figure 4.3(B). As a result, the absolute value of the curvature is constant over the whole curve. The preloading displacement, dL, is defined as the difference between the initial length L, of the mechanism, and the new, after-packaging straight length (or shortened length) D, and is given by the following equation, as a function of the radius and length.

$$dL = L - D = L - 4R\sin(\frac{L}{4R}) \tag{4.1}$$

Moreover, the equilibrium positions x_{eq} of the post buckled symmetric mechanism (design A) shown in Figure 4.3(C) can be easily found as approximately equal to the height H of the ribs according to the following formula.

$$x_{eq} = 4R\sin^2(\frac{L}{8R}) \approx \frac{L}{\sqrt{6dL/L}}\sin^2(\frac{\sqrt{6dL/L}}{2}) \tag{4.2}$$

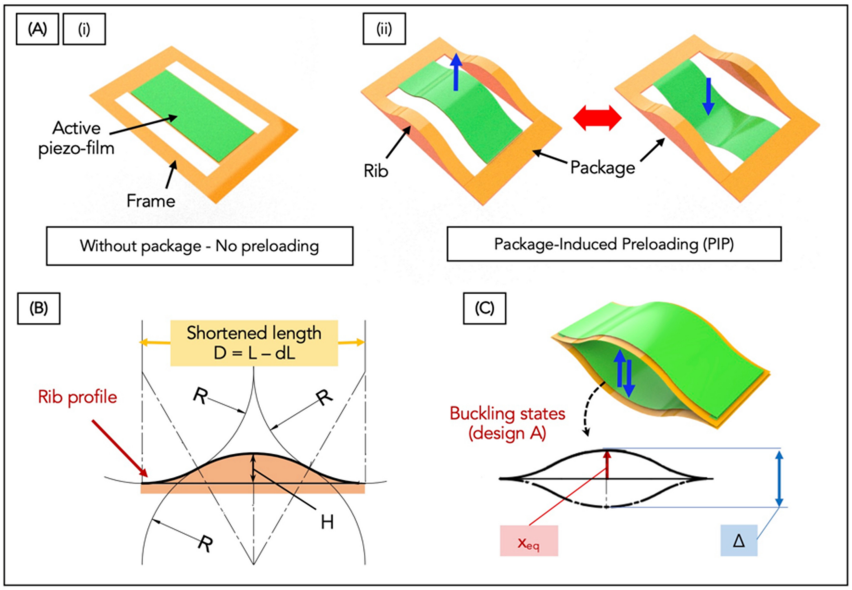

Figure 4.3: (A) Conceptual scheme of Package-induced Preloading (PIP): (i) flat flexible transducers without package: no buckling or preloading occurs. (ii) Package-Induced Preloading (PIP) due to properly designed package, with out-of-plane ribs. (B) Profile of the curved frame (rib) (i) with indication of the geometrical parameters used in sizing and the theoretical amplitudes of the buckling states for design A (ii).

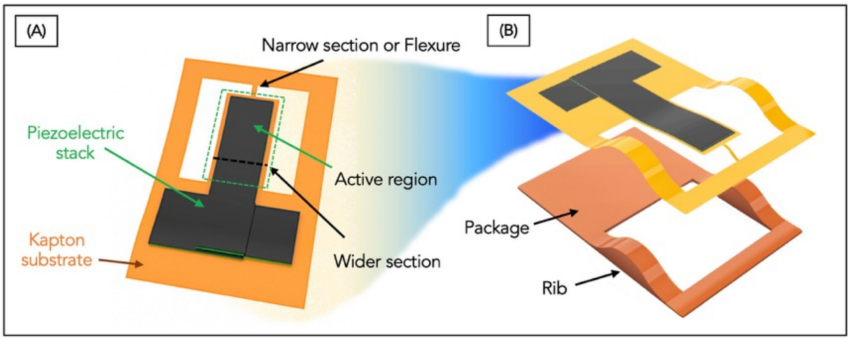

Figure 4.4: (A) Design for the planar mechanism, consisting of Kapton substrate and a proper active piezoelectric area, with indication of the main parameters. (B) Exploded view of the planar mechanism on the package used in this work.

Therefore, the predicted out-of-plane range of motion for this buckling structure is given by the following expression.

$$\Delta = 2x_{eq} \tag{4.3}$$

The aforementioned parameters for the mechanism of design B are more complex and require computational simulations to be calculated.

Figure 4.4(A) illustrates the planar mechanism B with indication of the components, whereas Figure 4.4(B) reports an exploded view of the final PIP device, representing the whole system comprising transducer, mechanism and package. In Table 4.1 the complete list of geometrical parameters for the fabricated PIP prototypes is reported. Multiple versions of design B were fabricated in which the lengths of the flexure and the piezoelectric area were varied. The motivation for this was not to perform an optimization of these design parameter for a particular application, but rather to allow a preliminary investigation on the performances of different design variations. The nomenclature that will be used to identify the variations in the design is set as follows. B1-B4 are variations of design B, where $L_S = L - L_f$ is the length of the wide section. B1 and B2 stand for the devices with a full piezoelectric area with short and long Kapton flexure, respectively. B3 and B4 correspond to devices where the piezoelectric area covers only part of the wide section namely for up to the length L_p. The uncovered Kapton area of width W and length $L_S - L_p$ is called collector area.

FABRICATION

Silicon wafers were used as support for the sputter-deposition of the piezoelectric stack. PolyDiMethyl Siloxane (PDMS) (Sylgard 184 Silicone Elastomer) was supplied by Dow Corning Corporation in two compounds: a viscous uncured pre-polymer and a curing agent. Kapton HN 25 µm-thick foils were supplied by DuPont. The rigid frame was 3D-printed utilizing a dielectric ink (Dielectric Nanoparticle Polymer Ink) for the insulating support. A double-adhesive tape (3M ECATT 9703) was used for assembling the device.

Table 4.1: Geometrical parameters of the fabricated PIP prototypes.

Parameter	**Symbol**	**Value**				
Transducers						
Substrate thickness (µm)	t_s			25		
Piezo stack thickness (µm)	t_p			1.6		
Mechanisms		A	B1	B2	B3	B4
Flexure length (mm)	L_f	-	1.9	7.9	4.9	1.9
Flexure width (mm)	W_f	-	0.38	0.38	0.38	0.38
Wide section length (mm)	L_s	15	13.1	7.1	10.1	13.1
Wide section width (mm)	W	7	7	7	7	7
Piezo length (mm)	L_p	15	13.1	7.1	7.1	7.1
Package						
Rib radius (mm)	R			5		
Rib height (mm)	H			2.7		
Preloading displacement (mm)	dL			1.5		
Shortened length (mm)	D			13.5		

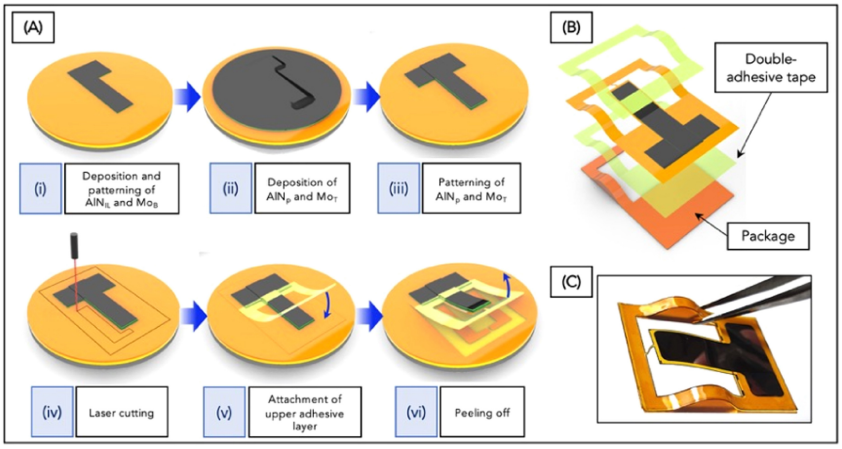

Figure 4.5: (A) Detailed fabrication and assembly process of the PIP devices. (i) Deposition and patterning of AlN interlayer and Mo bottom electrode. (ii) Deposition of AlN piezoelectric layer and Mo top electrode. (iii) Patterning of AlN piezoelectric layer and Mo top electrode. (iv) Laser cutting. (v) Attachment of adhesive layer. (vi) Peeling off. (B) Attachment of the flexible structure onto the 3D printed package through double-adhesive tape (C) Real photo of a PIP device after the fabrication and assembly process.

The realization of the thin-film piezoelectric transducers followed a previously reported microfabrication process [113, 114, 137, 138]. In brief, the Kapton substrate was attached to a silicon wafer using ~ 162 µm-thick PDMS spin-coated at 500 rpm for 30 s, degassed under vacuum to remove entrapped residual air-bubbles, then cured at 90°C for 15 min. The piezoelectric stack was deposited by reactive sputtering (K.J. Lesker Lab 18 system) in two single runs in order to minimize contaminations. A 120 nm-thick AlN interlayer and the bottom Mo-electrode (200 nm) were deposited in a single step and patterned by optical UV lithography and chemical etching (Figure 4.5(A)(i)). In a similar way, the AlN piezoelectric layer (~ 1 µm) and the second top Mo-electrode (200 nm) were deposited in a single run by sputtering (Figure 4.5(A)(ii)) and subsequently patterned through dry etching with Inductively-coupled Plasma-Reactive Ion Etching (ICP-RIE) system (Figure 4.5(A)(iii)). The residual stress induced in the deposited thin-film stack is due to the temperature reached during the sputtering process: up to ~ 70°C and to ~ 165°C for the Mo and AlN steps, respectively.

A CO_2 laser micro-machining system (from Universal Laser Systems, VLS2.30) has been employed to perform the laser cutting process on Kapton (Figure 4.5(A)(iv)). The laser process parameters were optimized to ensure a smooth cut- through performance and clear releasing of samples [139]. In particular, a laser power of 9 W, a scanning speed of 63 m min^{-1} and a pulse density of 750 ppi were adopted. Afterwards, the devices were immersed in Isopropyl Alcohol and ultrasonically cleaned for 30 s, to remove any traces of

carbonaceous residues resulting from the ablation of polyimide [140, 141]. The package was printed by a multi-layer 3D PCB printer (DragonFly LDM System, Nano Dimension) and used as support for the flexible piezoelectric transducers. The 3D printing process took approximately 6 h and it consisted of inkjet printing and curing simultaneously a dielectric ink at ~ 70 °C. The final devices were assembled as illustrated in Figures 4.5(A)(v, vi) and Figure 4.5(B): a double-adhesive tape was shaped by laser cutting, aligned and attached onto the 3D printed frame. Subsequently, the AlN-based flat transducers were laser-cut and peeled off from the PDMS/Si substrate with the aid of an upper adhesive tape (Figures 4.5(A)(v, vi)). Finally, the free-standing transducers were allowed to slowly adhere onto the double-adhesive tape (Figure 4.5(B)). The electrical connections were made on the exposed pads of the bottom and top electrodes, by using an adhesive Copper (Cu) tape, rivets and electrical wires: Silver paste and soldering Tin were used to improve the conduction of the connections. Figure 4.5(C) reports a real photo of a PIP device after the entire fabrication process.

SIMULATIONS

To simulate the mechanical behavior of the buckled structure a finite element model was built in ANSYS using beam elements (beam188). The composite cross-sections of the piezoelectric transducers were modeled as cross-sections of a custom uniform material. Equation (4.4) was used to determine the elastic modulus such that the flexural rigidity of the custom-material cross section matched that of the composite cross-section using the parallel axis theorem:

$$EI_{eq} = \sum_{n}^{N} \frac{E_n w t_n^3}{12} + E_n w t_n y_n^2 \tag{4.4}$$

Where y_n is the distance with respect to the neutral axis of the middle axis of the composite cross section; E_n, t_n are the Young's modulus and the thickness of the n^{th} layer, respectively. The materials are assumed to be perfectly elastic with the properties listed in Table 4.2.

Buckling was induced by constraining one end of the mechanism in all directions, and moving the other end by the same amount as expected from the PIP. Small imperfections were incorporated in the mechanism to prevent the simulation to crash due to singularities in this preloading step. After the buckled shape was achieved, a displacement was applied to the node with

Table 4.2: Materials properties used for FEM simulations; ρ mass density; E Young's modulus; ν Poisson's ratio.

Material	**Properties**	**Ref**
Kapton	ρ = 1.42 g/cm3; E = 2.5 GPa; ν = 0.34;	[142]
AlN	ρ = 3.26 g/cm3; E = 330 GPa; ν = 0.22;	[110, 111, 114, 143, 144]

the maximum out-of-plane displacement to flip the mechanism to its other stable configuration. During this, the reaction forces are recorded at regular intervals to determine the force-deflection behavior.

MECHANICAL AND ELECTRICAL CHARACTERIZATION

For measuring the out-of-plane force-deflection behavior of the fabricated devices, the measurement setup reported in Figures 4.6(A)(i–ii) was used. A micro-force sensing probe (FUTEK LRM200) with a resolution of 0.5 μN (1) is mounted on the mechanism (2) and displaced by a precision linear stage (Physik Instrumente M-505) with a resolution of 8.5 nm (3), from which the internal encoder captures position data. Data was recorded using a NI USB-6008 (4) in 250 steps over the range of motion.

The electrical properties (impedance, phase, capacitance) of the thin-film piezoelectric stack were measured by connecting the device to an Agilent E4980A Precision Inductance-Capacitance-Resistance (LCR) meter and performing frequency sweeps.

The devices were evaluated by mechanically triggering the snapping state of the fabricated devices at ~ 1-2 Hz and by detecting the open- circuit voltage with an oscilloscope (Textronix MDO 4104-3). The applied load for these tests consisted of a mechanical stimulus triggered by a linear micro-actuator (by Actuonix Motion Devices Inc., L16-R, 100 mm, 35:1, 6 Vdc), which served to allow the fast snapping transition between the two equilibrium positions of the bi-stable element.

The 3D printed frames were characterized in terms of mechanical strength and flexibility, since they serve as support for the flexible transducers, thus they must be lightweight and resistant to some extent. Dynamic mechanical analysis (DMA) measurements were performed in controlled force mode (force rate 1 $\mathrm{N\,min^{-1}}$) with a Q800 instrument (TA Instruments).

APPLICATION TESTING

To demonstrate the potential of the flexible PIP devices for low- frequency energy harvesting applications, their performance was stud-ied in a custom setup for wind energy harvesting. The setup is shown in Figures 4.6(B)(i–iii): it is based on a standard suction subsonic wind tunnel (provided by TQ TecQuipment), with a working section of 30.5 x 30.5 $\mathrm{cm^2}$ and 60 cm long, enclosed by acrylic side-walls. A custom-built setup based on an Arduino-controlled stepper motor allows to set speed parameters from a suitable computer, up to 20 $\mathrm{m\,s^{-1}}$ (Figure 4.6(B)(iii)). In particular, a wind speed ramp has been set in the range 0-20 $\mathrm{m\,s^{-1}}$ with a step of 2.5 $\mathrm{m\,s^{-1}}$ for a time interval of 5 s. Inside the working space of the wind tunnel, the devices are fixed between two halves of a bluff body (Figure 4.6(B)(ii)). The aim of the bluff body, according to the theory of flow by T. von Karman [145], is to induce a flow separation and to generate a Karman vortex street downstream of the body itself. The forces resulting from shedding vortices and periodic

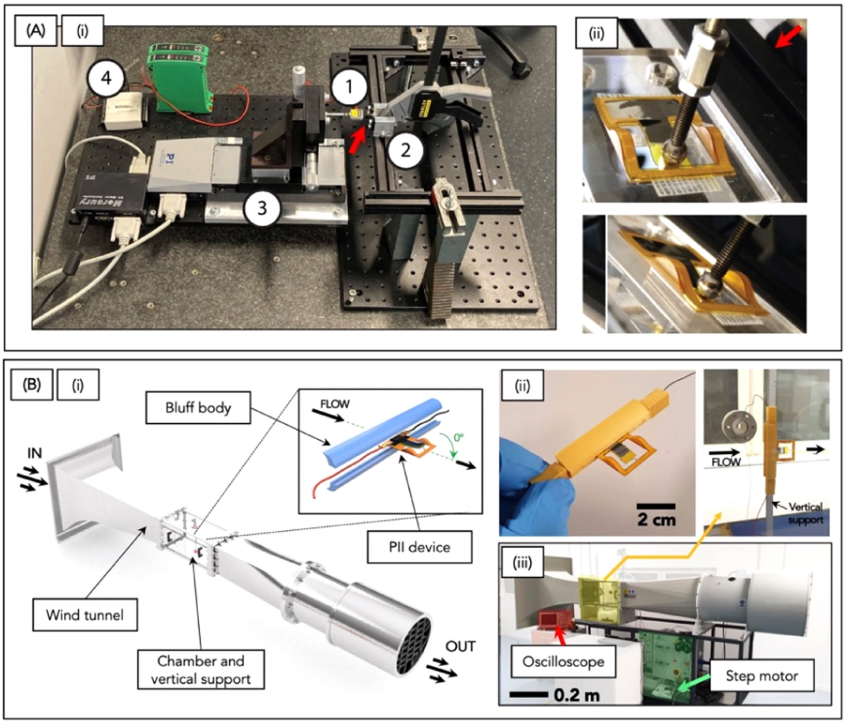

Figure 4.6: (A) (i) Photo of the force-deflection measurement setup with (1) microforce sensing probe, (2) mechanism, (3) precision linear stage, (4) data recorder. (ii) Closeup of a real sample being tested. (B) Wind tunnel setup employed for wind energy harvesting tests (i), with the PIP device fixed inside a 3D printed bluff body (ii). The position and direction of the device with respect to the wind flow are indicated. The step motor allows the controlled variation of wind speed and the oscilloscope is used to detect the signal from the device (iii).

pressure gradients are responsible of the periodic vibration/oscillation of the structure attached to the bluff body [146]. The bluff body has a reverse C cross section because it has been demonstrated as the best shape to optimize the generation of vortices downstream of the device [142, 143, 147]. The transversal pressure variation, $\triangle p$, can be determined in terms of pressure fluctuation coefficient, $C_p = \triangle p/(12\rho v^2)$, where ρ, v are the air density and the free-stream wind speed [144, 148]. Specific aerodynamic experimental studies would be necessary to obtain spatial distribution spectra of C_p. The effective area interested by the pressure fluctuations is the area of the oscillating element, i.e. $L_s * W$. The mechanical strain energy periodically induced in the flexible structure is then converted into electrical energy by the direct piezoelectric effect.

Therefore, the bluff body has three functions: (i) it acts as splitter for the incoming airflow, generating vortices and turbulences, (ii) serves as a fixed clamp for the device; and (iii) it contains and protects the electrical wires

that are feed to the outside of the wind tunnel through the acrylic side-walls of the working section. The devices are positioned parallel to the airflow (i.e. at 0 deg with respect to the flow direction), downstream of the bluff body. Addition-ally, in order to avoid edge effects, they are placed at middle height of the working section and at 20 cm from the inlet.

The power curves were obtained by measuring the voltage drop on different resistive loads connected to the devices. The maximum power is reached when the device is electronically terminate with an optimal load that matches its electrical impedance [149].

4.3 RESULTS AND DISCUSSION

FABRICATED PROTOTYPES

The sputter-deposition of AlN onto the Kapton substrate has produced a crack-free, 1 μm-thick, transparent piezoelectric film. It was observed that the columnar arrangement of the AlN-nanograins along the c-axis(0002) direction yields a wurtzite-phase polycrystalline lattice. This result is strictly affected by the sputtering process and also by the nature of the metal substrate. The choice and effect of Mo as metal electrode is based on previous works [109, 150–153].

The surface of the Kapton structure proved clean and undamaged after laser cutting, allowing a smooth and debris-free peeling from the Si substrate. After fabrication, the 3D printed package exhibits a high compliance maintaining the necessary robustness to act as mechanical support, thus it is suitable for the fabrication and assembly of lightweight and flexible energy harvesters.

The final PIP devices, after cutting and assembly, are illustrated in Figures 4.7(A)(i,ii), whereas Figures 4.7(B)(i–v) summarize the different designs tested in this work, in order to evaluate the influence of some geometrical parameters, i.e. the length of the piezoelectric area and the length of the narrow Kapton flexure. The pictures of the transducers after peeling and of the devices after assembly are reported together with the nomenclature used for referring to each design.

FORCE-DEFLECTION MEASUREMENTS

The force-deflection relations of the mechanisms are shown in Figure 4.8 for the simulation and the experiment. From the figure it can be observed that the flexibility for devices B1-B4 is improved compared to device A, due to the lower stiffness (Figure 4.8(A)(i)). Figure 4.8(A)(ii) shows in a magnified view an overlapping comparison of the force-deflection curves for the other designs (B1-B4).

Figure 4.8(B) demonstrates a typical theoretical force-deflection relation of a bi-stable system (black curve). Three equilibrium positions are found on the curve where force is equal to 0. Two of these positions (i.e. points 1 and 4)

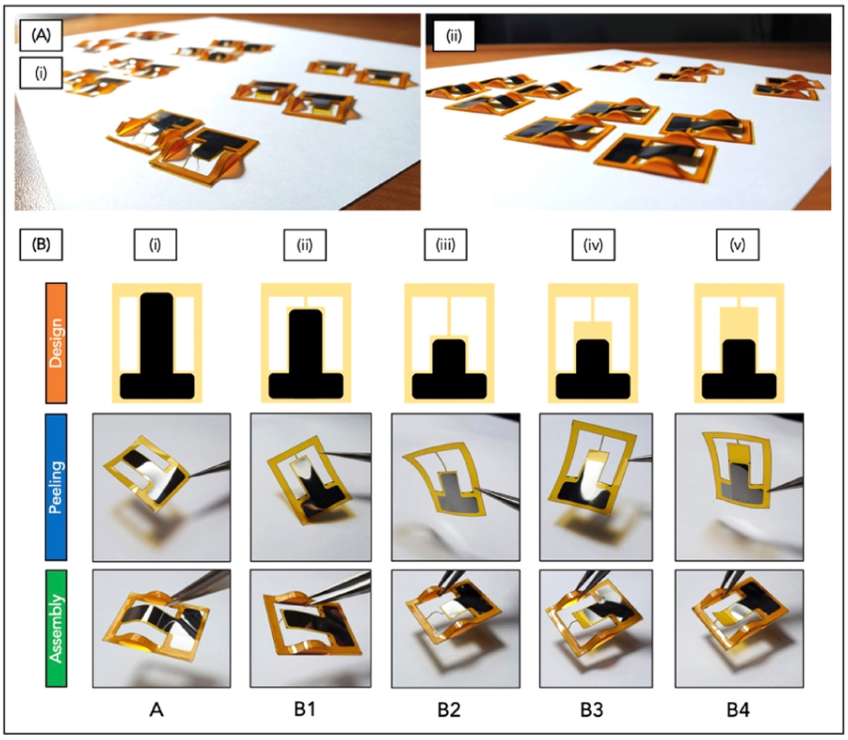

Figure 4.7: (A) (i, ii) Assembled PIP devices with different designs for the piezoelectric transducers. (B) Several tested designs with different geometrical parameters: design, pictures of the transducers after peeling and picture of the assembled PIP devices. The nomenclature of the designs (A, B1-B4) is set as follows. (i) Design without narrow stripe (design A). (ii) Design with a long piezoelectric area (design B1). (iii-iv) Design with a short piezoelectric area with different lengths for the Kapton narrow stripe, i.e. long (B2), intermediate (B3) and short (B4), respectively.

are stable equilibria where the system has a positive stiffness, and the other position is an unstable equilibrium (i.e. point 3) where the system has a negative stiffness. Moreover, in point 2 a maximum in the force-deflection relation can be found, which is identified as the switching point [99]. When the system is loaded past the unstable equilibrium, snap-through occurs and pulls the system to the opposite stable configuration.

The force-deflection relations of the post buckled devices A and B1- B4 are reported for each design in Figure 4.8, whereas as reference a similar typical curve is illustrated in Figure 4.8(B) (green curve). These curves show two bifurcation points between which two load paths can be identified (i.e. points 5 in Figure 4.8(B)). This section of the curve between the bifurcation points is identified as the low-stiffness region (LSR). It can be observed that, outside the LSR, the force-deflection relation rapidly steepens. This steepening effect is a result of strain hardening, which occurs because the devices are straightened and loaded in tension. The two load paths within

the LSR correspond to the two configurations of the system that can be identified as “knee-up” and “knee-down” and are present due to the rotational degree of freedom at the point where the force-deflection relation is measured. The peaks that are found in the simulated responses are the result of the snap-through behavior that occurs when the system changes between the configurations. In Figure 4.8(C) the force-deflection relation of the bi-stable device A is shown, which acts as a reference for the statically balanced designs B1-B4. It can be observed that the force at the switching point of device A is 16 mN and that the device has a range of motion of almost 6 mm between the equilibrium positions. Figures 4.8(D,G) show the force-deflection relations of devices B1 and B4 respectively, where the force at the switching point was reduced to 7 mN and 2 mN, respectively, as a result of the narrow flexure. However, in these devices the range of motion is reduced to approximately 3 mm and 3.5 mm. Figures 4.8(E,F) demonstrate the force- deflection relations of the designs B2 and B3. A force at the switching point of 2 mN and a range of motion of 3 mm were found for Device B3. Device B2 was found to have a single equilibrium position at 0 mm and very slight positive stiffness. From Figure 4.8 it can be observed that the effect of static balancing using the narrow flexure was demonstrated to result in more flexible systems, and that in most cases the simulated force-deflection relations show good correspondence to the measurements. The most apparent differences between simulation and experiments are discussed next.

In general, slightly larger forces were experimentally measured compared to the simulated results, which can be explained by deviations in material properties and dimensions as a result of fabrication. Additionally, some measurements show asymmetry in their force-deflection relations while all simulations are symmetric. This is particularly evident in the bi-stable device shown in Fig. 8C. The main reason for this is that the system is modeled as a custom uniform material, where in reality the cross-section is built from multiple layers with different properties. While this should not directly lead to an asymmetric force- deflection relation, the combination with residual stresses in some of these layers as a result of the fabrication process is very likely to cause this asymmetry. Moreover, the probe that was used during the measurements has a finite size and therefore it was not possible to actuate the devices exactly at the interface between the wide and narrow sections. Lastly, in devices B3 and B4 visual clues of residual stresses as a result of the fabrication process were observed in the wide Kapton sections between the AlN and the narrow flexure. This can explain the mismatch between the simulated and measured force-deflection curves particularly for these devices.

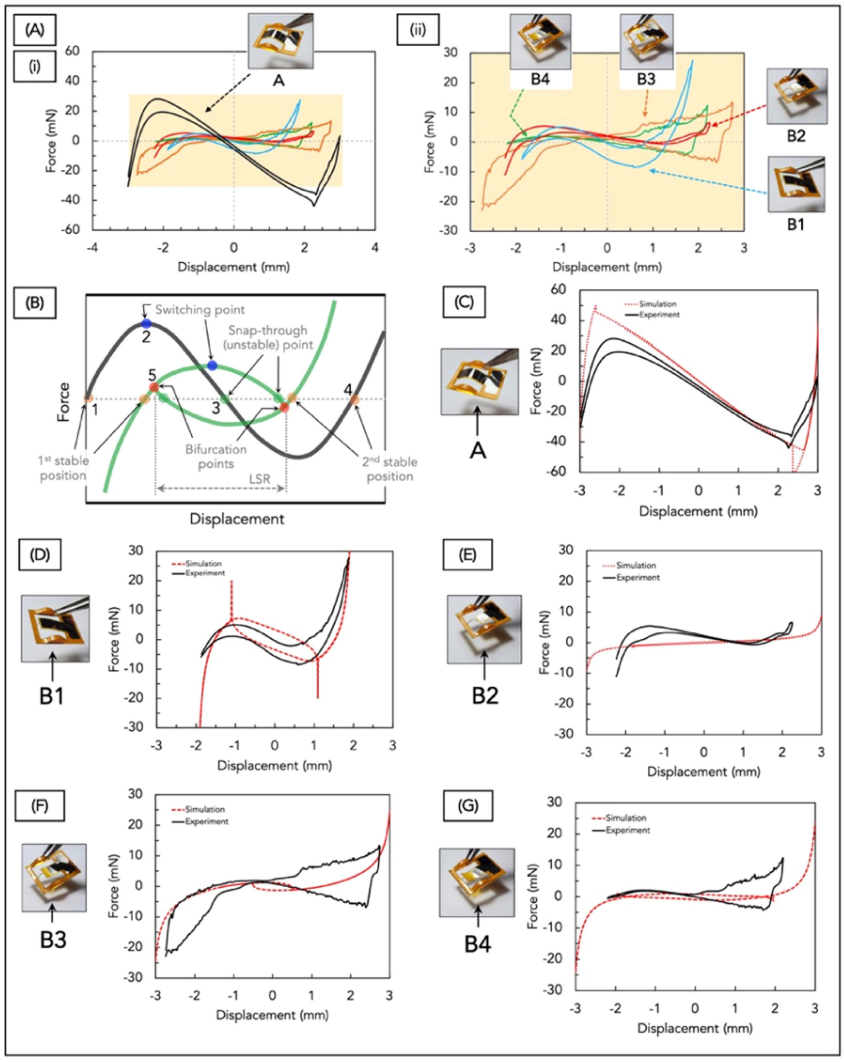

Figure 4.8: (A) (i, ii) Force-deflection curves of the different selected devices: the reduction of stiffness can be clearly observed from the design A to the other designs. (B) Example of a force-deflection curve for design A (black) and a statically-balanced design B (green), with indication of the first stable position (1), the switching points (2), the snap-through points (3), the second stable position (4), the bifurcation points (5) and the low-stiffness region (LSR) of a generic snapping structure. (C-G) Force-deflection curves for each single tested design, compared with the simulated curves.

INFLUENCE OF BUCKLING ONTO THE OUTPUT GENERATION

Preliminary performances of the fabricated PIP devices have been conducted by triggering the snapping state of the unstable structures, and detecting the output open-circuit voltage by means of an oscilloscope. Figure 4.9(A) depicts the forward and backward snapping of a PIP device, whereas Figure 4.9(B) reports the signals of the PIP devices with different designs. The comparison between the fixed device with only thermal stresses and the devices with package-induced instability reveals an enhancement of the generated voltage owing to the fast snapping and buckling effect. The device with design A exhibits a lower voltage in comparison to the other PIP designs because of two concur-rent factors. First, the higher stiffness of the unstable structure makes it less flexible and less prone to undergo fast snapping, thus reducing the acceleration of the element and consequently the output generation. Secondly, since the piezoelectric region is symmetric with respect to the application point of the mechanical triggering probe (in the middle), the snapping oscillation induces a symmetric stress distribution and thus charges with opposite signs (see also Figure 4.2(B)). This partial charge cancellation effect reduces the amplitude of the output signals.

The presence of the Kapton stripe and the asymmetric design of the PIP devices yield an open-circuit voltage 6 to 8 times higher than the one produced by thermal stresses (~ 45 mV peak-to-peak), demonstrating the enhancement effect of the packaging. In particular, design B4 exhibits an 8-fold-enhanced peak-to-peak voltage of ~ 350 mV due to the triggered snapping. Noteworthy, the eight-fold enhancement in the output voltage corresponds to a ~ 64-fold enhancement in the output power with respect to the standard, thermally-stressed device (1.225 μW vs 20.25 nW in a single snapping step, with a 100 kΩ impedance). This demonstrates that by only modifying some specific features of the design it is possible to enhance power by a factor 64.

The detected signals can be analyzed from a viewpoint of the working mechanism of the fabricated PIP devices, which is illustrated in Figure 4.9(C) for a full snapping cycle. Initially, the device is in an undeformed state, thus there is no potential difference inside the piezoelectric material. Under an applied mechanical stress, caused by a manual tapping or an airflow, the thin film starts to deform generating a piezoelectric potential along the direction of the material polarization, i.e. perpen-dicularly to the Kapton substrate (Figure 4.9(C), panel 3). Thus, a positive potential is generated when the applied stress is compressive, increasing from the substrate to the upper surface (where the top electrode is), and reaching the maximum value at the maximum strain (panel 4). When pressing in the opposite direction, the potential follows the same pathway but with opposite sign (panel 1) ending with another snapping step (panel 2). Due to the very fast transition between two equilibrium positions, rapid deformations and high voltages are achieved [154, 155]. As a result, the output is much greater than what is achieved in a standard piezoelectric transducer [113].

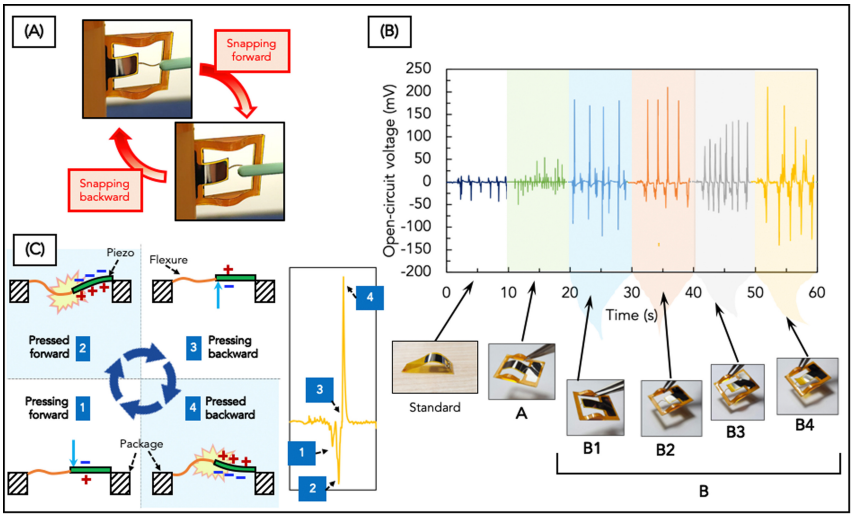

Figure 4.9: (A) Snapping forward and backward of a PIP device. (B) Open-circuit voltage of the PIP devices (designs A and B) compared to a standard structure (only subjected to thermal stresses). (C) Working principle of the piezoelectric active element during the snapping cycle with correspondence to the detected signal: (1) pressing forward, (2) pressed forward, (3) pressing backward, (4) pressed backward.

WIND ENERGY HARVESTING PERFORMANCE

In Figure 4.10(A) the results of the wind energy harvesting experiment are reported; the wind speeds used for the tests, and the open-circuit voltage of the tested designs are reported in (i) and (ii-vi), respectively. The output voltage generally increases with increasing wind speed because a higher displacement is imparted to the movement of the piezoelectric active area by a faster airflow. However, it can be seen that even at the greatest wind speeds, device A is not flexible enough to allow for the snapping motion to occur, and thus produces no relevant power output. In contrary, and as a result of the increased flexibility, the variations of design B demonstrate open-circuit voltages in the range of 200-450 mV.

The open-circuit voltage signals of designs B2, B3 and B4 are re-ported in Figure 4.10(A)(iv–vi), respectively. At a wind speed of 20 $m\,s^{-1}$, the devices produce a peak-to-peak voltage of ~ 0.45 V for B4, ~ 0.24 V for B2 and ~ 0.29 V for B3. Therefore, at high speeds the design exhibiting the best performances is B4, allegedly owing to a better interaction between the shortest Kapton flexure and the airflow, which triggers a faster and more impulsive snapping. At lower wind speeds, i.e. 2.5 $m\,s^{-1}$, the behavior of the three designs is different, in fact the peak-to-peak voltages are ~ 30 mV for B4, ~ 25 mV for B2 and ~ 120 mV for B3. Therefore, B3 with an intermediate length of the Kapton stripe exhibits the best performance for lower speeds.

The design with longer piezoelectric area (design B1) produces a reduced signal, as reported in Figure 4.10(A)(iii), reaching an average peak-to-peak

voltage of ~ 75 mV at 20 ms^{-1}, and ~ 19 mV at 2.5 ms^{-1}. The lower voltage is owing to the partial charge cancellation occurring during the oscillation of the long piezoelectric cantilever, which undergoes de-formations with opposite curvature during the same movement, i.e. with mechanical stress and thus electrical charges with opposite sign. This demonstrates that a larger area of piezoelectric material is less convenient for a wind energy harvester and, in particular, for the fabrication of a PIP device: the buckling effect resulting from package-induced instability should be imposed not on a full piezoelectric element, but on a substrate on which a smaller piezoelectric element resides. The previous results are also confirmed by the power density curves given in Figures 4.10(B)(i–iv). After measuring the average peak-to-peak voltage drop on the resistive loads connected to the device, the generated power density can be determined according to the following expression.

$$\tilde{P} = \frac{(\triangle V)^2 / R}{S} \tag{4.5}$$

Where $\tilde{P}$ is the output power density; S is the active piezoelectric area; R,$\triangle V$ are the resistance and the average peak-to-peak voltage drop on the resistive load, respectively. When the device is connected to an optimal load matching its electrical impedance [149], the maximum power is reached and the curve exhibits a peak. Figure 4.10(B) reports the power curves for the highest and the lowest wind speeds, i.e. 20 ms^{-1} and 2.5 ms^{-1}. The curves for design A are not reported because no relevant power was observed. For all the designs the maximum power is achieved at an optimal load of ~ 102 kΩ. The power density peak at 20 ms^{-1} is ~ 11.3 mWm^{-2} for B4, ~ 4 mWm^{-2} for B2, ~ 2.25 mWm^{-2} for B3 and ~ 0.35 mWm^{-2} for B1. At 2.5 ms^{-1}, instead, the power peak is achieved at ~ 0.085 mWm^{-2} for B4, ~ 0.037 mWm^{-2} for B2, ~ 0.30 mWm^{-2} for B3 and ~ 0.01 mWm^{-2} for B1. This confirms that (i) design B1 achieves the lowest performances due to partial charge cancellation during motion, (ii) is the best design for higher speeds is B4, and (iii) is the best design for lower speeds is B3.

The energy harvesting efficiency is strictly correlated to the output power, in fact for a piezoelectric transducer excited by a fluid flow it can be determined as the fraction of the wind kinetic energy flux through the cross-section occupied by the harvesting device actually transferred to the output circuit. Therefore, for a single oscillation it can be expressed as follows [156].

$$\eta = \frac{\bar{P}}{\frac{1}{2}\rho v^3 (2\bar{A}W)} \tag{4.6}$$

where $\bar{P}$ is the output power peak of the device; ρ, v are the density and velocity of airflow; W is the width of the active piezoelectric region; $\bar{A}$ is the motion amplitude of the active piezoelectric element, thus $2\bar{A}$ the range of motion, which results in 6 mm for design A and ~ 3 mm for the other designs

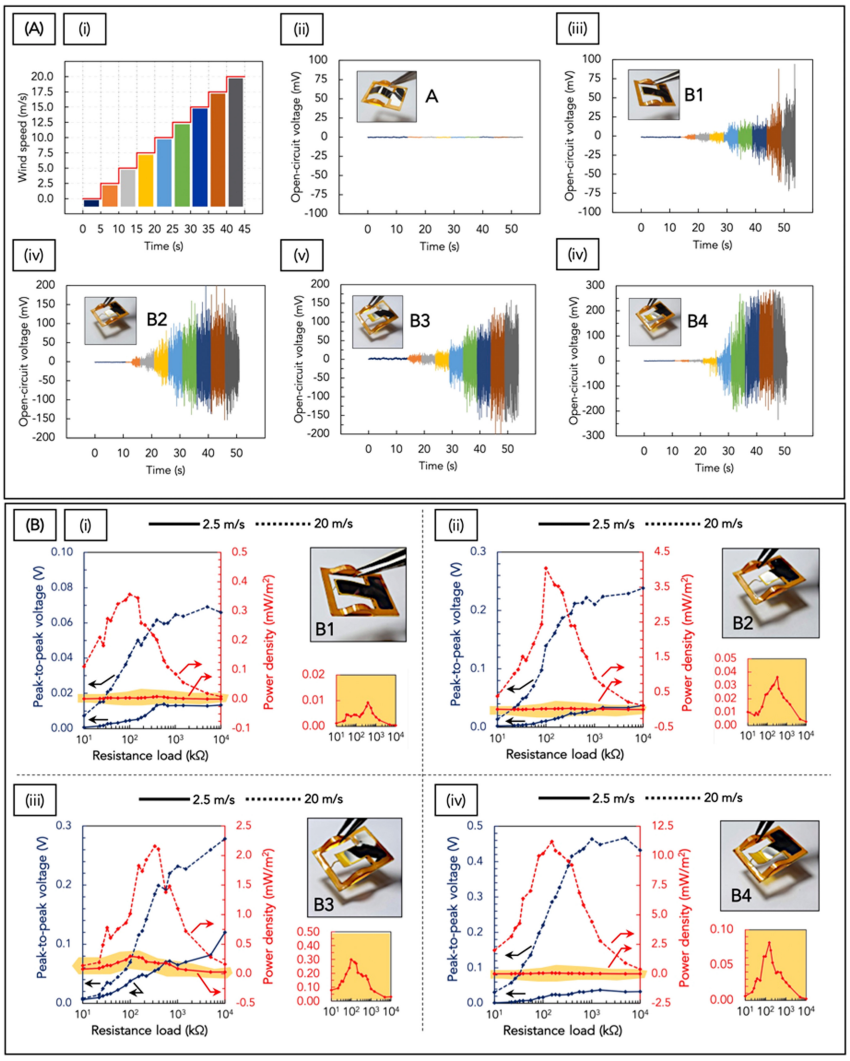

Figure 4.10: (A) Open-circuit voltage of the tested designs in the wind tunnel, under a wind speed ramp between 0 and 20 m/s with a step of 2.5 m/s for 5 s (i). Design A (ii), B1 (iii), B2 (iv), B3 (v), B4 (vi). (B) Power density curves and peak-to-peak voltage curves of the tested designs at two selected wind speeds: design B1 (i), B2 (ii), B3 (iii), B4 (iv). The solid lines correspond to a low wind speed (2.5 m/s), whereas the dotted lines correspond to a high wind speed (20 $\mathrm{m\,s^{-1}}$).

B1-B4. Hence, the designs B1-B4 can be compared with design A in terms of energy harvesting efficiency η and thus the specific influence of static balancing design onto this parameter can be evaluated. The range of values of the efficiency are below the ones of similar, recently-developed wind energy macro-harvesters, based on other piezoelectric/triboelectric materials or different architectures [157–160]. This is ascribed to the very

small device's dimensions under consider-ation in this work, resulting in relatively low power levels. In addition, Equation (4.6) holds for the assumption of a device in a regular flow, not ac-counting for the whole bluff-body/device system: the calculated efficiency represents a lower limit and specific experimental studies would be required to quantify the contribution of turbulences induced by the bluff body. However, the PIP devices can be rather considered a valid alternative in the context of unstable and nonlinear MEMS energy micro-harvesters, where research efforts are still ongoing [129, 161]. In fact, the key aspect on which this work focuses is the relative increase of energy harvesting efficiency induced by the mere application of static balancing principles, as summarized in Table 4.3. While the design A has a zero efficiency, the other designs B1-B4 are characterized by an increase in efficiency, which is maximized by design B3 at low speeds (4.610^{-3}%) and by design B4 at high speeds (5.2410^{-4}%). Additionally, it is noteworthy that the efficiency values are generally lower for high speeds while they increase by a factor 10 at low speeds for the same device. This demonstrates the suitability of the proposed method for designing and fabricating innovative future energy harvesters to be adopted especially for weak airflows, where standard technologies or current microfabricated devices cannot work effectively.

A further analysis has been performed to determine the characteristics of the wind-device interaction for lower wind speeds (design B3) and for higher wind speeds (design B4). In particular, a finer ramp of wind speeds has been set for the design B3, within the range of 0 to 5 $\mathrm{m\,s^{-1}}$, with a step of 0.1 $\mathrm{m\,s^{-1}}$ for a time interval of 1 s. As reported in Figure 4.11(A), the open-circuit voltage generated by the device B3 increases progressively with increasing wind speeds, exhibiting a low-range cut-in speed of ~ 0.3 $\mathrm{m\,s^{-1}}$, a low-range threshold speed of ~ 2.5m/s and a low-range rated speed of ~ 4.5 $\mathrm{m\,s^{-1}}$.

The design B4, selected for higher ranges of wind speed, exhibits a threshold speed of 2.5 $\mathrm{m\,s^{-1}}$ and a rated speed of ~ 17.5 $\mathrm{m\,s^{-1}}$ (Figure 4.11(B)).

Table 4.3: Comparison of output power and energy harvesting efficiency for a single oscillation of the selected designs.

Wind speed (v)		2.5 $\mathrm{m\,s^{-1}}$			20 $\mathrm{m\,s^{-1}}$		
Design	$2\bar{A}W$	p	$\bar{P}$	η	p	$\bar{P}$	η
	($\mathrm{mm^2}$)	($\mathrm{mW\,m^{-2}}$)	(nW)	(%)	($\mathrm{mW\,m^{-2}}$)	(nW)	(%)
A	42	n	n	0	n	n	0
B1	21	0.01	0.21	$4\ 10^{-4}$	0.35	0.02	$0.19\ 10^{-4}$
B2	21	0.037	1.13	$5.6\ 10^{-4}$	4	0.19	$1.88\ 10^{-4}$
B3	21	0.3	9.24	$4.6\ 10^{-3}$	2.25	0.11	$1.01\ 10^{-4}$
B4	21	0.085	3.92	$2.0\ 10^{-3}$	11.3	0.54	$5.24\ 10^{-4}$

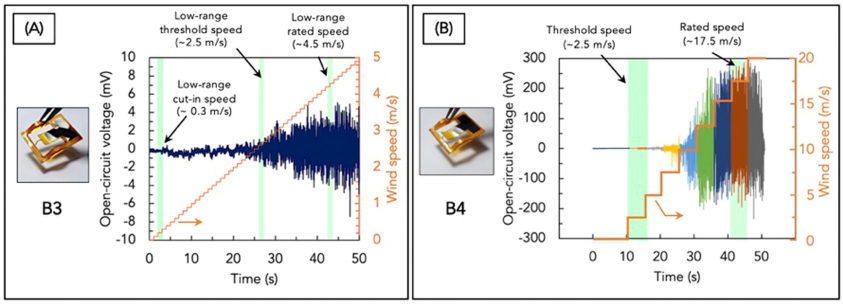

Figure 4.11: (A) Fine wind speed ramp for the determination of low-range cut-in, threshold and rated speeds for the design B3. (B) Coarse wind speed ramp for the determination of threshold and rated speeds for the design B4.

The results demonstrate that slight differences in the design of the PIP device can critically influence its performance. The length of the flexure and the consequent Kapton collector area without the piezoelectric material, are crucial both for imparting the mechanical flexibility of the device and for enhancing the output generation performances in different wind speed ranges. The present work is focused on the preliminary investigation of different designs rather than an optimization of the system for the application of wind energy harvesting. The results shown are useful to provide the following recommendations about the design of buckled devices for mechanical energy harvesting. First of all, the combination of a design aimed at static balancing and the PIP method are a feasible way to increase the flexibility of piezoelectric transducers. Secondly, the presence of the collector in the design can be used to achieve an increased performance: its intermediate flexibility between the flexure and the piezoelectric region provides a more stable oscillation between the stable positions. Finally, it should be noted that the bending-curve of the piezoelectric region is very important for the performance of the device, and may change when the design parameters are manipulated, especially the length of the flexure. When the proposed design is to be optimized for a particular application by tuning for example the flexure length or the length of the collector area, the effect on this curve must also be considered to avoid loss of performance. In general, it is recommended to achieve the desired range of motion and a very low force at switching point in order to design ultra-compliant energy harvesters.

For a first evaluation of the durability of the PIP devices, they have been tested in the wind tunnel for a prolonged time interval (10 min) and also after 30 min of continuous flow at a fixed wind speed. In this way, the mechanisms are subjected to the same periodic oscillations and deformations, after a first transient interval. In particular, the mechanisms that exhibited the best results for power densities, i.e. B3 and B4, have been tested at 2.5 $\mathrm{m\,s^{-1}}$ and 20 $\mathrm{m\,s^{-1}}$, respectively. It was observed that stable and

reproducible open-circuit voltage signals have been obtained with non-reduced amplitude, which demonstrates the durability of the thin-film materials and also the reliability of the PIP devices.

4.4 CONCLUSION

In this work a new method of inducing out-of-plane buckling in flexible piezoelectric transducers is reported. The method, which is based on the packaging design, is called Package-Induced Preloading (PIP). The theoretical basics of this concept are presented and exploited to develop flexible and lightweight prototypes for low-frequency energy harvesting. The transducers are based on piezoelectric prestressed thin films of Aluminium Nitride deposited by MEMS technologies onto a Kapton substrate. The design aimed at static balancing is used to achieve a greatly increased mechanical flexibility. The mechanisms are shaped by laser cutting, and the piezoelectric active area is patterned through lithography. The package extending out-of-plane is fabricated by high- resolution 3D printing.

By mechanically triggering the snapping state on the device, enhanced output voltages are demonstrated in comparison with prior art. A preliminary investigation is reported regarding the influence of the transducers' design onto the output generation performances under incoming wind flows in a wind tunnel. Different designs have been tested and two of them are demonstrated to obtain the best power densities for lower and higher ranges of wind speeds. It was demonstrated that the combination of a design aimed at static balancing and the PIP method is a feasible way to increase the flexibility of piezoelectric transducers. The proposed approach is versatile and can be applied to several types of devices, based also on different materials or structures. It can be harnessed to generate power from unfavorable conditions and to have a greater control on the movements of the piezoelectric structures. The presence of the ~ 3 mm-thick package as functional mechanical support permits to employ the device in several ways, in confined volumes and spaces or attached onto whichever surface. In addition, the fabricated prototypes were shown to be able to successfully capture energy from an incoming wind flow. Through further optimization, the efficiency of this device can be improved and novel ultra-compliant mechanisms can be designed for applications in energy harvesting from low-frequency mechanical sources, such as wind or water flows and human body motions.

5 DESIGN OF A STATICALLY BALANCED ORTHO-PLANAR MECHANISM

The usually high eigenfrequencies of miniaturized oscillators can be significantly lowered by reducing the stiffness through stiffness compensation. In this work, a mechanical design for a compliant ortho-planar mechanism is proposed in which the stiffness is compensated to such a degree that it can be identified as statically balanced. The mechanism was fabricated using laser micro-machining and subsequently preloaded through packaging. The statically balanced property of the mechanism was experimentally validated by a measurement of the force-deflection relation. A piezoelectric version of the design was fabricated for the purpose of energy harvesting from low-frequency motion. For a sub 1 Hz *excitation, the device demonstrated an average power output of 21.7* μW *and an efficiency that compares favorably to piezoelectric energy harvesters reported in literature. Therefore, it was found that stiffness compensation is a promising method for the design of piezoelectric energy harvesters for low-frequency motions.*

5.1 INTRODUCTION

In the last decades, vibration energy harvesting research has led to the development of increasingly smaller devices that scavenge energy from ambient vibration sources, such as human motion. As one of the most promising transduction mechanisms for energy harvesting, the piezoelectric effect has attracted great interest when combined with compliant mechanisms, a field in which mechanisms are synthesized from deforming members. A disadvantage of the desired miniaturization in this context is that the mass scales down at an increased rate compared to the stiffness which leads to higher natural frequencies. Especially for energy harvesting applications, in which the frequencies of ambient motions are generally low, this can greatly reduce the performance [26]. In order to overcome this problem, a negative stiffness element can be employed as a balancer that

This chapter originally appeared as T.W.A. Blad, R.A.J. van Ostayen, J.L. Herder, N. Tolou, (In-press) *A Statically Balanced Compliant Ortho-Planar Mechanism for Low-Frequency Energy Harvesting* in the Journal of Mechanical Design (2021) [162].

counteracts the (positive) stiffness of the mechanism. As a result, statically balanced mechanisms can be obtained that demonstrate near-zero stiffness behavior over a part of their working range [37]. These mechanisms are identified as stiffness-compensated or statically balanced mechanisms.

This was demonstrated by [95], where a statically balanced compliant mechanism (SB-CM) was developed and studied. This mechanism was fabricated using deep reactive-ion etching and achieved a near zero stiffness characteristic over a small range of motion. In [49] anther SB-CM was demonstrated in which the preloading was induced by a MEMS compatible thin film process. The resulting mechanism combined the positive stiffness of a linear guidance mechanism with a post-buckled flexure to achieve static balancing. An oscillator application was shown by [94] where a MEMS gravimeter is demonstrated that features a proof mass on top of an anti-spring mechanism. With increasing displacement, the anti-spring softened and the system was able to reach a resonant frequency of 2.3 Hz in the vertical orientation. Although low-frequency and bi-stable systems have been shown for piezoelectric energy harvesting [77, 163], the application of SB-CMs to compensate the stiffness of a piezoelectric transducer has not been demonstrated yet. One explanation may be found in the mismatch between the degrees of freedom (DoFs) of most SB-CMs, that move in-plane, and the most widely used piezoelectric transducers for energy harvesting, which are cantilevers that move out-of-plane.

The research objective of this work is to develop a statically balanced compliant ortho-planar mechanism (SB-COM) in which a piezoelectric transducer can be integrated for low-frequency vibration energy harvesting. Moreover, due to its planar design such a mechanism is compatible with the planar microfabrication processes and therefore allows for miniaturization to micro-scale.

In Section 5.2 the mechanical design and method for tuning the stiffness of mechanisms are introduced. Furthermore, the fabrication of the prototypes and experimental methods are discussed. The results are shown and discussed in Section 5.3, and the conclusions are listed in Section 5.4.

5.2 METHODS

MECHANICAL DESIGN

Figures 5.1(A,B) show a schematic view of the proposed design of the SB-COM. The design consists of a cantilevered beam, with a length L_c and rigidity EI_c which is connected to a rigid and square shuttle with dimensions of L_m. Two flexures with lengths L_f and rigidities EI_f, are connected to the shuttle at right angles to the cantilever. The initially flat flexures can be buckled by compressing them over a distance of dL. This process is called preloading and results in the flexures assuming a post-buckled shape that extends out of plane. In this preloaded configuration, the restoring force

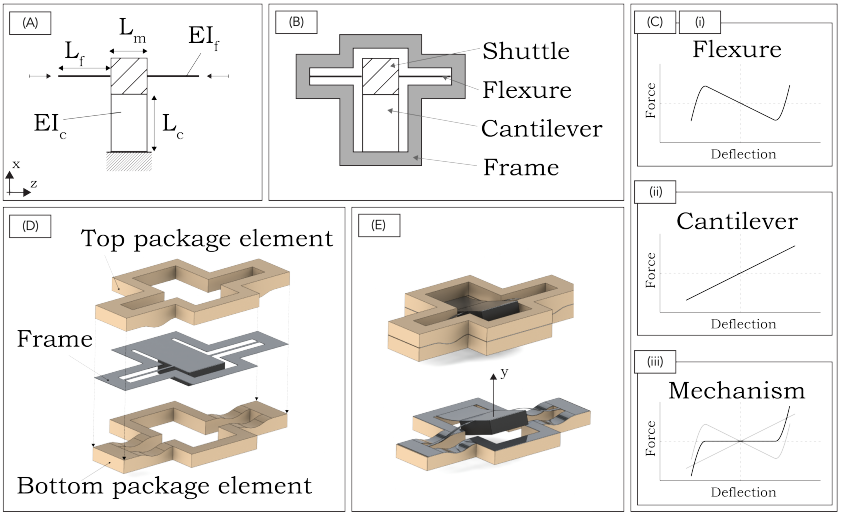

Figure 5.1: Design of the proposed SB-COM; (A) schematic showing the design parameters; (B) schematic overview of the components; (C) force-deflection relations of the (i) preloaded flexures, (ii) cantilever and (iii) statically balanced mechanism; (D) demonstration of the PIP method; (E) the assembled structure with and without the top package element.

delivered by the flexures on the shuttle in the out-of-plane direction is shown in Figure 5.1(C)(i). This force-deflection relation has a negative slope (i.e. stiffness) that is approximately constant over a part of the range of motion [29]. The flexures can be designed using the method outlined in the next section, such that this slope is equal and opposite to the restoring force provided by the cantilever (Figure 5.1(C)(ii)). As a result, a statically balanced system can be obtained in which the shuttle is in a state of neutral equilibrium over a part of its range of motion (Figure 5.1(C)(iii)).

The method used for preloading the flexures is demonstrated in Figures 5.1(C,D). In this method, a frame is designed around the mechanism which is sandwiched between two package elements with opposite out-of-plane geometries. As a result, the frame is forced to follow the out-of-plane shape of the packaging elements and therefore shortening it in the in-plane direction to achieve the desired preloading. This method is called package induced preloading (PIP) and is based on the technique proposed in [100].

STIFFNESS DESIGN METHOD

To tune the negative slope of the force-deflection relation of the preloaded flexures, the length, L_f, and the flexural rigidity, EI_f, can be manipulated. Compared to the length, tuning the rigidity does not affect the kinematics of the mechanism and is therefore preferred. The rigidity is most conveniently manipulated through the design of the width of the flexures, w_f, as this relation is linear compared to the cubic dependency on the thickness.

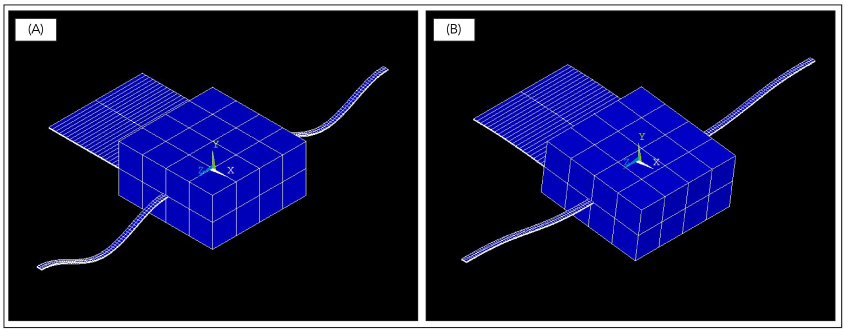

Figure 5.2: Finite element model representation of the buckling modes that contribute to the out-of-plane displacement of the shuttle; the modes are identified as (A) mode "W" and (B) mode "V".

Moreover, the width is easily controllable with planar manufacturing processes such as laser cutting. Therefore, w_f is chosen as the design parameter to tune the stiffness of the preloaded flexures.

In order to determine the configuration for which the desired effect is achieved, a linear buckling analysis is carried out using the finite element model (FEM) to identify the buckling modes of the mechanism. From this analysis, the two buckling modes shown in Figure 5.3 are found and identified as the modes "W" and "V". The out-of-plane motion of the shuttle can be described as a combination of these modes such that the mechanism moves from mode "W" to mode "V" when the shuttle is displaced away from $y = 0$. It was found that a post-buckled beam can be statically balanced over a particular motion if the critical loads corresponding to the buckling modes that describe this motion are equalized [89]. This principle can also be applied to this mechanism, such that static balancing of the shuttle in the out-of-plane direction is achieved if the critical loads corresponding to the "W" and "V" modes are equal.

Finding an optimized value for w_f is done as follows. First, the analytical model is evaluated for a range of values for w_f to find the critical loads of the mechanism. These critical loads depend differently on w_f and values can be found for w_f for which two critical loads are equal. Next, the FEM is used to identify the mode shapes corresponding to these critical loads and fine-tune the value for w_f for which the critical loads of modes "W" and "V" are equal. Finally, the nonlinear force-deflection relation of the post-buckled mechanism is simulated to verify that the resulting configuration is indeed statically balanced.

ANALYTICAL MODEL

For a beam element with a rigidity, EI, the transverse displacement, y, as a function of the axial coordinate, z corresponding to an applied axial load, P, is governed by the following differential equation [96].

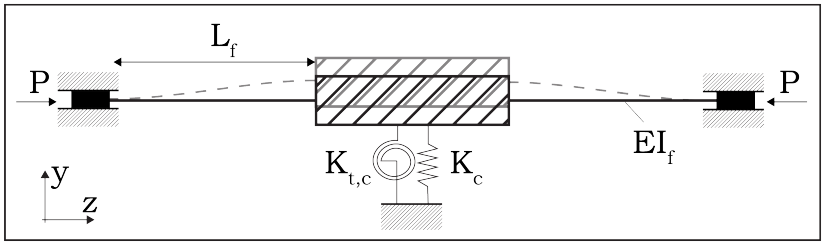

Figure 5.3: Schematic of the buckling problem formulated for the SB-COM.

$$\frac{\mathrm{d}^4 y}{\mathrm{d}z^4} + \frac{P}{EI}\frac{\mathrm{d}^2 y}{\mathrm{d}z^2} = 0 \tag{5.1}$$

The buckling problem of the SB-COM can be formulated as shown in Figure 5.2 where the flexures are modeled as two beam elements connecting to a rigid shuttle. Along the length of the flexures the following points can be identified as the edges of the beam elements: $z_0 = 0$, $z_1 = L_f$, $z_2 = L_f + L_m$, and $z_3 = 2L_f + L_m$. The transverse displacement is therefore given by the following expression.

$$y(z) = u_i(z), z_{2i-2} \leq z \leq \text{for} i = 1,2 \tag{5.2}$$

Where u_i is the transverse displacement of the i^{th} flexure. The general solution to Equation (5.1) can therefore be found as a piecewise equation with the following form.

$$u_i(z) = A_i \sin(\frac{\Lambda}{\sqrt{EI_f}}z) + B_i \cos(\frac{\Lambda}{\sqrt{EI_f}}z) + C_i z + D_i \tag{5.3}$$

Where A_i,B_i,C_i and D_i are unknown constants that depend on the boundary conditions of the beams and Λ are the eigenvalues corresponding to the critical loads of mechanism such that $\Lambda^2 = P_{crit}$. The boundary conditions that are considered for this mechanism are given by the following equations.

$$y(z_0) = 0 \tag{5.4}$$
$$y(z_3) = 0 \tag{5.5}$$
$$\frac{\mathrm{d}y}{\mathrm{d}z}(z_0) = 0 \tag{5.6}$$
$$\frac{\mathrm{d}y}{\mathrm{d}z}(z_3) = 0 \tag{5.7}$$
$$y(z_1) = y(z_2) + L_m \frac{\mathrm{d}y}{\mathrm{d}z}(z_1) \tag{5.8}$$
$$\frac{\mathrm{d}y}{\mathrm{d}z}(z_1) = \frac{\mathrm{d}y}{\mathrm{d}z}(z_2) \tag{5.9}$$
$$\frac{\mathrm{d}^2 y}{\mathrm{d}z^2}(z_1) + K_{t,c}\frac{\mathrm{d}y}{\mathrm{d}z} = \frac{\mathrm{d}^2 y}{\mathrm{d}z^2}(z_2) \tag{5.10}$$
$$\frac{\mathrm{d}^3 y}{\mathrm{d}z^3}(z_1) - K_c y = \frac{\mathrm{d}^3 y}{\mathrm{d}z^3}(z_2) \tag{5.11}$$

At the outer edges, the beams are fixed in transverse translation and rotation resulting in the boundary conditions as provided by Equations (5.4)-(5.7). At the middle connections to the shuttle, continuity is enforced through the boundary conditions given by Equations (5.8) and (5.9). Because the shuttle is assumed rigid, the rotations at the points where flexures connect to the shuttle (i.e. z_1 and z_2) must be equal and the transverse displacements at these points can only be offset as a result of the rotation of the shuttle. Finally, Equations (5.10) and (5.11) enforce equilibrium in the bending moments and lateral forces. In these equations, terms are included to cover the force and moment exerted by the cantilever as a result of its translational stiffness in the y-direction, K_c, and its torsional stiffness around the x-axis, $K_{t,c}$. These stiffnesses can be found from the following equations where GJ_c is the torsional rigidity of the cantilever.

$$K_c = \frac{3EI_c}{(L_c + \frac{L_m}{2})^3 - \frac{L_m}{2}^3} \qquad (5.12) \qquad\qquad K_{t,c} = \frac{GJ_c}{L_c} \qquad (5.13)$$

By applying the boundary conditions given by Equations (5.4)-(5.11) to Equation (5.3) we can find a transcendental eigenvalue problem of the following form [97].

$$\mathbf{T}(\Lambda)\mathbf{z} = \mathbf{0} \qquad (5.14)$$

Where $\mathbf{T}$ is a matrix consisting of transcendental functions in Λ , and $\mathbf{z}$ is a constant eigenvector containing A_i,B_i,C_i,D_i. The critical loads of the beam are found from the non-trivial solutions of Λ for $\mathbf{z} \neq \mathbf{0}$, and the mode shapes can be found by substituting the result in Equation (5.3).

FINITE ELEMENT MODEL

To validate the critical loads found in the analytical model and simulate the force-deflection relation of the mechanisms FEM was built in ANSYS Mechanical APDL using beam elements (beam188). A linear elastic material model with the properties of spring steel (E = 190 GPa, ν = 0.34, ρ = 7.82 $\mathrm{g\,cm^{-3}}$) is used. The buckling modes and their corresponding critical loads are computed by a linear buckling analysis. This analysis is done through eigenvalue buckling in a static structural analysis in which forces were applied to the outer edges of the flexures as shown in Figure 5.3. The results from this analysis are used to iteratively fine-tune the optimized value of w_f that was found with the analytical model. The simulation of the force-deflection relation of the post-buckled mechanism was carried out in two steps. First, a preloading step was applied in which the outer edges are displaced inwards by a preload displacement dL. Small imperfections were incorporated in the flexures to prevent the simulation to crashing during this step as a result of singularities. After the buckled shape was achieved, the post-buckled mechanism was manipulated in the out-of-plane direction. The reaction forces were captured over the range of motion at regular

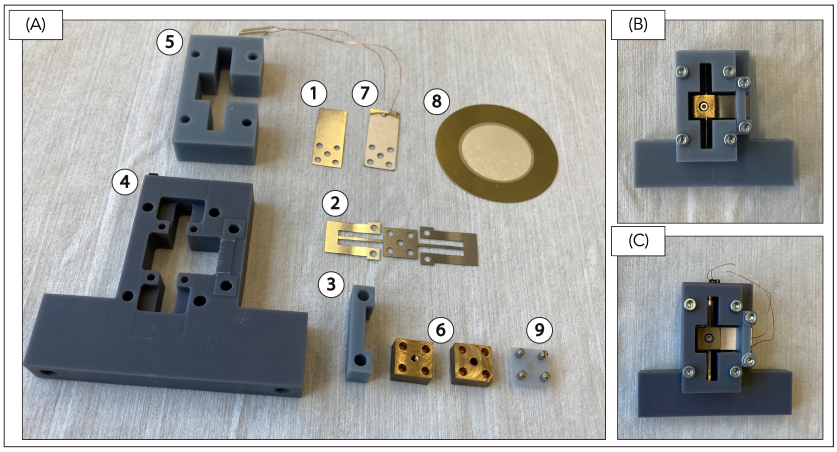

Figure 5.4: (i) Overview of components and (ii) assembled prototypes of the (A) SB-COM and (B) SCOPE.

Table 5.1: Relevant parameters of the fabricated prototypes

Parameter	Symbol	Value
SB-COM & SCOPE		
Cantilever length (mm)	L_c	7.5
Cantilever width (mm)	w_c	10
Shuttle length and width (mm)	L_m	10
Preload displacement (mm)	dL	0.2
Flexure length (mm)	L_f	13.5
Thickness of flexures (mm)	t	0.1
Mass of shuttle (g)	m	8
SB-COM		
Cantilever thickness (mm)	t_c	0.1
Flexure width (mm)	w_f	0.52
SCOPE		
Piezoelectric cantilever thickness (mm)	t_p	0.23
Flexure width (mm)	$w_{f,SCOPE}$	0.92

intervals to determine the force-deflection behavior.

FABRICATION AND ASSEMBLY

To validate the proposed SB-COM design, the components and prototypes shown in Figures 5.4(A-C) were fabricated. The cantilever (1) and flexures (2) are fabricated from 0.1 mm thick spring steel using a Spectra-Physics Talon 355-15 diode pumped solid-state (DPSS) UV laser system with a wavelength of 355 nm and maximum power of 15 W at 50 kHz. The cover of the cantilever (3) and the packaging elements (4,5) were 3d printed from UV photosensitive resin using a SLA machine (PRUSA SL1) and the shuttle (6) was machined from brass. The total mass of the shuttle was 8 g. The

elements were aligned by 2 x 5 mm dowel pins that were inserted in holes in the bottom package element (4) and the bottom half of the shuttle and lined up with holes in the flexure, cantilever, top package element (5) and the top half of the shuttle. The system was assembled by pushing the packaging elements together and clamping them with bolts resulting in the assembled SB-COM shown in Figure 5.4(B).

To evaluate the performance of the design for the application of energy harvesting from low-frequency vibrations, a piezoelectric version of the SB-COM shown in Figure 5.4(C) was fabricated. This prototype is identified as the SCOPE (i.e. Statically balanced Compliant Ortho-planar Piezoelectric Energy harvester). In the SCOPE, the stainless steel cantilever is replaced by a piezoelectric transducer (7) with an identical length and width as the cantilever. The transducer was fabricated from t_p = 0.23 mm thick audio buzzers (8) (KEPO FT-41T-1.0A1-478) using the laser. The buzzers consisted of a brass substrate with a thickness of 0.1 mm and a piezoelectric layer with a thickness of 0.13 mm to which electrical connections were soldered. To prevent short-circuiting the piezoelectric transducer, a 3d printed isolation layer (9) was added between the transducer and the top of the shuttle. In the SCOPE, the width of the flexures was increased to $w_{f,SCOPE}$ = 0.92 mm to compensate for the higher stiffness of the piezoelectric transducer. An overview of the important parameters of both prototypes is given in Table 5.1.

EXPERIMENTAL CHARACTERIZATION

The force-deflection relation of the SB-COM was evaluated experimentally with the setup shown in Figure 5.5(A)(i). The setup consists of a force sensor (1) (FUTEK LRM200) mounted on a motorized stage (2) (PI M-505) and connected to the prototype (3). The mechanism is actuated in a quasi-static fashion over a specified range of motion during which the reaction force is captured. The applied deflection is measured by capturing position data from the internal encoder of the stage. Data was recorded with a data acquisition system (4) (NI USB-6008) with a resolution of 50 μm. The connection between the force sensor and the prototype shown in Figure 5.5(A)(ii) is made by using a magnet that latches onto the bolt in the middle of the shuttle. This ensures that the force sensor remains in contact with the prototype such that also pulling forces can be measured.

The energy harvesting performance of the SCOPE was evaluated by using the setup shown in Figure 5.5(B)(i) to apply a prescribed motion to the package. The setup consists of a platform (5) suspended by air bearings that can be moved over a distance of 500 mm. The platform is driven by an ironless linear motor (TECNOTION UL-6N) controlled by a servo drive (KOLLMORGEN AKD-P00306). The position of the platform is measured using an incremental encoder (RENISHAW TONIC T1000-05A) and controlled using a position feedback loop. Moreover, the acceleration of the platform was also captured using an accelerometer (6) (ME-MEβSYSTEME

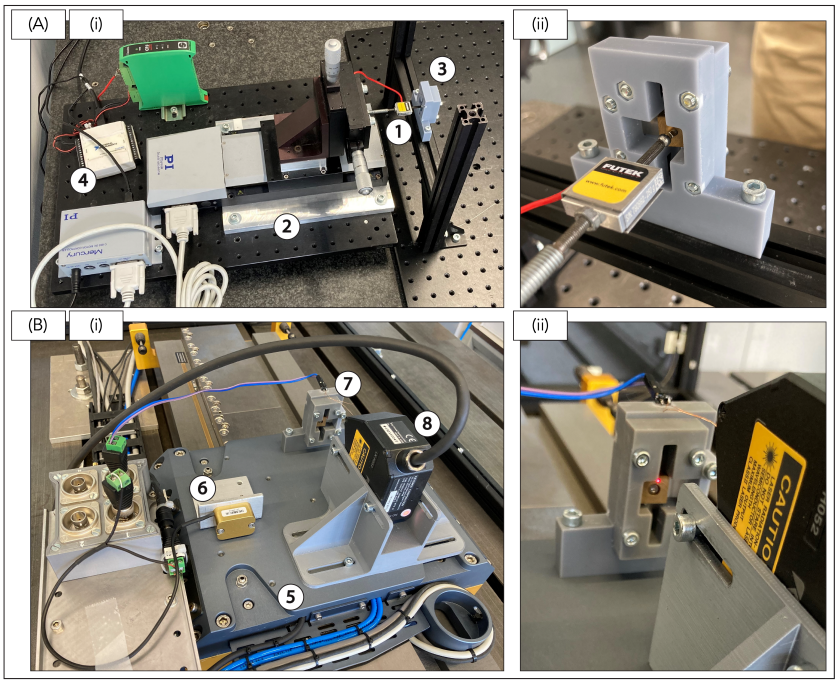

Figure 5.5: Experimental setups used for (A) the validation of the force-deflection relation of the SB-COM and (B) measuring the performance of the SCOPE under low-frequency vibration.

AS28E). The prototype (7) was fastened on top of the platform in an orientation such that the motion is applied in the y-direction and the and the displacement of the shuttle was captured using a laser sensor (8) (KEYENCE LS-K052) as shown in Figure 5.5(B)(ii). The power output of the piezoelectric transducer was measured over a 100 kΩ load.

5.3 Results and Discussion

Mechanical Analysis

The first three buckling modes of the SB-COM and their corresponding critical loads are shown in Figure 5.6. In this figure, the dashed lines are obtained with the analytical model and the solid lines are obtained with the linear buckling analysis carried out using the FEM. It can be found that next to the "W" and "V" modes also another mode is found that can be identified as the "N" mode. This mode describes a rotation of the shuttle is therefore not relevant for achieving a configuration in which the shuttle is statically balanced in the out-of-plane direction.

It can be observed that manipulating the design variable w_f has a different effect on the critical loads corresponding to these modes and that

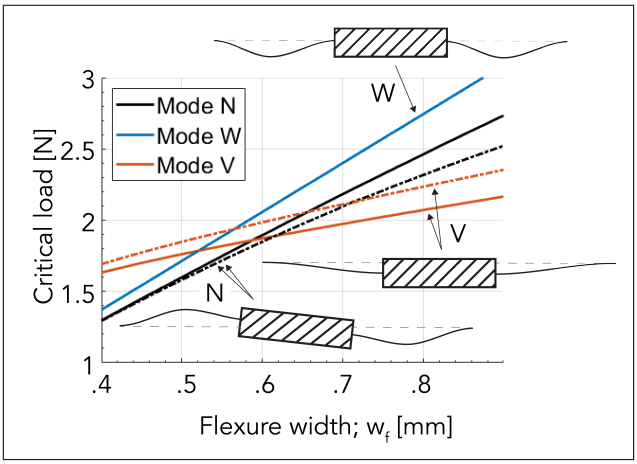

Figure 5.6: Buckling modes and corresponding critical loads as a function of the design variable w_f for the SB-COM; (dashed) analytical model, (solid) finite element model.

the order of the buckling mode changes over the considered region. The desired near-zero stiffness is achieved if the critical loads corresponding to the "W" and "V" modes are equalized because these modes describe the out-of-plane displacement. It can be found from the figure that this effect is achieved in the SB-COM at a flexure width of w_f = 0.52 mm. Following a similar analysis, this effect was found for the SCOPE at a flexure width of $w_{f,SCOPE}$ = 0.92 mm.

It can be seen that the analytical model provides a relatively good estimate of the critical loads calculated by the FEM. This is an important result as this analytical model can be evaluated much quicker. While the critical load of the "W" mode overlaps completely with the value calculated by the FEM, slight differences can be found in the values calculated for the "V" and "N" modes. These differences are most likely a result from the simplified representation of the displacement of the mechanism; in the analytical model, the displacement is assumed to be a translation in the out-of-plane direction, while in reality the proof mass will undergo a pivoting motion around the base of the cantilever.

FORCE-DEFLECTION RELATION OF THE SB-COM

The measured force-deflection relations of SB-COM with and without flexures are compared to the results of the simulations in Figures 5.7(A,B). From the results of the simulation shown in Figure 5.7(A) can be verified that without the flexures, the stiffness of the cantilever is 265 $\mathrm{N\,m^{-1}}$ and corresponds to the stiffness that can be calculated from Equation (5.12). Furthermore, it can be observed from the simulation shown in Figure 5.7(B)

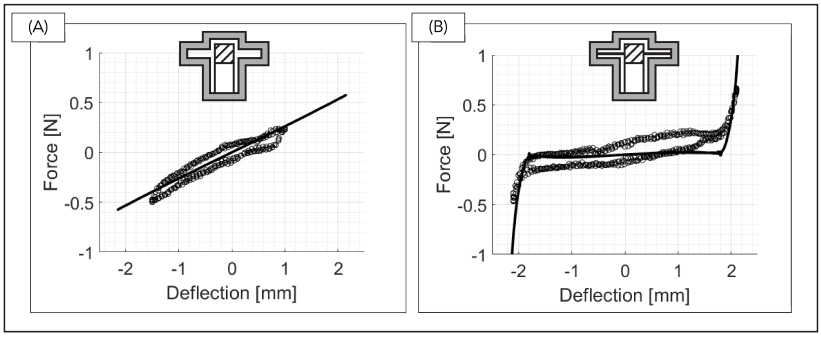

Figure 5.7: Measurement and simulation of the force-deflection relations of the SB-COM (A) without flexures and (B) with flexures; (—) FEM, (o) measurement.

that a much flatter force-deflection relation is found for the SB-COM when the flexures with width of $w_f = 0.52$ mm were added. In this configuration, the shuttle demonstrates a region of near-zero stiffness and virtually no force when deflected between approximately $y = -2$ mm and $y = 2$ mm . Therefore, this configuration can be identified as statically balanced. Moreover, It can be observed the force-deflection relation rapidly steepens for displacements of $|y| > 2$ mm. This steepening effect is a result of the flexures being straightened such that they lose their compensating effect and are loaded in tension instead. The measured force-deflection relations contain a hysteresis between the forward and backward load paths which is caused by the magnetic connection between the shuttle and the force sensor. Overall, they show a good correspondence to the simulated results. It can be seen that the greatest differences are observed in the near-zero stiffness region of the SB-COM with flexures $y = 0$ mm and $y = 2$ mm. These differences are mainly a result of manufacturing tolerances and the manual assembly that resulted in a slight preference of the mechanism to one of the sides.

ENERGY HARVESTING WITH SCOPE

The results of the low-frequency energy harvesting experiment of SCOPE with and without flexure are shown in Figures 5.8(A,B). In this experiment, the platform is moved with a harmonic motion with a frequency of 0.9 Hz and an amplitude of 230 mm such that an acceleration of 0.75 g is applied to the SCOPE. It can be seen from the figures that energy harvesting is demonstrated for this low-frequency excitation of sub 1 Hz.

From the figure can be seen that while the SCOPE without flexures demonstrates performance that is typical for linear oscillators at off-resonance conditions, the SCOPE with flexures was very lightly bi-stable and demonstrates a motion pattern where the shuttle rapidly moves through the low stiffness zone until it encounters an increase in the restoring force.

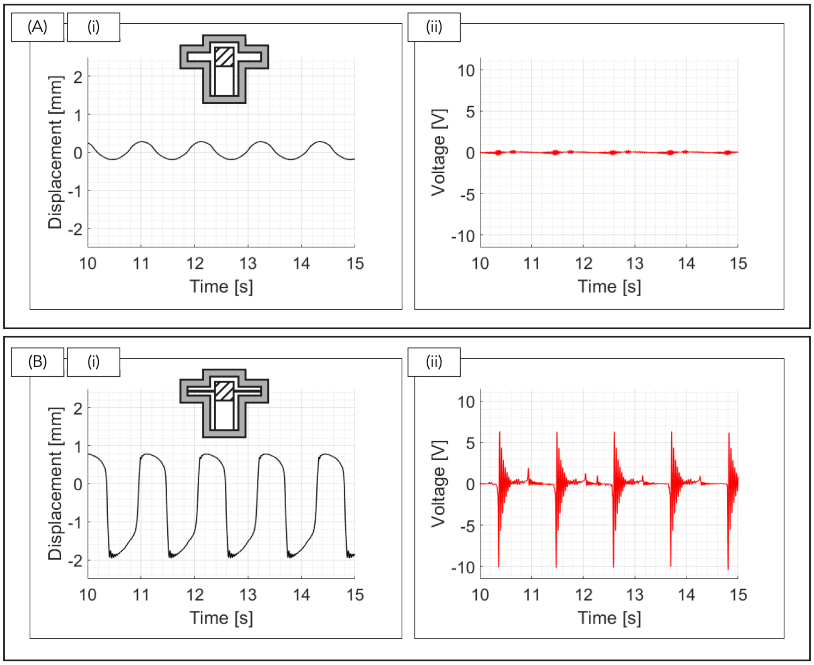

Figure 5.8: Measured (i) displacement and (ii) voltage over a 100 kΩ resistor when excited by a harmonic motion with a frequency of 0.9 Hz and an acceleration of 0.75 g for the SCOPE (A) without flexures and (B) with flexures.

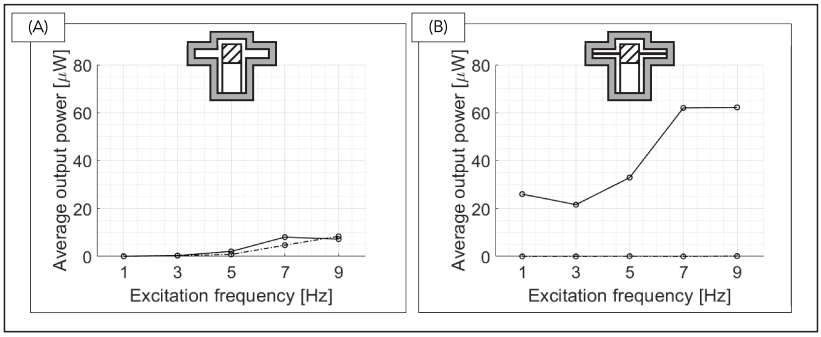

Figure 5.9: Frequency-power curves of the SCOPE (A) without flexures and (B) with flexures at accelerations of (dashed) 0.5 g, and (solid) 1 g.

The asymmetry in this motion pattern can likely be explained due to a slight preference of the mechanism resulting from the manufacturing tolerances and manual assembly. Moreover, at the displacement of $y = -2$ mm this leads to an impact-like behavior, presumably due to the rapid steepening of the force-deflection relation at this point, which greatly improves the power

output of the piezoelectric transducer. Moreover, the average power dissipated in the resistor over the 5 s interval shown in Figures 5.8(A,B) is 0.1 μW for the SCOPE without flexures, and 21.7 μW for the SCOPE with flexures.

The experiment is repeated for excitations of 1,3,5,7 and 9 Hz for accelerations of 0.5 and 1 g, and the resulting frequency-power curves are shown in Figure 5.9. From the figure can be observed that the SCOPE with flexures demonstrated a very high power output for accelerations of 1 g at all frequencies, but demonstrated virtually no power output for accelerations of 0.5 g. This result can be explained by the observed bi-stability of the SCOPE with flexures. Although the device was only very lightly bi-stable, the acceleration of 0.5 g was not sufficient to provide enough force to set the shuttle in motion.

EFFICIENCY OF THE SCOPE

To compare the performance of the SCOPE with piezoelectric energy harvesters reported in literature, the motion ratio, λ, and generator figure of merit, FoM_G, are used [58]. The motion ratio is a metric to describe the size of the generator relative to the applied excitation and the FoM_G is a metric with which a bias-free comparison can be drawn between generators of different shapes and sizes operated at different conditions. These quantities are defined by the following expressions.

$$\lambda = \frac{L_z}{2Y_0} \tag{5.15}$$

$$FoM_G = \frac{P_{avg}}{\frac{1}{16} Y_0 \rho_m V L_z \omega^3} \tag{5.16}$$

Where Y_0 and ω are the amplitude and frequency of the driving motion, V is the total volume occupied by the device, L_z is the dimension of the generator along the direction of the applied motion, ρ_m is the density of the proof mass material, and P_{avg} is the average output power dissipated in the resistive load. For the SCOPE with flexures, which has a dimension of $L_z = 15$ mm, a motion ratio of $\lambda = 0.033$ is found for the sub 1 Hz excitation with an amplitude of 230 mm. This constitutes to one of the lowest motion ratios reported in literature yet and demonstrates that this energy harvester is tested under conditions representative of a very high level of miniaturization [58]. Moreover, an efficiency of 0.27% was found at an average power output of 21.7 μW for the 50 x 32 x 15 mm device. This is a relevant efficiency for an energy harvester, especially considering that the device is tested at such a

Table 5.2: Performance of the SCOPE compared to energy harvesters reported in literature.

Source	Driving motion	Output power	Motion ratio	Efficiency
This work	0.9 Hz, 0.75 g	21.7 μW	0.033	0.27%
Galchev 2012 [63]	2 Hz, 2 g	10.4 μW	0.057	0.13%
Renaud 2009 [83]	1 Hz, 1 g	47 μW	0.07	0.18%
Pillatsch 2012 [87]	0.25 Hz ,0.28 g	370 μW	0.063	1.00%

low motion ratio. Furthermore, it is expected that higher efficiencies can be achieved when a larger transducer is used in which more piezoelectric material is deformed, and when the used volume is further optimized.

5.4 CONCLUSION

In this work we have demonstrated a new ortho-planar mechanism design consisting of a cantilever and two post-buckled flexures mounted at right angles. The out-of-plane stiffness of the mechanism can be tuned by manipulating the width of the flexures. Moreover, it was demonstrated that a statically balanced configuration could be achieved by tuning the width of the balancing flexures to 0.52 mm. The mechanism was prototyped using laser micro-machining and subsequently preloaded using a packaging method called package-induced preloading. The statically balanced property of the mechanism was experimentally validated by a measurement of the force-deflection relation.

Furthermore, a piezoelectric energy harvester prototype is fabricated by replacing the cantilever of the mechanism with a piezoelectric transducer. The power output of the energy harvester is evaluated at an low-frequency excitation of sub 1 Hz using a linear stage. Under these conditions, the statically balanced energy harvester demonstrates a relevant efficiency and greatly improved performance compared to a configuration in which the flexures were removed. Therefore, it can be concluded that static balancing can be used to improve the performance of piezoelectric energy harvesters for low-frequency vibrations.

6 APPLICATION TESTING USING REPLICATION OF HEARTBEAT MOTION

The lifespan of pacemakers can be extended by extracting kinetic energy from the beating of the heart and using it to replenish the batteries. However, the accurate replication of the heartbeat motion has received little attention. In this work, a method is proposed with which the vibration environment as experienced by an implanted pacemaker can be replicated in the lab such that vibration energy harvesters can be tested under realistic conditions. For this purpose, a heartbeat motion generator is developed with which unique signals of vibration environments can be constructed for arbitrary heartrates. Furthermore, an experimental setup is demonstrated in which a linear stage with air-bearings and position feedback can replicate this motion. Experiments are carried out in which heartbeat motions of 60, 80, 100 and 120 bpm were replicated and used to test a prototype of a low-frequency energy harvester.

6.1 INTRODUCTION

Each year more than a million pacemakers are implanted to treat arrhythmias. A major technological development in this space is the leadless pacemaker, which is up to an order of magnitude smaller than the conventional system. This system eliminates the most vulnerable components and greatly simplifies the implantation procedure. However, the longevity of these devices is limited by the lifespan of their built-in batteries. Typically the batteries last around seven years and surgery is required to replace the batteries, which brings additional costs and risks [1, 2].

To overcome this limitation, it has been proposed that kinetic energy in the form of motion or vibration can be extracted from the beating of the heart through miniaturized devices called vibration energy harvesters (VEHs). Moreover, the extracted energy can be used to continuously replenish the battery of the pacemaker to extend its longevity such that replacement surgeries are required less frequently, if at all. In literature, different groups have developed a wealth of VEHs to study this case [164–176]. While in vivo studies provide excellent validation, lab tests are often much more convenient during the design and optimization of such

systems. For this purpose, various approaches have been demonstrated.

Tashiro et al. [164, 165] presents a setup in which the vibrations of a canine heart are measured with an accelerometer and replicated by simulator consisting of a vibrating table driven by a stepper motor. It is stated that the prototype was therefore forced to move as if it were attached to the heart wall. Zurbuchen et al. [166] uses a setup on which the harvester is fixed on a piston that glides in a shaft and is actuated by a stepper motor. The system is programmed to follow a reciprocating motion with a constant acceleration (i.e. the applied acceleration is a square wave) that corresponds to the acceleration of 6.7 $\mathrm{m s^{-2}}$ found in measurements done on pigs with implanted accelerometers. Jackson et al. [167, 168] mimics the vibration environment of the heart by sending custom waveforms to an electromagnetic shaker. The generation of the waveforms was based on measurements of Brancato et al. [177, 178] and resulted in various signals containing 35-50 ms vibration impulses with frequencies of 1-4 Hz representing 60-240 bpm. However, in all of these studies, little detail is provided on how well these approaches are able to replicate the vibration environment. This is important as these tests may not be representative if the vibration environment is not accurately replicated [179]. Especially when acceleration measurements are used to drive electromagnetic shakers at low frequencies, it is very important to correct for the dynamics of the shaker itself [180].

In this work, the motion of the heart at the location of an implanted pacemaker is studied with the goal to build signals with which this vibration environment can be described for various heart rates. Furthermore, a method is proposed with which these vibration environments can be accurately replicated in the lab. The research objective is to study the performance of a low-frequency energy harvester under conditions comparable to a vibration environment of an implanted pacemaker.

In Section 6.2 the development of the heartbeat motion generator is discussed. Section 6.3 presents the experimental setup and procedure as well as the mechanical design and fabrication of a low-frequency energy harvester. The results and discussion is presented in Section 6.4, and the conclusions are listed in Section 6.5.

6.2 DEVELOPMENT OF A HEARTBEAT MOTION GENERATOR

The leadless pacemaker is preferably implanted on the inside of the right ventricle (RV) in the apical or mid-septal region [181], as shown in Figure 6.1(A). Currently, no accurate data on the motion of this tissue is available for humans. Therefore, information on the motion of this tissue will be collected from three sources of data: epicardial acceleration measurements from literature, acceleration measurements on the outside of the chest, and

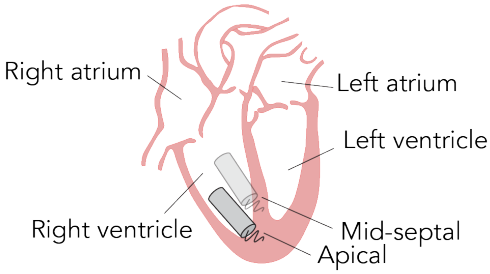

Figure 6.1: Schematic of the location of the implanted leadless pacemaker in the right ventricle.

echocardiography. The data from these sources will be analyzed and used to build a heartbeat motion generator: an algorithm with which signals can be generated that can be used to replicate the vibration environment of a pacemaker in the lab.

HEARTBEAT MOTION DATA SOURCES

The first source were epicardial acceleration signals from Grymyr et al. [182], where an accelerometer was used to capture the heartbeat vibration environment in five pigs. The accelerometer used is a 3D accelerometer (KXM52-1040, Kionix, Inc., NY, USA) with a dimension of $5 \times 5 \times 2$ mm and a sampling frequency of 500 Hz. One accelerometer is placed in the left ventricle apical region and the second one is placed in a basal lateral region. During the measurements the chest was left open and the pigs were placed in dorsal supine position.

Next, acceleration measurements are performed with an accelerometer attached on the outside of the chest. The accelerometer used for this experiment is a 3D accelerometer (356A32, PCB, NY, USA) with a dimension of 11.4 x 11.4 x 11.4 mm and a sampling frequency of 2048 Hz. Measurements are performed on three men (age 23-28) with normal hearts in rest and during exercise. The accelerometer is attached on the outside of the chest at approximately the location of the apex.

Lastly, Speckle Tracking Echocardiography (STE) measurements are performed at the Leiden University Medical Center (LUMC), the Netherlands, on nine patients (4 woman/5 man, age 20-79) with normal hearts. A VIVID E95 (GE Healthcare) with a 2.5 MHz transducer is used and the data is analyzed offline using the EchoPAC software. The patients held their breath in order to prevent influence from respiratory motion and the drift compensation mode was turned on. The mean spatial resolution is 0.25 mm per pixel and the mean temporal resolution is 62 fps. The motion of the apical and mid-septal regions of the RV is measured in the longitudinal, circumferential and radial directions using the apical short axis view shown and four chamber view shown in Figures 6.2(A,B). For the longitudinal and radial direction derivative of the displacement is obtained to find the

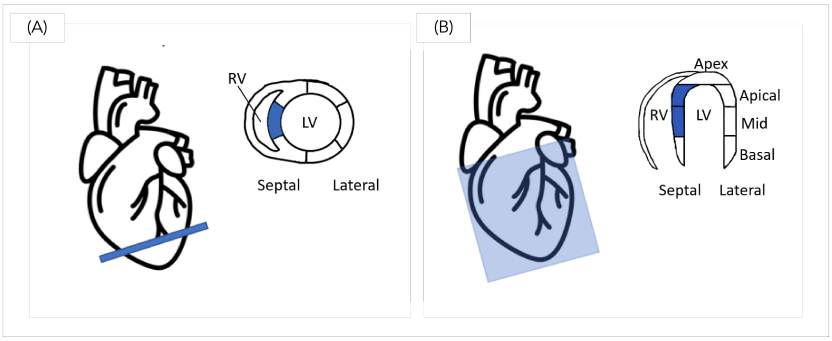

Figure 6.2: Picture identifying the cross-sections used in the STE measurements; A) apical short axis view; B) four chamber view.

velocity, and for the circumferential direction the motion is obtained in the rotation angle (degrees). In order to process the rotation angle, the radius of the heart in the apical view is determined in EchoPAC, to calculate the tangential velocity.

VIBRATION ENVIRONMENT ANALYSIS

The data from the three sources is analyzed to gain insight in the shape and amplitude of the acceleration, as well as the influence of the heart rate on the motion.

From the three sources, the epicardial acceleration signals were found to provide the most reliable information on the shape of the motion as they were measured directly on the heart. Moreover, the shape of the acceleration signals measured on the outside of the chest is significantly affected by the dynamic properties of the tissues in between, and the temporal and spatial resolutions of the STE measurements are too low to compute acceleration signals from which observations regarding the shape can be made. Based on the epicardial acceleration signals, it can be found that their shapes consist of a repeating pattern of two peaks. If the acceleration signals are synchronized with an ECG, such as shown in Figure 6.3(A), it can be observed that the larger peaks are simultaneous with the R-peaks in the ECG, and the smaller acceleration peaks are simultaneous with the end of the T-waves in the ECG. These moments in the ECG can respectively be linked to the ventricular contraction and relaxation [22]. Between the signals, differences are observed in the details of the acceleration peaks. They differ, for instance, in duration, amplitude and the number of oscillations after each peak. Similar results are observed from the signals obtained with an accelerometer attached on the outside of the chest, as well as in other acceleration signals found in literature for dogs, sheep, pigs and humans [23–26]. It can be concluded that the shape of the motion signal should contain a repeating pattern of two motions associated with the contraction

and relaxation of the ventricles.

The accelerations that were observed in the epicardial acceleration signals from pigs are significantly higher compared to the measurements done on humans. It was found that these signals contain two overestimations caused by a dynamic gravity component, and the open-chest conditions. The first overestimation is caused by a rotational motion of the heart that changes the orientation of the accelerometer with respect to gravity [183, 184]. The second overestimation results from the open-chest conditions, during which the accelerations are much greater than those that an implanted pacemaker may experience when the chest is closed [182]. The acceleration measurements on the outside of the chest, were not found to be representative either as vibrations were significantly damped due to the tissues in between the heart and the accelerometer. Although the data from the STE measurements does not contain detailed information on the shape of the signals, it was found that this can be used to identify the maximum amplitude of the acceleration from the isovolumic myocardial acceleration (IVA) [185, 186]. Using this method, average values of 0.63 $\mathrm{m s^{-2}}$ – 1.03 $\mathrm{m s^{-2}}$ were found for the nine patients at the regions where pacemakers are implanted. These accelerations correspond to those observed by Margulecsu et al. [187].

The analysis is concluded by studying the effect of the heartrate on the motion. Naturally, the heartrate is directly connected to the frequency with which the acceleration peaks are observed. However, it was observed from the measurements with the accelerometer on the outside of the chest during exercise that the heartrate also affects the amplitude of these peaks. This effect was also observed in literature [188–191], and it was found that the acceleration of the peak related to the contraction increased faster than the acceleration of the peak related to the relaxation.

HEARTBEAT MOTION GENERATOR

Through the combination of the data from sources, a heartbeat motion generator is constructed with which signals can be generated that represent the vibration environment of an implanted pacemaker at different heartrates. These signals are one-dimensional acceleration signals of the motion in the longitudinal direction. This direction was chosen because it contains the highest accelerations.

To build the signals, it is proposed to isolate waveforms of individual contraction and relaxation cycles from the measured acceleration signals and use them to synthesize new heartbeat signals. In order to do this, transfer function models can be estimated for the isolated cycles by fitting their impulse responses such that they match the measured accelerations. The heartbeat motion generator can now combine these transfer function models as building blocks in order to generate a new heartbeat motion signal. The desired heartbeat can be achieved by generating a series of impulses with a rate corresponding to the desired heartrate. An example of

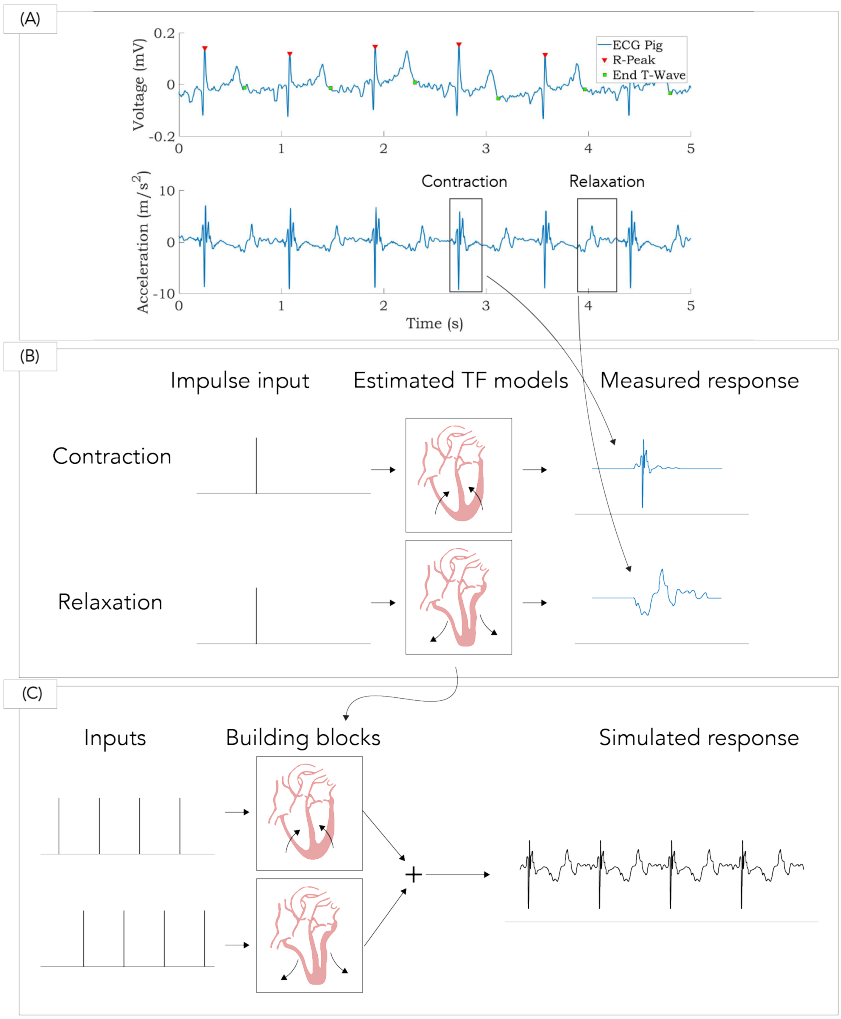

Figure 6.3: Proposed method to build the heartbeat signals, A) measured pig ECG and acceleration data with the individual contraction and relaxation cycles, B) estimation of transfer function models from the individual contraction and relaxation cycles, C) combination of the transfer function models as building blocks for a new heartbeat signal.

this method is shown in Figure 6.3, where individual cycles are extracted from the acceleration signals from [182] (Figure 6.3(A)) and used to estimate transfer function models (Figure 6.3(B)) with which a new heartbeat signal is synthesized (Figure 6.3(C)). Next, the data from the STE measurements can be used to scale these signals such that the accelerations match with those observed in human heart motion. Finally, an additional scaling can be applied to capture the dependency on the heartrate.

To allow the generator to generate unique series, building blocks may be randomly selected for every new signal. Moreover, it is proposed to incorporate some small variation in both the scaling, as well as the spacing between the impulses to reflect that every person has a different heartbeat, and that the heartbeat may change over time. In this way, unique signals for different heart rates can be generated quickly, which makes it easier to validate the performance of heartbeat-powered vibration energy harvesters for a broad range of conditions.

6.3 VIBRATION REPLICATION EXPERIMENTS

EXPERIMENTAL SETUP AND TESTING PROCEDURE

The performance of the energy harvesters is evaluated for low-frequency excitations using the setup shown in Figure 6.4. The setup consists of carriage (1) with air bearings that is driven by an ironless linear motor [TECNOTION UL-6N] controlled by a servo drive [KOLLMORGEN AKD-p00306] that moves over a 500 mm linear track (2). With this hardware, motions containing low-frequencies can be replicated very accurately due to the long stroke, low stiffness and low friction of the system. The applied motion is measured using an incremental encoder [RENISHAW TONIC T1000-05A] (3) and controlled using a position feedback loop. The prototype (4) is fastened on top of the stage and the output of the transducer is measured over a connected load R =100 kΩ. Furthermore, the acceleration is measured using accelerometer (5). The following experiments are conducted.

The procedure for the replication of the generated signals is as follows. First, the acceleration signals are integrated twice to obtain a position signal that the stage can track. To limit the drift, a first-order high pass filter with a cutoff frequency of 0.5 Hz is applied. The filtered signal is used as a reference input for the controller of the position loop, which is tuned to a bandwidth of 40 Hz. With this method, experiments were carried out in which heartbeat motions of 60, 80, 120 and 140 bpm were replicated. To validate the performance of an energy harvester under these conditions, a prototype was developed based on the design from [162] and will be discussed next.

MECHANICAL DESIGN OF THE LOW-FREQUENCY ENERGY HARVESTER

The concept shown in Figures 6.5(A,B) houses two vibration energy harvesters, one with flexures and one without. The energy harvester design consist of a piezoelectric transducer which is connected to a rigid shuttle and two flexures which are connected to the shuttle at right angles to the piezoelectric transducer. The initially flat flexures can be buckled by compressing them over a distance of dL. This process is called preloading and results in the flexures assuming a post-buckled shape that extends out of

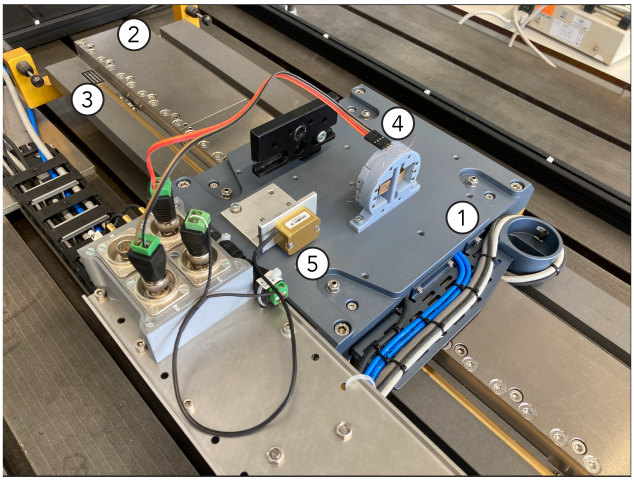

Figure 6.4: Experimental setup used to evaluate the performance of the system for low-frequency excitations.

plane. In this preloaded configuration, the flexures are bi-stable in the out-of-plane direction and provide a negative stiffness to the shuttle. This negative stiffness can be used to compensate the stiffness of the piezoelectric transducer. As a result, the flexibility of the energy harvester can be tuned.

The outside diameter of the system, $D = 53.6$ mm, is designed to match the dimension of the commonly used Micra leadless pacemaker at a scale of 8:1. The piezoelectric transducers as well as the balancing flexures are fabricated using a Spectra-Physics Talon 355-15 diode pumped solid-state (DPSS) UV laser system with a wavelength of 355 nm and maximum power of 15 W at 50 kHz. For the piezoelectric transducers, 0.23 mm thick audio buzzers (KEPO FT-41T-1.0A1-478) with a brass substrate thickness of $t_s = 0.1$ mm and a piezo thickness of $t_p = 0.13$ mm are machined to cantilevers with a free length of $L_p = 7.5$ mm and a width of $w_p = 10$ mm. Moreover, a taper is added in the transducers next to the shuttle to prevent excessive stresses at the sharp corners. The balancing flexures are machined from $t_f = 0.1$ mm thick spring steel with a free length of $L_f = 13.5$ mm and a width of $w_f = 1.5$ mm. The frame elements and an isolation layer between the top electrode of the piezo and the shuttle are 3D-printed from UV photosensitive resin using a SLA machine (PRUSA SL1). The shuttle consists of two square parts with sides L_m= 10mm and thickness $t_m = 5$ mm that were machined from brass and had a total mass of 8g. The system is assembled by bolting the shuttle parts together and thereby clamping the piezo and the flexure in place. Next, this assembly is clamped between the parts of the frame by bolts. In this step, the holes at the sides of the flexures are placed on dowel pins inserted in the frame. As a result, the flexures are compressed and assume their

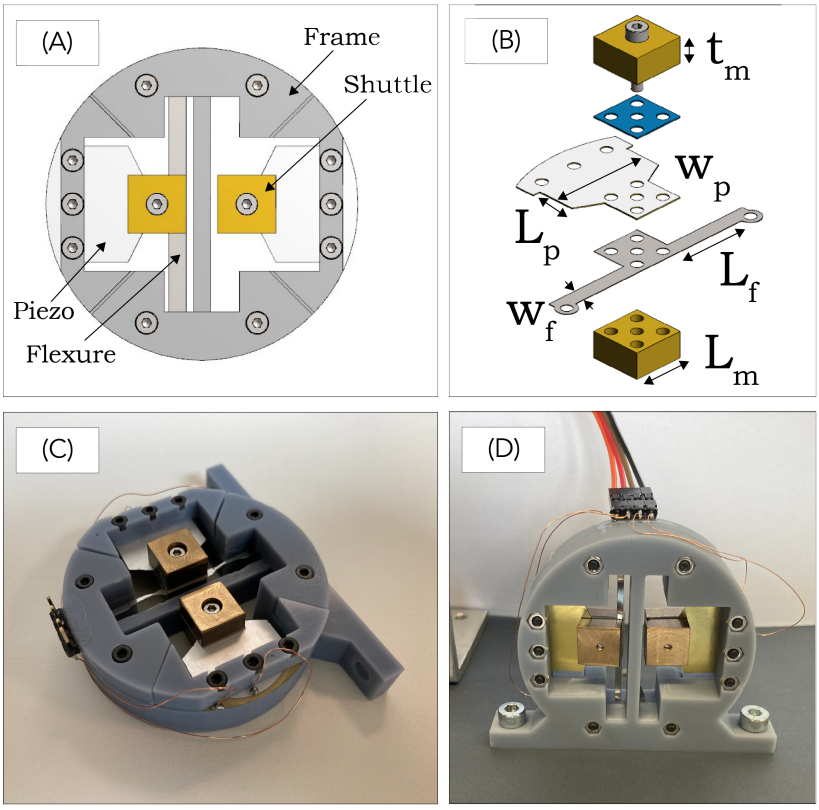

Figure 6.5: A) Mechanical design and components; B) Assembly and relevant parameters of the vibration energy harvesters; C/D) Assembled prototype.

Table 6.1: Parameters of the fabricated prototype.

Parameter	Symbol	Value
General		
Outer diameter (mm)	D	53.6
Shuttle dimensions (mm)	L_m, t_m	10 x 5
Piezoelectric transducer		
Free length (mm)	L_p	7.5
Width (mm)	w_p	10
Substrate thickness (mm)	t_s	0.10
Piezo thickness (mm)	t_p	0.13
Balancer flexure		
Free length (mm)	L_f	13.5
Width (mm)	w_f	1.5
Thickness (mm)	t_f	0.1

post-buckled configuration. Photographs of the assembled prototype are shown in Figure 6.1(C,D) and all parameters are summarized in Table 6.1.

6.4 RESULTS AND DISCUSSION

Figure 6.6(A-D) shows the results of the experiments in which the generated heartbeat motions are replicated on the linear stage at 60-120 bpm. In Figures 6.6(A-D)(i), the acceleration signals that were generated with the heartbeat motion generator described in section 6.2 are shown together with the accelerations that were measured during the replication of these signals on the linear stage. It can be seen that the generated signals clearly show the shape containing a repeating pattern of motions as associated with the contraction and relaxation of the ventricles. Moreover, all of the patterns are similar in general, but clearly show different details as a result of the introduced variances. Furthermore, the amplitudes of the peak accelerations in the 60 bpm and 80 bpm signals correspond to the values identified in section 2, and scale with increased heartrates.

Next, the generated signals are compared with the accelerations that were measured on the linear stage during the replication of the accelerations. It can be observed that the system is capable of achieving a very good tracking of the motion such that the accelerations are replicated with minimal errors. Slight differences between the acceleration signals are only found in parts where the acceleration changes rapidly and the system cannot keep up.

Figures 6.6(A-D)(ii) show the measured performance of the energy harvesters with and without flexures in response to the replicated heartbeat motion profiles. Moreover, the average power generated by the energy harvesters is shown in Table 6.2. From the tests on the heartbeat signals was found that for both energy harvesters the generated power increased rapidly for increasing heartrates. This is caused by the combination of the increased amplitudes of the accelerations at higher heartrates, as well as the increased heartrate itself which causes the energy harvesters to be excited more often. Furthermore, it can be observed that the energy harvester with the flexures showed an increased performance compared to the reference energy

Table 6.2: Power output of the harvester prototypes for various heart rates replicated on the stage.

Heartbeat motion profile (bpm)	Power without flexures (μW)	Power with flexures (μW)
60	0.02	0.12
80	0.04	0.26
100	0.13	0.73
120	0.63	3.34

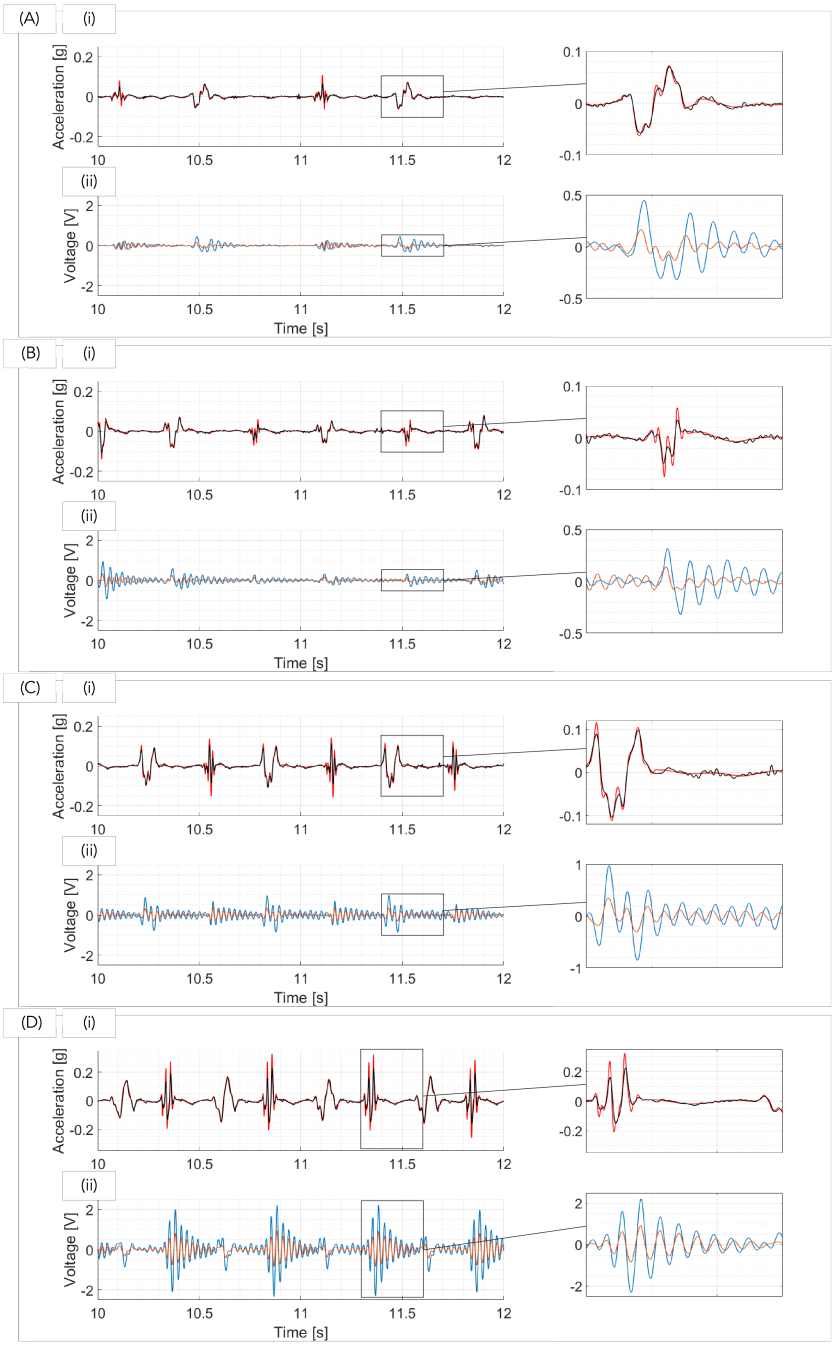

Figure 6.6: Comparison of (i) original and replicated acceleration and (ii) energy harvester performance; A) 60bpm; B) 80bpm; C) 100bpm; D) 120bpm; — generated acceleration signal; — measured acceleration during replication of the signal ; — harvester with flexures; — harvester without flexures.

harvester for all tested heartrates. This demonstrates that the stiffness compensation provided by the flexures can improve the performance of energy harvesters in real-world vibration environments that contain low-frequency vibrations.

6.5 CONCLUSION

In this work we have demonstrated a method to replicate the vibration environment as experienced by implanted pacemakers in the lab for the testing of piezoelectric energy harvesters. Three different sources of data are combined in order to develop a heartbeat signal generator with which unique heartbeat motion signals can be generated for different heart rates. This allows the convenient testing of heartbeat-powered vibration energy harvesters in the lab for a broad range of conditions.

Next, an experimental setup was developed with which the generated acceleration signals could be replicated in the lab though a feedback controlled linear air-bearing stage. Experiments are carried out in which heartbeat motions of 60, 80, 100 and 120 bpm were replicated. It was found that the setup was able to accurately replicate the generated heartbeat motions.

To study the performance of low-frequency energy harvesters in a heartbeat motion environment, a prototype housing two piezoelectric vibration energy harvesters was designed. One of the energy harvesters used post-buckled flexures to provide a negative stiffness with which the stiffness of the piezoelectric transducer was compensated. It is shown that the energy harvester with the flexures outperformed the reference energy harvester in all cases. Although the prototype did not generate enough output to power a pacemaker, it validates that stiffness compensation can be applied to improve the performance of vibration energy harvesters in real-world vibration environments.

7 MEMS IMPLEMENTATION IN SILICON

The usually high eigenfrequencies of miniaturized piezoelectric vibration energy harvesters can be significantly lowered by applying stiffness compensation. In this work, a micro-scale design is proposed in which this is achieved by using post-buckled flexures to offset the stiffness of a piezoelectric transducer. In the MEMS design, a preloading feature is integrated by which the necessary preload can introduced at micro-scale with high precision. The device was simulated using a finite element model, and it was demonstrated that 99.6% of the original stiffness of the piezoelectric transducer could be compensated by the preloaded mechanism. As a result, an eigenfrequency of <30 Hz *was calculated for the MEMS device with a mass of 0.56* mg. *This demonstrates that stiffness compensation can be used in the design of piezoelectric MEMS vibration energy harvesters for low-frequency applications.*

7.1 INTRODUCTION

Vibration energy harvesting research is pursuing the development of increasingly smaller devices that extract energy from low-frequency ambient motion sources, such as human motion. For these devices, piezoelectric transducers have attracted great interest due to their high power densities and miniaturization capabilities [24]. Moreover, piezoelectric transducers are especially suitable as they can be integrated in compliant mechanisms and thereby benefit from the advantages these mechanisms offer in terms of manufacturing processes, compactness and resistance to wear [29]. A particularly common configuration used at micro-scale is the cantilevered design as shown by [42, 192, 193].

Du et al. [42] presents a MEMS energy harvester was fabricated from a silicon-on-insulator (SOI) wafer and used aluminum nitride (AlN) as a piezoelectric material. The device with an area of 12.25 mm^2 and mass of 5.6 mg was able to harvest up to 40.6 μW from an applied vibration an applied acceleration of 0.3 g at a frequency of 199 Hz. Biswal et al. [193] optimizes a hole in a cantilever-based energy harvester to lower the eigenfrequency of the designed structures from 1.96 kHz to 1.56 kHz. The optimized structure, with an area of 0.3 mm^2, and mass of 0.069 mg demonstrated a power output of 490 nW under a 1 g acceleration at 1.56 kHz. A larger device with an area of

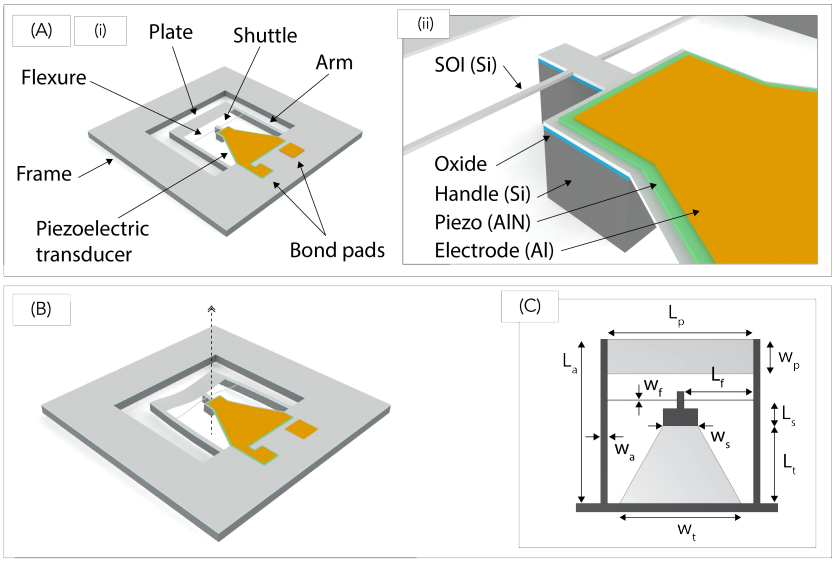

Figure 7.1: A) Mechanical design of the piezoelectric energy harvester showing (i) the components and (ii) the layers used in the micromachining process. B) Schematic of the preloaded device resulting in a low eigenfrequency in the illustrated direction. C) Relevant parameters of the proposed design.

an area of 78 mm^2 and a mass of 28.9 mg is demonstrated by Andosca et al. [192]. The device had a resonance frequency of approximately 5 Hz and could generate up to 128 µW under a 1 g excitation applied at resonance. However, a problem with these miniaturized devices is that their natural frequencies are relatively high. Upon miniaturization, the mass scales down at an increased rate compared to the stiffness and as a result a greatly reduced efficiency is observed when excited by real-world vibrations [26]. In prior art, it was noted that "*without the attached mass, it is unrealistic if not impossible to produce a MEMS harvester responding to a frequency below 200* Hz" [192].

In this work, an alternative approach is taken in which the stiffness of the miniaturized device is reduced through stiffness compensation. This is achieved by leveraging a negative stiffness structure in the form of post-buckled flexures to act as a balancer that counteracts the (positive) stiffness of the piezoelectric transducer. The research objective of this work is to demonstrate that stiffness compensation can be used to achieve MEMS vibration energy harvesters for low-frequency (<100 Hz) applications without the need for large attached masses.

In Section 7.2 the mechanical design and method for tuning the stiffness of mechanisms are introduced. Furthermore, the fabrication of the prototypes and experimental methods are discussed. The results are shown and discussed in Section 7.3, and the conclusions are listed in Section 7.4.

7.2 METHODS

MECHANICAL DESIGN

Figure 7.1(A) shows a schematic view of the proposed design of the stiffness-compensated mechanism, which is designed following the PiezoMUMPs design rules [194]. This process uses Silicon-on-insulator (SOI) wafers on which the designs of multiple users are fabricated simultaneously through a prescribed five-mask-level fabrication process. The design comprises of a frame, a piezoelectric transducer, a shuttle, two flexures, two arms and a plate. The frame, shuttle and the arms are full-width structures (i.e. the device layer is not released), while the transducer, flexures and the plate are released from the handle. On top of the silicon device layer of the piezoelectric transducer, a layer of AlN and an Al electrode are deposited. The top surface of the silicon is doped and acts as the bottom electrode. Electrical interfacing of the device is achieved through the bond pads on the side of the frame.

The working principle of the stiffness compensation is as follows; the plate mounted between the arms is deformed in the out-of-plane direction and thereby pulls the arms inwards. The deformation of the plate can be achieved through packaging [100] in a reproducible fashion. As a result of the arms being pulled inward, the flexures are compressed and begin to buckle. This process is called preloading and results in the flexures assuming a post-buckled shape that extends out of plane. In this preloaded configuration, the flexures exhibit a negative stiffness on the shuttle which compensates for the stiffness of the cantilevered piezoelectric transducer. As a result, the device has a very low stiffness in the out-of-plane direction illustrated in Figure 7.1(B). Moreover, due to the stiffness compensation, the eigenfrequency of this device is very low for a MEMS device. The relevant parameters for this design are shown in Figure 7.1(C) and summarized in Table 7.1.

Table 7.1: Relevant parameters of the proposed design.

Parameter	Symbol	Value
Layer thicknesses		
Handle thickness (um)	t_h	400
Oxide thickness (um)	t_{ox}	1
Device layer thickness (um)	t_d	10
Piezoelectric transducer thickness (um)	t_{AlN}	0.5
Electrode thickness (um)	t_e	1.02
Geometric parameters		
Piezoelectric transducer dimensions (mm)	L_t, w_t	2.25 x 3.5
Flexure dimensions (mm)	L_f, w_f	2 x 0.045
Shuttle dimensions (mm)	L_s, w_s	0.75 x 1
Arm dimensions (mm)	L_a, w_a	4.75 x 0.2
Plate dimensions (mm)	L_p, w_p	4.2 x 1

MECHANICAL ANALYSIS USING FINITE ELEMENT MODEL

To simulate the mechanical behavior of the proposed design, a finite element model was built in ANSYS APDL in which the design was meshed using beam elements (beam188). In this model, linear elastic material models were used with the properties listed in Table 7.2. In these meshes, the composite cross-sections of this design were modeled as uniform cross-sections in which an equivalent elastic modulus, E_eq, was determined through Equation (7.1).

$$\frac{E_{eq}\, t_c^3}{12} = \sum_{n}^{N} \frac{E_n\, t_n^3}{12} + E_n\, t_n\, y_n^2 \tag{7.1}$$

Where , y_n is the distance with respect to the neutral axis of the composite cross section, E_n and t_n are the Young's modulus and the thickness of the n^{th} layer, and $t_c = \sum_n^N t_n$ is the thickness of the composite layer.

To evaluate the force-deflection behavior of the stiffness-compensated device, the simulation is carried out in the steps shown in Figures 7.2(A-D). Figure 7.2(A) shows the unloaded configuration in which the frame at the base of the cantilever and the arms is fixed in all directions, and a displacement of 400 µm was applied to the middle of the plate. Due to the applied deflection, the plate starts to pull on the arms and thereby causes the arms to move inwards by 21.5 µm. Because the arms are 200 µm wide and 400 µm thick, their deflection is predominantly in the in-plane direction. As a result of the arms moving inwards, the flexures are compressed and buckle to obtain the configuration shown in Figure 7.2(B).

After the buckled shape was achieved, the arms were fixed in place and the shuttle was moved in the out-of-plane direction over a displacement of 250 µm. During this motion, of which the extreme positions are shown in Figures 7.2(C-D), the reaction force provided by the mechanism is recorded at regular intervals to determine the force-deflection behavior.

7.3 RESULTS

In Figure 7.3, the force-deflection relations resulting from the simulations are shown for the stiffness-compensated mechanism after preloading. In order to demonstrate the sensitivity of the stiffness compensation, the width of the balancing flexures is varied between 40 µm, 45 µm, and 50 µm. From the figure

Table 7.2: Materials properties used for FEM simulations; ρ mass density; E Young's modulus; ν Poisson's ratio.

Material	Properties	Ref
Si	ρ = 2.30 g/cm3; E = 130 GPa; ν = 0.28;	[195]
SiO2	ρ = 2.20 g/cm3; E = 72 GPa; ν = 0.2;	[196, 197]
AlN	ρ = 3.26 g/cm3; E = 330 GPa; ν = 0.22;	[110, 111, 114, 143, 144]
Al	ρ = 2.71 g/cm3; E = 69 GPa; ν = 0.34;	[198]

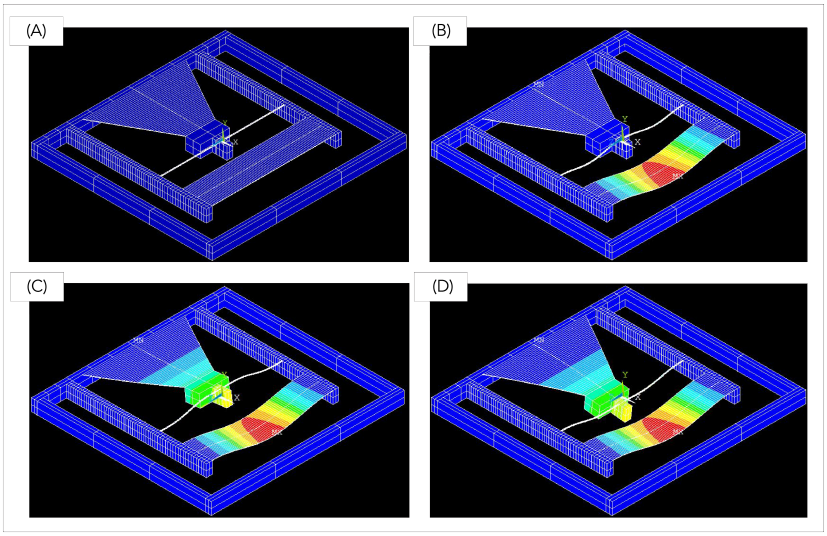

Figure 7.2: Simulation steps showing the deformation of the mechanism A) in the initial undeformed configuration; B) after preloading C) in the upwards deflected position D) in the downwards deflected position.

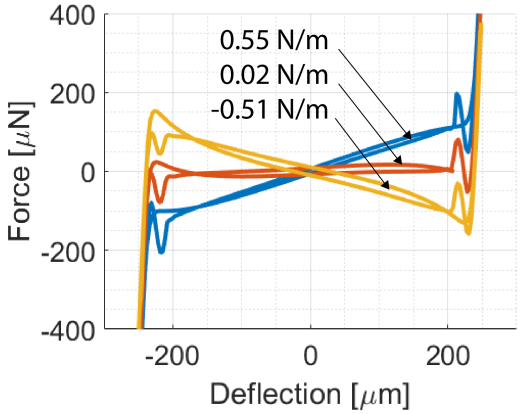

Figure 7.3: Simulated force-deflection relation of the stiffness-compensated mechanism after preloading for different widths of the balancing flexure.

can be observed that these variations lead to a mechanism with a positive stiffness of 0.55 $\mathrm{N\,m^{-1}}$, a mechanism with a near-zero-stiffness of 0.02 $\mathrm{N\,m^{-1}}$, and a bi-stable mechanism with a negative stiffness of approximately -0.51 $\mathrm{N\,m^{-1}}$ over the middle part of its range of motion.

7.4 DISCUSSION

PRELOADING AT MICRO-SCALE

Preloading of mechanisms at micro-scale poses a significant challenge because physical handling without causing damage is difficult due to the high precision that is required [46]. In prior art, alternative MEMS preloading approaches have been demonstrated by leveraging the stresses resulting from the deposition of thin-films during the fabrication process [49, 50]. However, these approaches often require careful tuning of the process parameters to achieve the desired amount of preloading and may therefore not be efficient for prototyping. This work presents a novel MEMS preloading feature consisting of two arms and a plate which is integrated in the die. This feature allows very precise control over the applied preload because the plate acts as a lever. In the simulations, it was found that a 400 µm displacement applied in the middle of the plate resulted in a 21.5 µm inward displacement of the arms. In order to apply the preload in a repeatable fashion, the displacement of the plate may be provided by a package, a method called package-induced-preloading [100].

FORCE-DEFLECTION RELATIONS OF THE PRELOADED MECHANISMS

From the force-deflection relations of the preloaded mechanisms shown in Figure 7.3 it can be observed that the mechanisms have a range of motion with an amplitude of 200 µm in which they are relatively compliant. For larger deflections, the force-deflection relation rapidly steepens as a result of the mechanisms being straightened and loaded in tension. In the proposed mechanisms, the stiffness within the range of motion is relatively linear as a result of the flexures being placed at right angles to the motion of the cantilevered piezoelectric transducer. Nevertheless, two load paths can be identified in the force-deflection relations, similar to the mechanisms demonstrated in previous work [89]. These load paths correspond to the two configurations of the post-buckled flexures that can be identified as "knee-up" and "knee-down" and are the result a small amount of torsion induced in the flexures during the cantilevered motion. However, because these load paths are such close together, they can be assumed as a single force-deflection relation in practice. Furthermore, the peaks that can be observed in the force-deflection relations near the ends of the range of motion are likely numerical artifacts that occur because the solver switches between the load paths. In earlier work, these peaks were also found in the simulations, but not measured during experiments [89].

STIFFNESS COMPENSATION AND APPLICATION TO ENERGY HARVESTING

In the proposed mechanism, the stiffness of the piezoelectric transducer (i.e. without the flexures) was found to be approximately 4.72 $\mathrm{N\,m^{-1}}$. The mass of the silicon shuttle is 0.56 mg such that the eigenfrequency of a device without the flexures would be approximately 460 Hz. With the addition of the stiffness compensation provided by the post-buckled flexures, this stiffness can be greatly reduced. The amount of stiffness compensation can be tuned by designing the length and width of the flexures. Compared to the length, the width is a more convenient parameter to fine-tune the stiffness compensation because of two reasons. First, the flexural rigidity of a beam depends linearly on its width (compared to the cubic relation to the length) and thereby reduces the uncertainty of fabrication tolerances. Secondly, manipulating the width does not affect the range of motion of the device. For a preloaded mechanism with a flexure width of w_f = 45 μm, the linearized stiffness that can be found from Figure 7.3 is 0.02 $\mathrm{N\,m^{-1}}$. This constitutes to a 99.6% reduction in stiffness of the piezoelectric transducer, and as a result the eigenfrequency of the preloaded mechanism was calculated to be <30 Hz. For a MEMS device, this is a very low eigenfrequency and demonstrates that stiffness compensation can be used to construct MEMS vibration energy harvesters for low-frequency applications.

Moreover, it was also demonstrated that a bi-stable configuration can be achieved for the proposed design. In some applications, such bi-stable vibration energy harvesters may be preferred over resonators as their performance is less sensitive to the frequency of the driving motion and instead depends on the applied acceleration [66]. However, with the inertia of the current shuttle, a force of only 5.6 μN is generated by a 1 g acceleration. Due to fabrication tolerances, it may not be feasible to tune the force-deflection relation of the proposed mechanism such that it can be used for these conditions.

FABRICATION AT MICRO-SCALE

The simulations indicated that with the use of stiffness compensation in the proposed designs, piezoelectric MEMS vibration energy harvesters with resonance frequencies <30 Hz can be achieved. Future work will be aimed at the experimental validation of the results from the simulations, as well as the characterization of the energy harvesting performance under real-world conditions. The prototypes will be fabricated using the PiezoMUMPs process from MEMSCAP. Figures 7.4(A-F) shows the designs of the masks and the order of the process. First, a pattern of oxide (dashed black) is patterned with the PADOXIDE mask on the device layer (red) as shown in Figure 7.4(A) in order to provide electrical insulation from the non-active regions of the piezoelectric material. Next, the piezoelectric material (dashed purple) and electrodes (blue) are patterned with the PZFILM and PADMETAL masks as shown in Figures 7.4(B-C), respectively. The silicon device layer is patterned

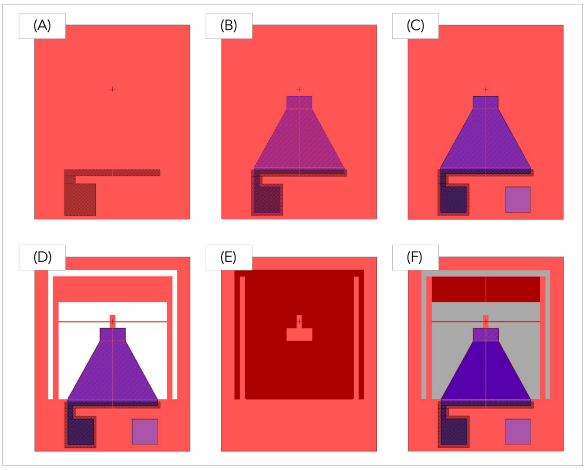

Figure 7.4: Overview of the masks designed for the fabrication of the prototypes; A) PADOXIDE mask, B) PZFILM mask, C) PADMETAL mask, D) SOI mask, E) TRENCH mask, F) Resulting device.

using the SOI mask shown in Figure 5(D), in which the white areas are the exposed oxide layer on top of the handle. Figure 7.4(E) shows the pattern of the final TRENCH mask that will be etched in the handle from the back of the wafer such that the resulting device shown in Figure 7.4(F) is obtained.

7.5 Conclusion

In this work we have presented a design and simulation of a MEMS piezoelectric vibration energy harvester for low-frequency applications. In the mechanism, stiffness compensation is applied by using a negative stiffness provided by post-buckled flexures to offset the stiffness of the piezoelectric transducer. This post-buckled state is achieved through preloading the device with a special preloading feature that is integrated in the design. The finite element simulations showed that when the width of the flexure was designed at w_f = 45 µm, a stiffness compensation of 99.6% could be achieved by the preloaded device. As a result of the stiffness compensation, an eigenfrequency of <30 Hz was calculated. For a MEMS device, this is a very low eigenfrequency and demonstrates that stiffness compensation can be used to construct MEMS vibration energy harvesters for low-frequency applications.

8 CONCLUSION

This chapter provides a discussion of the material presented in the previous chapters, outlines the main contributions and considers their impact in a broader perspective.

8.1 DISCUSSION

The impact of this work is that it enables the design of efficient energy harvesters from many real-world environments in which the ambient motion consists of mostly low-frequency vibrations. Examples of such environments include human motion, vehicle engines, industrial machines and winds or waves. In applications where battery replacement is expensive, regulated and/or risky, energy harvesting may have a large commercial potential as an alternative to batteries. Particularly in implanted medical devices such as leadless pacemakers, a convincing case can be made for the application of this technology. Furthermore, low-frequency energy harvesting may provide considerable opportunities for the future exploitation of wireless sensor networks in various areas.

Beyond the application in energy harvesting, the ideas developed in this thesis can be more generally applied to piezoelectric MEMS transducers where stiffness negatively affects the performance. Examples include sensors such as accelerators, geophones and microphones, but also actuators such as speakers and pumps. Similar to the case of energy harvesting, stiffness compensation can be applied to improve the sensitivity of these devices at low-frequencies.

Besides the mechanical designs, this work has yielded three more general contributions to the fields of vibration energy harvesting and compliant mechanisms. The first is the development of a framework for vibration energy harvesting based on an efficiency-centered approach and a new metric to describe the size of the device relative to the amplitude of the applied vibration. The second is the conception of a more general theory that describes how the critical loads of a buckled mechanism relate to its post-buckled force-deflection relation, and how this can be used in the design of stiffness compensated mechanisms. The third is the development of package induced preloading as an enabling technology for the preloading of compliant mechanisms at small scales. These developments will be discussed successively.

DEVELOPMENT OF A FRAMEWORK

The first more general contribution of this thesis to the field of vibration energy harvesting is the development of the framework presented in Chapter 2 that hinges on two ideas. The first of these ideas is that the performance of a vibration energy harvester should be judged by an efficiency-centered approach instead of a power-centered approach such that vastly different generators operating in different environments can be compared. While this idea is not exactly new [3, 16, 26–28], the practical implementation proposed in Chapter 2 goes beyond the state-of-the art in two ways. First, the proposed generator figure of merit, (FoM_G), improves on the existing figures of merit by eliminating the bias towards generator shape and material. Secondly, the FoM_G is intended be evaluated for many operating conditions such that a frequency response function in terms of efficiency as shown in Figure 2.2 is obtained. This frequency-efficiency relation greatly improves the insight that is gained in the performance of the generator compared to a single reported value. Nevertheless, for the comparison of multiple generators it is often desired to compare only a limited number of values, and therefore the peak efficiency (η_{pk}) and the normalized half-efficiency bandwidth (BW_{nhe}) can be derived from the frequency-efficiency relation to capture the performance of the generator in only two variables.

The second idea is that it is not necessarily the frequency which makes low-frequency energy harvesting challenging, but rather the size of the device[1] in relation to the amplitude of the applied motion. After all, there is no reason why we couldn't design a energy harvester, for example in the form of a piezoelectric cantilever with a proof mass, with a natural frequency of 1 Hz. However, it would be infeasible to achieve a relevant efficiency if we apply a 1g excitation to this system at 1 Hz and only allow the cantilever to deflect 10 mm. To quantify this effect, a new metric called the motion ratio (λ) was proposed. It can be argued that in the design of vibration energy harvesters for low-frequency applications, this metric may be more relevant than the frequency of the applied motion as resonance cannot be used anyway due the limited space.

The ambition was to use this framework to analyze the experimental work vibration energy harvesters reported in literature, generalize the results and compare the performances of different strategies. This approach was successful to a great extent and resulted in the overviews presented in Figures 2.5 and 2.6. However, there are some important limitations that should be discussed. First of all, this analysis suffers from a huge participation bias as it requires quite a number of parameters in order to evaluate the FoM_G. Over 500 research articles were analyzed during this study, and it was found that only 25 of those reported sufficient information to evaluate the FoM_G. Furthermore, there are large variations in the quality of the transducers, build quality and the overall degree of optimization

[1] To be precise, the internal travel limit is the actual parameter we are looking for, but this is so rarely reported in practice that device size is a more suitable alternative.

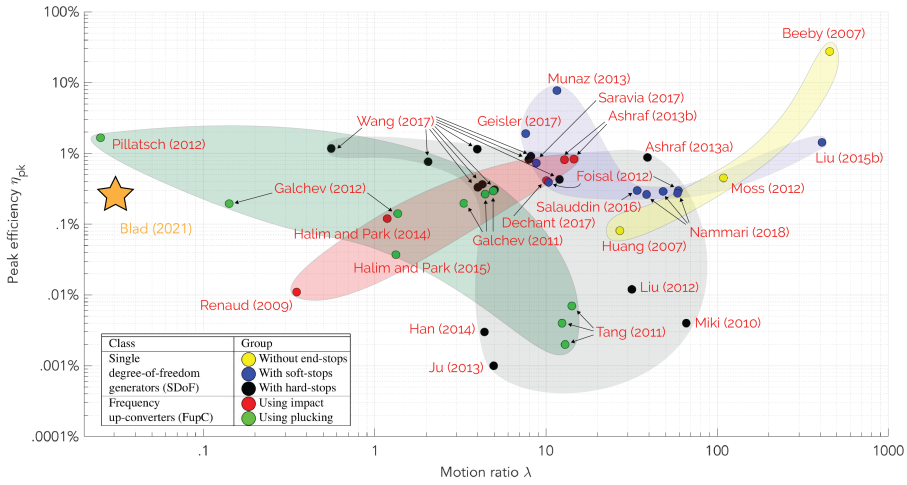

Figure 8.1: Reproduction of the overview shown in Figure 2.5 in which the experimental results from Chapter 5 have been indicated with a yellow star.

between the reported generators. As a result, the results could be generalized only to limited extent and the intended comparison between the different strategies lacks solid conclusions.

Nevertheless, new research can keep being added using this framework such that more substantial conclusions can inevitably be drawn in the future. To lead by example, the overview of Figure 2.5 was reproduced and the experimental results of Chapter 5 have been added in the overview shown in Figure 8.1. It can be observed that this energy harvester was tested at a very low motion ratio, among the lowest ever reported in literature[2], and already demonstrates a relevant efficiency despite the lack of optimization. This provides further evidence that the proposed approach based on stiffness compensation is an effective strategy to design energy harvesters for low-frequency applications.

DEVELOPMENT OF THEORY

A second contribution of this thesis was the conception of a theory that describes the relation between the buckling loads and the force-deflection relation of a buckled structure. This relation was suggested in literature, where it was noted that minimal stiffness was achieved when the critical loads of the first two buckling modes are the same [49], but it was never substantiated. During the development of designs that preceded the

[2] Considering that the generator reported by Pillatsch et al. [87] was tested by tilting the device with respect to gravity instead of applying a driving motion, an argument can be made that Chapter 5 demonstrated the lowest motion ratio ever reported in literature.

mechanisms outlined in Chapter 3, this behavior was used time and time again as a tool to predict general stiffness characteristics of a post-buckled mechanism from its linear buckling analysis. The desire to find a convincing explanation of why this tool worked motivated a closer study of the observed behavior. The subsequent investigation of the strain energy in a post-buckled beam led to the inception of two ideas that eventually resulted in the theory presented in Chapter 3. As the description given in Chapter 3 is rather brief, a more elaborate discussion on these ideas is repeated next.

The first idea was that the total strain energy in a post-buckled beam must be equal to the work done by the preloading. In slender beams, the moment of buckling happens at infinitesimal compression after which the reaction force is approximately constant with a magnitude equal to the critical load corresponding to the mode shape in which the beam is buckled [98, 99]. As a result, the strain energy of the post-buckled beam must be, in close approximation, equal to the product of the critical load and the preload displacement as stated by Equation 3.5. Moreover, this analysis should hold regardless of the mode shape in which the beam is buckled. Therefore, when the critical loads that correspond to two different mode shapes are equal, the strain energy of the post-buckled beam must be equal in both of these modes shapes. The second idea was that if the displacement field of the post-buckled beam moving between two mode shapes can be described as a linear combination of these mode shapes, the total strain energy during this motion can also be described as a combination of the strain energies of these mode shapes. The combination of these ideas leads to the conception of the theory that when the motion of a post-buckled beam can be described as the combination of two of its mode shapes of which the corresponding critical loads are equal, the total strain energy does not change during that motion. What this means in practice is that the beam is statically balanced and demonstrates zero-stiffness behavior.

While in this thesis the theory was strictly only shown for the beams presented in Chapter 3, its use as a design tool was again successfully applied in the mechanisms presented in Chapters 4-7, as well as those in [199]. Moreover, Numic et al. [200] the investigation from the perspective of energy was repeated for a more complex mechanism in an analytical fashion, and the same results were found. This supports the idea that this theory can be extended to more buckled mechanisms, and perhaps be generalized for all buckled mechanisms, and doing so is considered a logical line of further research.

DEVELOPMENT OF PACKAGE INDUCED PRELOADING

The third contribution is the development of package induced preloading as an enabling technology for stiffness compensation in miniaturized applications. The key challenge that was identified for the implementation of stiffness compensation at these scales is the introduction of the preload that is required to induce the initial buckling. At macro-scale, preloading is often

done through some assembly feature based on a lead-screw [37, 77]. A similar approach was taken in Chapter 3, where the mechanisms were preloaded through the assembly of a frame. However, it was found that such a method could not reliably be used at smaller scales [46, 47]. For this purpose, a new method called package induced preloading was developed. Compared to methods where beams are buckled by pushing their ends towards each other, improved precision and repeatability can be achieved.

In the first iteration of this method, which was demonstrated in Chapter 4, a single packaging element was used over which the mechanism was laminated and fixed with double-sided adhesive tape. Because the kapton-based mechanisms had a negligible flexural rigidity, this method provided sufficient fixation. For the stainless steel mechanisms used in Chapter 5, a next iteration of this method was necessary. Here, the mechanisms were sandwiched between two packaging elements that were bolted together in order to achieve the required deformation of the frame. Finally, in Chapter 7, a subsequent iteration of this method is presented in which this method was made compatible with the design rules specified for the intended microfabrication process. This main difference compared to the design presented in Chapter 5 is that in this design only a single feature is going to be deformed by the package.

In the current designs, package induced preloading is achieved by deforming features in the out-of-plane direction. These may also be deformed in an in-plane fashion to achieve a similar effect. A particularly convenient embodiment that can be thought of is one in which a package can be twisted to induce the preloading. Further extension of this method aimed at the application for the preloading of MEMS is identified as a major opportunity for further research and is therefore highly recommended.

8.2 CONCLUSION

The limitations of batteries imposed on implanted medical devices such as pacemakers motivated the desire to develop miniaturized vibration energy harvesters for low-frequency motion. Piezoelectric transducers integrated in compliant ortho-planar mechanisms were found to be especially suited for this purpose due to their high energy densities and compatibility with MEMS fabrication processes. The particular challenge is to overcome the inherent stiffness of the piezoelectric material such that the devices become responsive to low-frequency motion. It is in this context that the main objective of this thesis was formulated as the development of an effective strategy and the necessary technologies to enable vibration energy harvesting from low-frequency motion with miniaturized devices.

Following the proposed approach, the integration of stiffness compensation in the design of compliant ortho-planar mechanisms initially resulted in the mechanism designs presented in Chapter 3, and their MEMS implementation reported in Chapter 4. These designs demonstrated great

reductions in the out-of-plane stiffness of the mechanisms, and reported the application of stiffness compensation in a piezoelectric energy harvester for the first time. However, in these designs the force-deflection relations shown in Figure 3.5 were inherently nonlinear over the working range of the device, which limited the stiffness compensation that could be achieved.

Further development of the approach addressed this issue and yielded the mechanism design presented in Chapter 5. In this design, the stiffness compensation could achieved to such an extent that the resulting mechanism may be identified as statically balanced. Successively, this design was implemented in a piezoelectric energy harvester which demonstrated a relevant efficiency when excited by a low-frequency motion of sub 1 Hz. Furthermore, the preliminary results reported in Chapter 6 and Chapter 7 showed that the superior performance of the stiffness-compensated design can also be expected when excited by real-world vibration environments, and when miniaturized to micro-scale.

In this study, significant advances have been made towards the development of miniaturized vibration energy harvesters for low-frequency applications. While MEMS-based piezoelectric transducers have seen decades of development, their application to energy harvesting from low-frequency motion has remained a major challenge due to the intrinsic stiffness of both the silicon and the piezoelectric materials. It was found that through the application of stiffness compensation, a technique from the field of statically balanced compliant mechanisms with which stiffness can be reduced or even fully nullified, miniaturized vibration energy harvesters can be made responsive to low-frequency motion without the need for large masses. Therefore, it was concluded that the strategy developed in this thesis provided a new perspective to address this challenge.

REFERENCES

[1] J. Senaratne, M. E. Irwin, and M. P. J. Senaratne, "Pacemaker Longevity: Are We Getting What We Are Promised?," *Pacing and Clinical Electrophysiology*, vol. 29, no. 10, pp. 1044–1054, 2006.

[2] M. R. Carrión-Camacho, I. Marín-León, J. M. Molina-Doñoro, and J. R. González-López, "Safety of Permanent Pacemaker Implantation: A Prospective Study," *Journal of Clinical Medicine*, vol. 8, Jan. 2019.

[3] P. D. Mitcheson, E. M. Yeatman, G. K. Rao, A. S. Holmes, and T. C. Green, "Energy Harvesting From Human and Machine Motion for Wireless Electronic Devices," *Proceedings of the IEEE*, vol. 96, pp. 1457–1486, Sept. 2008.

[4] J. C. Deharo and P. Djiane, "Longévité des stimulateurs cardiaques Remplacement du boîtier de stimulateur," *Annales de Cardiologie et D'angeiologie*, vol. 54, pp. 26–31, Jan. 2005.

[5] J. Z. Lee, S. K. Mulpuru, and W. K. Shen, "Leadless pacemaker: Performance and complications," *Trends in Cardiovascular Medicine*, vol. 28, pp. 130–141, Feb. 2018.

[6] A. Pfenniger, M. Jonsson, A. Zurbuchen, V. M. Koch, and R. Vogel, "Energy Harvesting from the Cardiovascular System, or How to Get a Little Help from Yourself," *Annals of Biomedical Engineering*, vol. 41, pp. 2248–2263, Nov. 2013.

[7] C. S. Raghavendra, K. M. Sivalingam, and T. Znati, *Wireless Sensor Networks*. Springer, Dec. 2006.

[8] I. F. Akyildiz and M. C. Vuran, *Wireless Sensor Networks*. John Wiley & Sons, June 2010.

[9] M. Abdulkarem, K. Samsudin, F. Z. Rokhani, and M. F. A Rasid, "Wireless sensor network for structural health monitoring: A contemporary review of technologies, challenges, and future direction," *Structural Health Monitoring*, vol. 19, pp. 693–735, May 2020. Publisher: SAGE Publications.

[10] L. Muduli, D. P. Mishra, and P. K. Jana, "Application of wireless sensor network for environmental monitoring in underground coal mines: A systematic review," *Journal of Network and Computer Applications*, vol. 106, pp. 48–67, Mar. 2018.

[11] P. Arroyo, J. L. Herrero, J. I. Suárez, and J. Lozano, "Wireless Sensor Network Combined with Cloud Computing for Air Quality Monitoring," *Sensors*, vol. 19, p. 691, Jan. 2019. Number: 3 Publisher: Multidisciplinary Digital Publishing Institute.

[12] X. Tang, X. Wang, R. Cattley, F. Gu, and A. D. Ball, "Energy Harvesting Technologies for Achieving Self-Powered Wireless Sensor Networks in Machine Condition Monitoring: A Review," *Sensors*, vol. 18, p. 4113, Dec. 2018. Number: 12 Publisher: Multidisciplinary Digital Publishing Institute.

[13] S. A. Kumar and P. Ilango, "The Impact of Wireless Sensor Network in the Field of Precision Agriculture: A Review," *Wireless Personal Communications*, vol. 98, pp. 685–698, Jan. 2018.

[14] S. Tarannum and S. Farheen, "Wireless Sensor Networks for Healthcare Monitoring: A Review," in *Inventive Computation Technologies* (S. Smys, R. Bestak, and l. Rocha, eds.), Lecture Notes in Networks and Systems, (Cham), pp. 669–676, Springer International Publishing, 2020.

[15] S. Roundy, P. K. Wright, and J. M. Rabaey, *Energy Scavenging for Wireless Sensor Networks: with Special Focus on Vibrations*. Boston, MA: Springer US, 2004.

[16] P. D. Mitcheson, T. C. Green, E. M. Yeatman, and A. S. Holmes, "Architectures for vibration-driven micropower generators," *Journal of microelectromechanical systems*, vol. 13, no. 3, pp. 429–440, 2004.

[17] M. Zhou, M. S. H. Al-Furjan, J. Zou, and W. Liu, "A review on heat and mechanical energy harvesting from human – Principles, prototypes and perspectives," *Renewable and Sustainable Energy Reviews*, vol. 82, pp. 3582–3609, Feb. 2018.

[18] S. Roundy, P. Wright, and J. Rabaey, "A study of low level vibrations as a power source for wireless sensor nodes," *Computer Communications*, vol. 26, no. 11, pp. 1131–1144, 2003.

[19] R. Rantz and S. Roundy, "Characterization of real-world vibration sources with a view toward optimal energy harvesting architectures," in *Industrial and Commercial Applications of Smart Structures Technologies 2016*, vol. 9801, p. 98010P, International Society for Optics and Photonics, Apr. 2016.

[20] R. Rantz, M. A. Halim, T. Xue, Q. Zhang, L. Gu, K. Yang, and S. Roundy, "Architectures for wrist-worn energy harvesting," *Smart Materials and Structures*, vol. 27, p. 044001, Mar. 2018.

[21] D. Zhu, M. J. Tudor, and S. P. Beeby, "Strategies for increasing the operating frequency range of vibration energy harvesters: a review,"

Measurement Science and Technology, vol. 21, p. 022001, Dec. 2009. Number: 2.

[22] S. D. Moss, O. R. Payne, G. A. Hart, and C. Ung, "Scaling and power density metrics of electromagnetic vibration energy harvesting devices," *Smart Materials and Structures*, vol. 24, p. 023001, Feb. 2015.

[23] J. Holterman and W. A. Groen, *An introduction to piezoelectric materials and applications*. Stichting Applied Piezo, 2013.

[24] A. Erturk and D. J. Inman, *Piezoelectric energy harvesting*. John Wiley & Sons, 2011.

[25] S. G. Kim, S. Priya, and I. Kanno, "Piezoelectric MEMS for energy harvesting," *MRS Bulletin*, vol. 37, pp. 1039–1050, Nov. 2012.

[26] S. Roundy, "On the Effectiveness of Vibration-based Energy Harvesting," *Journal of Intelligent Material Systems and Structures*, vol. 16, pp. 809–823, Oct. 2005.

[27] W. Q. Liu, A. Badel, F. Formosa, and Y. P. Wu, "A new figure of merit for wideband vibration energy harvesters," *Smart Materials and Structures*, vol. 24, p. 125012, Oct. 2015.

[28] S. P. Beeby, R. N. Torah, M. J. Tudor, P. Glynne-Jones, T. O'Donnell, C. R. Saha, and S. Roy, "A micro electromagnetic generator for vibration energy harvesting," *Journal of Micromechanics and Microengineering*, vol. 17, no. 7, p. 1257, 2007.

[29] L. L. Howell, "Compliant Mechanisms," in *21st Century Kinematics* (J. M. McCarthy, ed.), (London), pp. 189–216, Springer, 2013.

[30] L. L. Howell, S. P. Magleby, and B. M. Olsen, *Handbook of Compliant Mechanisms*. John Wiley & Sons, Apr. 2013.

[31] S. Kota, J. Joo, Z. Li, S. M. Rodgers, and J. Sniegowski, "Design of Compliant Mechanisms: Applications to MEMS," *Analog Integrated Circuits and Signal Processing*, vol. 29, pp. 7–15, Oct. 2001.

[32] F. Cosandier, S. Henein, M. Richard, and L. Rubbert, "The Art of Flexure Mechanism Design," 2017.

[33] H. Soemers, *Design Principles for precision mechanisms*. T-Pointprint, 2011.

[34] J. A. Gallego and J. L. Herder, "Criteria for the Static Balancing of Compliant Mechanisms," in *Proceedings of ASME 2010 International Design Engineering Technical Conferences and Computers and Information in Engineering Conference*, pp. 465–473, American Society of Mechanical Engineers Digital Collection, Mar. 2011.

[35] M. T. Todaro, F. Guido, L. Algieri, V. M. Mastronardi, D. Desmaële, G. Epifani, and M. D. Vittorio, "Biocompatible, Flexible, and Compliant Energy Harvesters Based on Piezoelectric Thin Films," *IEEE Transactions on Nanotechnology*, vol. 17, pp. 220–230, Mar. 2018.

[36] M. Schenk and S. D. Guest, "On zero stiffness," *Proceedings of the Institution of Mechanical Engineers, Part C: Journal of Mechanical Engineering Science*, vol. 228, pp. 1701–1714, July 2014. Publisher: IMECHE.

[37] K. Hoetmer, J. L. Herder, and C. J. Kim, "A Building Block Approach for the Design of Statically Balanced Compliant Mechanisms," in *Proceedings of ASME 2009 International Design Engineering Technical Conferences and Computers and Information in Engineering Conference*, pp. 313–323, American Society of Mechanical Engineers Digital Collection, July 2010.

[38] S. P. Beeby, M. J. Tudor, and N. M. White, "Energy harvesting vibration sources for microsystems applications," *Measurement Science and Technology*, vol. 17, no. 12, p. R175, 2006.

[39] E. Arroyo, A. Badel, F. Formosa, Y. Wu, and J. Qiu, "Comparison of electromagnetic and piezoelectric vibration energy harvesters: Model and experiments," *Sensors and Actuators A: Physical*, vol. 183, pp. 148–156, Aug. 2012.

[40] P. Muralt, R. G. Polcawich, and S. Trolier-McKinstry, "Piezoelectric Thin Films for Sensors, Actuators, and Energy Harvesting," *MRS Bulletin*, vol. 34, pp. 658–664, Sept. 2009.

[41] Y. Q. Fu, J. K. Luo, N. T. Nguyen, A. J. Walton, A. J. Flewitt, X. T. Zu, Y. Li, G. McHale, A. Matthews, E. Iborra, H. Du, and W. I. Milne, "Advances in piezoelectric thin films for acoustic biosensors, acoustofluidics and lab-on-chip applications," *Progress in Materials Science*, vol. 89, pp. 31–91, Aug. 2017.

[42] S. Du, Y. Jia, C. Zhao, G. A. J. Amaratunga, and A. A. Seshia, "A Nail-Size Piezoelectric Energy Harvesting System Integrating a MEMS Transducer and a CMOS SSHI Circuit," *IEEE Sensors Journal*, vol. 20, pp. 277–285, Jan. 2020. Conference Name: IEEE Sensors Journal.

[43] M. T. Todaro, F. Guido, V. Mastronardi, D. Desmaele, G. Epifani, L. Algieri, and M. De Vittorio, "Piezoelectric MEMS vibrational energy harvesters: Advances and outlook," *Microelectronic Engineering*, vol. 183-184, pp. 23–36, Nov. 2017.

[44] J. J. Parise, L. L. Howell, and S. P. Magleby, "Ortho-Planar Mechanisms," in *Proceedings of ASME 2000 International Design Engineering Technical Conferences and Computers and Information in Engineering*

Conference, pp. 1279–1286, American Society of Mechanical Engineers Digital Collection, Dec. 2020.

[45] J. J. Parise, L. L. Howell, and S. P. Magleby, "Ortho-planar linear-motion springs," *Mechanism and Machine Theory*, vol. 36, pp. 1281–1299, Nov. 2001.

[46] P. J. Pluimers, N. Tolou, B. D. Jensen, L. L. Howell, and J. L. Herder, "A Compliant On/Off Connection Mechanism for Preloading Statically Balanced Compliant Mechanisms," in *Proceedings of ASME 2012 International Design Engineering Technical Conferences and Computers and Information in Engineering Conference*, pp. 373–377, American Society of Mechanical Engineers Digital Collection, Sept. 2013.

[47] G. K. Ananthasuresh and L. L. Howell, "Mechanical Design of Compliant Microsystems—A Perspective and Prospects," *Journal of Mechanical Design*, vol. 127, pp. 736–738, Feb. 2005.

[48] M. Y. Barel, D. F. Machekposhti, J. L. Herder, N. Tolou, and M. Sitti, "Permanent Preloading by Acceleration for Statically Balancing MEMS Devices," in *2018 International Conference on Reconfigurable Mechanisms and Robots (ReMAR)*, pp. 1–11, June 2018.

[49] P. R. Kuppens, J. L. Herder, and N. Tolou, "Permanent Stiffness Reduction by Thermal Oxidation of Silicon," *Journal of Microelectromechanical Systems*, vol. 28, pp. 900–909, Oct. 2019. Conference Name: Journal of Microelectromechanical Systems.

[50] R. Xu, H. Akay, and S.-G. Kim, "Buckled MEMS Beams for Energy Harvesting from Low Frequency Vibrations," *Research*, vol. 2019, pp. 1–14, Aug. 2019.

[51] S. Beeby and N. M. White, *Energy Harvesting for Autonomous Systems*. Artech House, 2010.

[52] H. A. Sodano, D. J. Inman, and G. Park, "A review of power harvesting from vibration using piezoelectric materials," *Shock and Vibration Digest*, vol. 36, no. 3, pp. 197–206, 2004.

[53] G. D. Szarka, B. H. Stark, and S. G. Burrow, "Review of Power Conditioning for Kinetic Energy Harvesting Systems," *IEEE Transactions on Power Electronics*, vol. 27, pp. 803–815, Feb. 2012. Conference Name: IEEE Transactions on Power Electronics.

[54] Y. Tsujiura, E. Suwa, F. Kurokawa, H. Hida, and I. Kanno, "Reliability of vibration energy harvesters of metal-based PZT thin films," *Journal of Physics: Conference Series*, vol. 557, p. 012096, Nov. 2014.

[55] M. Okayasu, G. Ozeki, and M. Mizuno, "Fatigue failure characteristics of lead zirconate titanate piezoelectric ceramics," *Journal of the European Ceramic Society*, vol. 30, pp. 713–725, Feb. 2010.

[56] J. A. Brans, T. W. A. Blad, and N. Tolou, "A Review of Design Principles for Improved Mechanical Reliability of Cantilever Piezoelectric Vibration Energy Harvesters," in *2019 7th International Conference on Control, Mechatronics and Automation (ICCMA)*, pp. 408–415, Nov. 2019.

[57] J. A. Brans, T. W. A. Blad, and N. Tolou, "Reliability of Tapered Bimorph Piezoelectric Energy Harvesters - an Experimental Study," (Virtual, Online), 2021. (In-press).

[58] T. Blad and N. Tolou, "On the efficiency of energy harvesters: A classification of dynamics in miniaturized generators under low-frequency excitation," *Journal of Intelligent Material Systems and Structures*, vol. 30, pp. 2436–2446, Sept. 2019.

[59] C. B. Williams and R. B. Yates, "Analysis of a micro-electric generator for microsystems," *Sensors and Actuators A: Physical*, vol. 52, pp. 8–11, Mar. 1996.

[60] M. F. Daqaq, R. Masana, A. Erturk, and D. Dane Quinn, "On the Role of Nonlinearities in Vibratory Energy Harvesting: A Critical Review and Discussion," *Applied Mechanics Reviews*, vol. 66, pp. 040801–040801–23, May 2014.

[61] P. L. Green, E. Papatheou, and N. D. Sims, "Energy harvesting from human motion and bridge vibrations: An evaluation of current nonlinear energy harvesting solutions," *Journal of Intelligent Material Systems and Structures*, vol. 24, pp. 1494–1505, Aug. 2013.

[62] B. J. Bowers and D. P. Arnold, "Spherical, rolling magnet generators for passive energy harvesting from human motion," *Journal of Micromechanics and Microengineering*, vol. 19, no. 9, p. 094008, 2009.

[63] T. Galchev, E. E. Aktakka, and K. Najafi, "A Piezoelectric Parametric Frequency Increased Generator for Harvesting Low-Frequency Vibrations," *Journal of Microelectromechanical Systems*, vol. 21, pp. 1311–1320, Dec. 2012.

[64] H. Kulah and K. Najafi, "Energy Scavenging From Low-Frequency Vibrations by Using Frequency Up-Conversion for Wireless Sensor Applications," *IEEE Sensors Journal*, vol. 8, pp. 261–268, Mar. 2008.

[65] M. Geisler, S. Boisseau, M. Perez, P. Gasnier, J. Willemin, I. Ait-Ali, and S. Perraud, "Human-motion energy harvester for autonomous body area sensors," *Smart Materials and Structures*, vol. 26, no. 3, p. 035028, 2017.

[66] S. P. Pellegrini, N. Tolou, M. Schenk, and J. L. Herder, "Bistable vibration energy harvesters: A review," *Journal of Intelligent Material Systems and Structures*, vol. 24, pp. 1303–1312, July 2013.

[67] H. Liu, C. Lee, T. Kobayashi, C. J. Tay, and C. Quan, "A new S-shaped MEMS PZT cantilever for energy harvesting from low frequency vibrations below 30 Hz," *Microsystem Technologies*, vol. 18, pp. 497–506, Apr. 2012.

[68] E. Dechant, F. Fedulov, D. V. Chashin, L. Y. Fetisov, Y. K. Fetisov, and M. Shamonin, "Low-frequency, broadband vibration energy harvester using coupled oscillators and frequency up-conversion by mechanical stoppers," *Smart Materials and Structures*, vol. 26, no. 6, p. 065021, 2017.

[69] T. Galchev, H. Kim, and K. Najafi, "Micro Power Generator for Harvesting Low-Frequency and Nonperiodic Vibrations," *Journal of Microelectromechanical Systems*, vol. 20, pp. 852–866, Aug. 2011.

[70] W.-S. Huang, K.-E. Tzeng, M.-C. Cheng, and R.-S. Huang, "A silicon mems micro power generator for wearable micro devices," *Journal of the Chinese Institute of Engineers*, vol. 30, pp. 133–140, Jan. 2007.

[71] S. D. Moss, J. E. McLeod, I. G. Powlesland, and S. C. Galea, "A bi-axial magnetoelectric vibration energy harvester," *Sensors and Actuators A: Physical*, vol. 175, pp. 165–168, Mar. 2012.

[72] A. R. M. Foisal, C. Hong, and G.-S. Chung, "Multi-frequency electromagnetic energy harvester using a magnetic spring cantilever," *Sensors and Actuators A: Physical*, vol. 182, pp. 106–113, Aug. 2012.

[73] A. Munaz, B.-C. Lee, and G.-S. Chung, "A study of an electromagnetic energy harvester using multi-pole magnet," *Sensors and Actuators A: Physical*, vol. 201, pp. 134–140, Oct. 2013.

[74] M. Salauddin, M. A. Halim, and J. Y. Park, "A magnetic-spring-based, low-frequency-vibration energy harvester comprising a dual Halbach array," *Smart Materials and Structures*, vol. 25, no. 9, p. 095017, 2016.

[75] C. M. Saravia, J. M. Ramírez, and C. D. Gatti, "A hybrid numerical-analytical approach for modeling levitation based vibration energy harvesters," *Sensors and Actuators A: Physical*, vol. 257, pp. 20–29, Apr. 2017.

[76] A. Nammari, L. Caskey, J. Negrete, and H. Bardaweel, "Fabrication and characterization of non-resonant magneto-mechanical low-frequency vibration energy harvester," *Mechanical Systems and Signal Processing*, vol. 102, pp. 298–311, Mar. 2018.

[77] W. Liu, Adrien Badel, Fabien Formosa, Yipeng Wu, Nabil Bencheikh, and Amen Agbossou, "A wideband integrated piezoelectric bistable generator: Experimental performance evaluation and potential for real environmental vibrations," *Journal of Intelligent Material Systems and Structures*, vol. 26, pp. 872–877, May 2015.

[78] Y. Wang, Q. Zhang, L. Zhao, and E. S. Kim, "Non-Resonant Electromagnetic Broad-Band Vibration-Energy Harvester Based on Self-Assembled Ferrofluid Liquid Bearing," *Journal of Microelectromechanical Systems*, vol. 26, pp. 809–819, Aug. 2017.

[79] K. Ashraf, M. H. M. Khir, J. O. Dennis, and Z. Baharudin, "A wideband, frequency up-converting bounded vibration energy harvester for a low-frequency environment," *Smart Materials and Structures*, vol. 22, no. 2, p. 025018, 2013.

[80] S. Ju, S. H. Chae, Y. Choi, S. Lee, H. W. Lee, and C.-H. Ji, "A low frequency vibration energy harvester using magnetoelectric laminate composite," *Smart Materials and Structures*, vol. 22, no. 11, p. 115037, 2013.

[81] M. Han, Q. Yuan, X. Sun, and H. Zhang, "Design and Fabrication of Integrated Magnetic MEMS Energy Harvester for Low Frequency Applications," *Journal of Microelectromechanical Systems*, vol. 23, pp. 204–212, Feb. 2014.

[82] D. Miki, M. Honzumi, Y. Suzuki, and N. Kasagi, "Large-amplitude MEMS electret generator with nonlinear spring," in *2010 IEEE 23rd International Conference on Micro Electro Mechanical Systems (MEMS)*, pp. 176–179, Jan. 2010.

[83] M. Renaud, P. Fiorini, R. v. Schaijk, and C. v. Hoof, "Harvesting energy from the motion of human limbs: the design and analysis of an impact-based piezoelectric generator," *Smart Materials and Structures*, vol. 18, no. 3, p. 035001, 2009.

[84] M. A. Halim and J. Y. Park, "Theoretical modeling and analysis of mechanical impact driven and frequency up-converted piezoelectric energy harvester for low-frequency and wide-bandwidth operation," *Sensors and Actuators A: Physical*, vol. 208, pp. 56–65, Feb. 2014.

[85] K. Ashraf, M. H. Md Khir, J. O. Dennis, and Z. Baharudin, "Improved energy harvesting from low frequency vibrations by resonance amplification at multiple frequencies," *Sensors and Actuators A: Physical*, vol. 195, pp. 123–132, June 2013.

[86] Q. C. Tang, Y. L. Yang, and X. Li, "Bi-stable frequency up-conversion piezoelectric energy harvester driven by non-contact magnetic repulsion," *Smart Materials and Structures*, vol. 20, no. 12, p. 125011, 2011.

[87] P. Pillatsch, E. M. Yeatman, and A. S. Holmes, "A scalable piezoelectric impulse-excited energy harvester for human body excitation," *Smart Materials and Structures*, vol. 21, no. 11, p. 115018, 2012.

[88] M. A. Halim and J. Y. Park, "Modeling and experiment of a handy motion driven, frequency up-converting electromagnetic energy harvester using transverse impact by spherical ball," *Sensors and Actuators A: Physical*, vol. 229, pp. 50–58, June 2015.

[89] T. W. A. Blad, R. A. J. van Ostayen, and N. Tolou, "A method for tuning the stiffness of building blocks for statically balanced compliant ortho-planar mechanisms," *Mechanism and Machine Theory*, vol. 162, p. 104333, Aug. 2021.

[90] H. Dong, Y. Jia, Y. Hao, and S. Shen, "A novel out-of-plane MEMS tunneling accelerometer," *Sensors and Actuators A: Physical*, vol. 120, pp. 360–364, May 2005.

[91] S. He and R. B. Mrad, "Design, Modeling, and Demonstration of a MEMS Repulsive-Force Out-of-Plane Electrostatic Micro Actuator," *Journal of Microelectromechanical Systems*, vol. 17, pp. 532–547, June 2008. Conference Name: Journal of Microelectromechanical Systems.

[92] K. Tao, S. W. Lye, J. Miao, L. Tang, and X. Hu, "Out-of-plane electret-based MEMS energy harvester with the combined nonlinear effect from electrostatic force and a mechanical elastic stopper," *Journal of Micromechanics and Microengineering*, vol. 25, p. 104014, Sept. 2015. Publisher: IOP Publishing.

[93] N. Tolou, V. A. Henneken, and J. L. Herder, "Statically Balanced Compliant Micro Mechanisms (SB-MEMS): Concepts and Simulation," in *Proceedings of ASME 2010 International Design Engineering Technical Conferences and Computers and Information in Engineering Conference*, pp. 447–454, American Society of Mechanical Engineers Digital Collection, Mar. 2011.

[94] R. P. Middlemiss, A. Samarelli, D. J. Paul, J. Hough, S. Rowan, and G. D. Hammond, "Measurement of the Earth tides with a MEMS gravimeter," *Nature*, vol. 531, pp. 614–617, Mar. 2016.

[95] N. Tolou, P. Estevez, and J. L. Herder, "Collinear-Type Statically Balanced Compliant Micro Mechanism (SB-CMM): Experimental Comparison Between Pre-Curved and Straight Beams," in *Proceedings of ASME 2011 International Design Engineering Technical Conferences and Computers and Information in Engineering Conference*, pp. 113–117, American Society of Mechanical Engineers Digital Collection, June 2012.

[96] S. P. Timoshenko and J. M. Gere, *Theory of Elastic Stability*. Courier Corporation, June 2009.

[97] K. V. Singh and G. Li, "Buckling of functionally graded and elastically restrained non-uniform columns," *Composites Part B: Engineering*, vol. 40, pp. 393–403, July 2009.

[98] B. Camescasse, A. Fernandes, and J. Pouget, "Bistable buckled beam and force actuation: Experimental validations," *International Journal of Solids and Structures*, vol. 51, pp. 1750–1757, May 2014.

[99] P. Cazottes, A. Fernandes, J. Pouget, and M. Hafez, "Bistable Buckled Beam: Modeling of Actuating Force and Experimental Validations," *Journal of Mechanical Design*, vol. 131, Oct. 2009. Publisher: American Society of Mechanical Engineers Digital Collection.

[100] M. Mariello, T. W. A. Blad, V. M. Mastronardi, F. Madaro, F. Guido, U. Staufer, N. Tolou, and M. De Vittorio, "Flexible piezoelectric AlN transducers buckled through package-induced preloading for mechanical energy harvesting," *Nano Energy*, vol. 85, p. 105986, July 2021.

[101] M. Mariello, F. Guido, V. M. Mastronardi, M. T. Todaro, D. Desmaële, and M. De Vittorio, "Nanogenerators for harvesting mechanical energy conveyed by liquids," *Nano Energy*, vol. 57, pp. 141–156, Mar. 2019.

[102] J. Fang, X. Wang, and T. Lin, "Electrical power generator from randomly oriented electrospun poly(vinylidene fluoride) nanofibre membranes," *Journal of Materials Chemistry*, vol. 21, pp. 11088–11091, July 2011. Publisher: The Royal Society of Chemistry.

[103] X. Chen, S. Xu, N. Yao, and Y. Shi, "1.6 V Nanogenerator for Mechanical Energy Harvesting Using PZT Nanofibers," *Nano Letters*, vol. 10, pp. 2133–2137, June 2010.

[104] S. Bai, Q. Xu, L. Gu, F. Ma, Y. Qin, and Z. L. Wang, "Single crystalline lead zirconate titanate (PZT) nano/micro-wire based self-powered UV sensor," *Nano Energy*, vol. 1, pp. 789–795, Nov. 2012.

[105] P. Wang and H. Du, "ZnO thin film piezoelectric MEMS vibration energy harvesters with two piezoelectric elements for higher output performance," *Review of Scientific Instruments*, vol. 86, p. 075002, July 2015.

[106] C. B. Eom and S. Trolier-McKinstry, "Thin-film piezoelectric MEMS," *MRS Bulletin*, vol. 37, pp. 1007–1017, Nov. 2012.

[107] K. Wasa, T. Matsushima, H. Adachi, I. Kanno, and H. Kotera, "Thin-Film Piezoelectric Materials For a Better Energy Harvesting MEMS,"

Journal of Microelectromechanical Systems, vol. 21, pp. 451–457, Apr. 2012. Conference Name: Journal of Microelectromechanical Systems.

[108] S. S. Won, M. Sheldon, N. Mostovych, J. Kwak, B.-S. Chang, C. W. Ahn, A. I. Kingon, I. W. Kim, and S.-H. Kim, "Piezoelectric poly(vinylidene fluoride trifluoroethylene) thin film-based power generators using paper substrates for wearable device applications," *Applied Physics Letters*, vol. 107, p. 202901, Nov. 2015. Publisher: American Institute of Physics.

[109] G. F. Iriarte, J. G. Rodríguez, and F. Calle, "Synthesis of c-axis oriented AlN thin films on different substrates: A review," *Materials Research Bulletin*, vol. 45, pp. 1039–1045, Sept. 2010.

[110] K. Tonisch, V. Cimalla, C. Foerster, H. Romanus, O. Ambacher, and D. Dontsov, "Piezoelectric properties of polycrystalline AlN thin films for MEMS application," *Sensors and Actuators A: Physical*, vol. 132, pp. 658–663, Nov. 2006.

[111] E. Iborra, J. Olivares, M. Clement, J. Capilla, V. Felmetsger, and M. Mikhov, "Piezoelectric and electroacoustic properties of V-doped and Ta-doped AlN thin films," in *2013 Joint European Frequency and Time Forum International Frequency Control Symposium (EFTF/IFC)*, pp. 262–265, July 2013.

[112] K. Tonisch, V. Cimalla, C. Foerster, D. Dontsov, and O. Ambacher, "Piezoelectric properties of thin AlN layers for MEMS application determined by piezoresponse force microscopy," *physica status solidi c*, vol. 3, no. 6, pp. 2274–2277, 2006. _eprint: https://onlinelibrary.wiley.com/doi/pdf/10.1002/pssc.200565123.

[113] F. Guido, A. Qualtieri, L. Algieri, E. D. Lemma, M. De Vittorio, and M. T. Todaro, "AlN-based flexible piezoelectric skin for energy harvesting from human motion," *Microelectronic Engineering*, vol. 159, pp. 174–178, June 2016.

[114] S. Petroni, F. Rizzi, F. Guido, A. Cannavale, T. Donateo, F. Ingrosso, V. M. Mastronardi, R. Cingolani, and M. D. Vittorio, "Flexible AlN flags for efficient wind energy harvesting at ultralow cut-in wind speed," *RSC Advances*, vol. 5, pp. 14047–14052, Jan. 2015. Publisher: The Royal Society of Chemistry.

[115] V. M. Mastronardi, F. Guido, M. De Vittorio, and S. Petroni, "Flexible Force Sensor Based on C-axis Oriented Aluminum Nitride," *Procedia Engineering*, vol. 87, pp. 164–167, Jan. 2014.

[116] S. Petroni, C. L. Tegola, G. Caretto, A. Campa, A. Passaseo, M. D. Vittorio, and R. Cingolani, "Aluminum Nitride piezo-MEMS on polyimide

flexible substrates," *Microelectronic Engineering*, vol. 88, pp. 2372–2375, Aug. 2011.

[117] S. Petroni, F. Guido, B. Torre, A. Falqui, M. T. Todaro, R. Cingolani, and M. D. Vittorio, "Tactile multisensing on flexible aluminum nitride," *Analyst*, vol. 137, pp. 5260–5264, Oct. 2012. Publisher: The Royal Society of Chemistry.

[118] L. Lamanna, F. Rizzi, F. Guido, L. Algieri, S. Marras, V. M. Mastronardi, A. Qualtieri, and M. D. Vittorio, "Flexible and Transparent Aluminum-Nitride-Based Surface-Acoustic-Wave Device on Polymeric Polyethylene Naphthalate," *Advanced Electronic Materials*, vol. 5, no. 6, p. 1900095, 2019.

[119] A. Iqbal and F. Mohd-Yasin, "Reactive Sputtering of Aluminum Nitride (002) Thin Films for Piezoelectric Applications: A Review," *Sensors*, vol. 18, p. 1797, June 2018.

[120] M. Mariello, L. Fachechi, F. Guido, and M. De Vittorio, "Multifunctional sub-100um thickness flexible piezo triboelectric hybrid water energy harvester based on biocompatible AlN and soft parylene C-PDMS-Ecoflex," *Nano Energy*, vol. 83, p. 105811, May 2021.

[121] N. Jackson, L. Keeney, and A. Mathewson, "Flexible-CMOS and biocompatible piezoelectric AlN material for MEMS applications," *Smart Materials and Structures*, vol. 22, p. 115033, Oct. 2013. Publisher: IOP Publishing.

[122] T. von Buren, P. Mitcheson, T. Green, E. Yeatman, A. Holmes, and G. Troster, "Optimization of inertial micropower Generators for human walking motion," *IEEE Sensors Journal*, vol. 6, pp. 28–38, Feb. 2006. Conference Name: IEEE Sensors Journal.

[123] W. Liu, M. Han, B. Meng, X. Sun, X. Huang, and H. Zhang, "Low frequency wide bandwidth MEMS energy harvester based on spiral-shaped PVDF cantilever," *Science China Technological Sciences*, vol. 57, pp. 1068–1072, June 2014.

[124] A. A. Narasimulu, P. Zhao, N. Soin, K. Prashanthi, P. Ding, J. Chen, S. Dong, L. Chen, E. Zhou, C. D. Montemagno, and J. Luo, "Significant triboelectric enhancement using interfacial piezoelectric ZnO nanosheet layer," *Nano Energy*, vol. 40, pp. 471–480, Oct. 2017.

[125] H. Liu, F. Zeng, G. Tang, and F. Pan, "Enhancement of piezoelectric response of diluted Ta doped AlN," *Applied Surface Science*, vol. 270, pp. 225–230, Apr. 2013.

[126] M. S. Majdoub, P. Sharma, and T. Çağin, "Dramatic enhancement in energy harvesting for a narrow range of dimensions in piezoelectric

nanostructures," *Physical Review B*, vol. 78, p. 121407, Sept. 2008. Publisher: American Physical Society.

[127] J. Yan, M. Liu, Y. G. Jeong, W. Kang, L. Li, Y. Zhao, N. Deng, B. Cheng, and G. Yang, "Performance enhancements in poly(vinylidene fluoride)-based piezoelectric nanogenerators for efficient energy harvesting," *Nano Energy*, vol. 56, pp. 662–692, Feb. 2019.

[128] Z.-Z. Ong, V.-K. Wong, and J.-H. Ho, "Performance enhancement of a piezoelectric rain energy harvester," *Sensors and Actuators A: Physical*, vol. 252, pp. 154–164, Dec. 2016.

[129] Y. Qi, J. Kim, T. D. Nguyen, B. Lisko, P. K. Purohit, and M. C. McAlpine, "Enhanced Piezoelectricity and Stretchability in Energy Harvesting Devices Fabricated from Buckled PZT Ribbons," *Nano Letters*, vol. 11, pp. 1331–1336, Mar. 2011. Publisher: American Chemical Society.

[130] A. C. Wang, C. Wu, D. Pisignano, Z. L. Wang, and L. Persano, "Polymer nanogenerators: Opportunities and challenges for large-scale applications," *Journal of Applied Polymer Science*, vol. 135, no. 24, p. 45674, 2018.

[131] H. Shao, Z. Wen, P. Cheng, N. Sun, Q. Shen, C. Zhou, M. Peng, Y. Yang, X. Xie, and X. Sun, "Multifunctional power unit by hybridizing contact-separate triboelectric nanogenerator, electromagnetic generator and solar cell for harvesting blue energy," *Nano Energy*, vol. 39, pp. 608–615, Sept. 2017.

[132] C. R. Bowen, H. A. Kim, P. M. Weaver, and S. Dunn, "Piezoelectric and ferroelectric materials and structures for energy harvesting applications," *Energy & Environmental Science*, vol. 7, pp. 25–44, Dec. 2013.

[133] Z. Yang, S. Zhou, J. Zu, and D. Inman, "High-Performance Piezoelectric Energy Harvesters and Their Applications," *Joule*, vol. 2, pp. 642–697, Apr. 2018.

[134] L. Dong, C. Wen, Y. Liu, Z. Xu, A. B. Closson, X. Han, G. P. Escobar, M. Oglesby, M. Feldman, Z. Chen, and J. X. J. Zhang, "Piezoelectric Buckled Beam Array on a Pacemaker Lead for Energy Harvesting," *Advanced Materials Technologies*, vol. 4, no. 1, p. 1800335, 2019.

[135] J. Tao, X. He, S. Yi, and Y. Deng, "Broadband energy harvesting by using bistable FG-CNTRC plate with integrated piezoelectric layers," *Smart Materials and Structures*, vol. 28, p. 095021, Aug. 2019.

[136] N. Tolou, J. G. Sanchez, and J. L. Herder, "Statically balanced compliant micro mechanisms (SB-MEMS): a breakthrough in precision engineering," *Mikroniek: vakblad voor precisie-technologie*, vol. 6, pp. 20–25, 2010.

[137] L. Algieri, M. T. Todaro, F. Guido, V. Mastronardi, D. Desmaële, A. Qualtieri, C. Giannini, T. Sibillano, and M. De Vittorio, "Flexible Piezoelectric Energy-Harvesting Exploiting Biocompatible AlN Thin Films Grown onto Spin-Coated Polyimide Layers," *ACS Applied Energy Materials*, vol. 1, pp. 5203–5210, Oct. 2018.

[138] M. Mariello, F. Guido, V. M. Mastronardi, R. Giannuzzi, L. Algieri, A. Qualteri, A. Maffezzoli, and M. De Vittorio, "Reliability of Protective Coatings for Flexible Piezoelectric Transducers in Aqueous Environments," *Micromachines*, vol. 10, p. 739, Nov. 2019.

[139] J. Cheng, C.-s. Liu, S. Shang, D. Liu, W. Perrie, G. Dearden, and K. Watkins, "A review of ultrafast laser materials micromachining," *Optics & Laser Technology*, vol. 46, pp. 88–102, Mar. 2013.

[140] B. Luk'yanchuk, N. Bityurin, M. Himmelbauer, and N. Arnold, "UV-laser ablation of polyimide: from long to ultra-short laser pulses," *Nuclear Instruments and Methods in Physics Research Section B: Beam Interactions with Materials and Atoms*, vol. 122, pp. 347–355, Feb. 1997.

[141] X. Hu, F. Yang, M. Guo, J. Pei, H. Zhao, and Y. Wang, "Fabrication of polyimide microfluidic devices by laser ablation based additive manufacturing," *Microsystem Technologies*, vol. 26, pp. 1573–1583, May 2020.

[142] C. Zhang, L. Ding, L. Yang, Z. Yang, Z. Yang, and L. Zhang, "Influence of Shape and Piezoelectric-Patch Length on Energy Conversion of Bluff Body-Based Wind Energy Harvester," *Complexity*, vol. 2020, p. e3789809, July 2020.

[143] H. L. Dai, A. Abdelkefi, Y. Yang, and L. Wang, "Orientation of bluff body for designing efficient energy harvesters from vortex-induced vibrations," *Applied Physics Letters*, vol. 108, p. 053902, Feb. 2016.

[144] A. Roshko, "On the Wake and Drag of Bluff Bodies," *Journal of the Aeronautical Sciences*, vol. 22, pp. 124–132, Feb. 1955.

[145] T. Kármán, *Aerodynamics*. Cornell University Press, 1963.

[146] A. B. Atrah, M. S. Ab-Rahman, H. Salleh, M. Z. Nuawi, M. J. Mohd Nor, and N. B. Jamaludin, "Karman Vortex Creation Using Cylinder for Flutter Energy Harvester Device," *Micromachines*, vol. 8, p. 227, July 2017.

[147] S. F. Hoerner, "Fluid-dynamic drag," *Hoerner Fluid Dynamics*, 1965.

[148] P. Shen, L. Lin, Y. Wei, H. Dou, and C. Tu, "Vortex shedding characteristics around a circular cylinder with flexible film," *European Journal of Mechanics - B/Fluids*, vol. 77, pp. 201–210, Sept. 2019.

[149] S. Priya, "Modeling of electric energy harvesting using piezoelectric windmill," *Applied Physics Letters*, vol. 87, p. 184101, Oct. 2005.

[150] F. Chen, M. Jia, Y. She, Y. Wu, Q. Shen, and L. Zhang, "Mechanical behavior of AlN/Mo functionally graded materials with various compositional structures," *Journal of Alloys and Compounds*, vol. 816, p. 152512, Mar. 2020.

[151] G. Iriarte, J. Bjurstrom, J. Westlinder, F. Engelmark, and I. Katardjiev, "Synthesis of c-axis-oriented AlN thin films on high-conducting layers: Al, Mo, Ti, TiN, and Ni," *IEEE Transactions on Ultrasonics, Ferroelectrics, and Frequency Control*, vol. 52, pp. 1170–1174, July 2005.

[152] S. S. Chauhan, M. M. Joglekar, and S. K. Manhas, "Influence of Process Parameters and Formation of Highly c-Axis Oriented AlN Thin Films on Mo by Reactive Sputtering," *Journal of Electronic Materials*, vol. 47, pp. 7520–7530, Dec. 2018.

[153] A. T. Tran, H. Schellevis, H. T. M. Pham, C. Shen, and P. M. Sarro, "Influence of seed layer on crystallinity and orientation of pulsed — DC sputtered AlN thin-films for piezoelectric actuators," *Procedia Engineering*, vol. 5, pp. 886–889, Jan. 2010.

[154] G. Tang, B. Yang, C. Hou, G. Li, J. Liu, X. Chen, and C. Yang, "A piezoelectric micro generator worked at low frequency and high acceleration based on PZT and phosphor bronze bonding," *Scientific Reports*, vol. 6, p. 38798, Dec. 2016.

[155] W. Wu, H. Du, D. F. Wang, and T. Itoh, "Resonating Characterization of Piezoelectric Fibers Applicable to Flexible Self-powered Fabric," *Procedia Engineering*, vol. 120, pp. 1028–1031, Jan. 2015.

[156] S. Michelin and O. Doaré, "Energy harvesting efficiency of piezoelectric flags in axial flows," *Journal of Fluid Mechanics*, vol. 714, pp. 489–504, Jan. 2013.

[157] J. Zhang, J. Zhang, C. Shu, and Z. Fang, "Enhanced piezoelectric wind energy harvesting based on a buckled beam," *Applied Physics Letters*, vol. 110, p. 183903, May 2017.

[158] Y. Feng, L. Zhang, Y. Zheng, D. Wang, F. Zhou, and W. Liu, "Leaves based triboelectric nanogenerator (TENG) and TENG tree for wind energy harvesting," *Nano Energy*, vol. 55, pp. 260–268, Jan. 2019.

[159] S. Cui, Y. Zheng, J. Liang, and D. Wang, "Triboelectrification based on double-layered polyaniline nanofibers for self-powered cathodic protection driven by wind," *Nano Research*, vol. 11, pp. 1873–1882, Apr. 2018.

[160] L. Zhao and Y. Yang, "Toward Small-Scale Wind Energy Harvesting: Design, Enhancement, Performance Comparison, and Applicability," *Shock and Vibration*, vol. 2017, p. e3585972, Mar. 2017.

[161] H. Bi, B. Wang, Y. Huang, J. Zhou, and Z. Deng, "Nonlinear dynamic performance of buckled piezoelectric ribbon-substrate energy harvester," *Composite Structures*, vol. 261, p. 113570, Apr. 2021.

[162] T. W. A. Blad, R. A. J. van Ostayen, J. L. Herder, and N. Tolou, "Statically Balanced Compliant Ortho-Planar Mechanism for Low-Frequency Energy Harvesting," *Journal of Mechanical Design*, 2021. (In-press).

[163] A. Abdelkefi, N. Barsallo, L. Tang, Y. Yang, and M. R. Hajj, "Modeling, validation, and performance of low-frequency piezoelectric energy harvesters," *Journal of Intelligent Material Systems and Structures*, vol. 25, pp. 1429–1444, Aug. 2014.

[164] R. Tashiro, N. Kabei, K. Katayama, E. Tsuboi, and K. Tsuchiya, "Development of an electrostatic generator for a cardiac pacemaker that harnesses the ventricular wall motion," *Journal of Artificial Organs*, vol. 5, pp. 0239–0245, Dec. 2002.

[165] R. Tashiro, N. Kabei, K. Katayama, Y. Ishizuka, F. Tsuboi, and K. Tsuchiya, "Development of an Electrostatic Generator that Harnesses the Motion of a Living Body : Use of a Resonant Phenomenon," *JSME International Journal Series C Mechanical Systems, Machine Elements and Manufacturing*, vol. 43, pp. 916–922, Dec. 2000.

[166] A. Zurbuchen, A. Haeberlin, L. Bereuter, A. Pfenniger, S. Bosshard, M. Kernen, P. P. Heinisch, J. Fuhrer, and R. Vogel, "Endocardial Energy Harvesting by Electromagnetic Induction," *IEEE Transactions on Biomedical Engineering*, vol. 65, pp. 424–430, Feb. 2018.

[167] N. Jackson, O. Z. Olszewski, C. O'Murchu, and A. Mathewson, "Shock-induced aluminum nitride based MEMS energy harvester to power a leadless pacemaker," *Sensors and Actuators A: Physical*, vol. 264, pp. 212–218, Sept. 2017.

[168] N. Jackson, O. Z. Olszewski, C. O'Murchu, and A. Mathewson, "Ultralow-frequency PiezoMEMS energy harvester using thin-film silicon and parylene substrates," *Journal of Micro/Nanolithography, MEMS, and MOEMS*, vol. 17, p. 015005, Mar. 2018.

[169] B. Vysotskyi, F. Parrain, X. L. Roux, E. Lefeuvre, P. Gaucher, and D. Aubry, "Electrostatic vibration energy harvester using multimodal-shaped springs for pacemaker application," in *2018 Symposium on*

Design, Test, Integration Packaging of MEMS and MOEMS (DTIP), pp. 1–6, May 2018.

[170] A. Zurbuchen, A. Haeberlin, L. Bereuter, J. Wagner, A. Pfenniger, S. Omari, J. Schaerer, F. Jutzi, C. Huber, J. Fuhrer, and R. Vogel, "The Swiss approach for a heartbeat-driven lead- and batteryless pacemaker," *Heart Rhythm*, vol. 14, pp. 294–299, Feb. 2017.

[171] M. Ansari and M. A. Karami, "A sub-cc nonlinear piezoelectric energy harvester for powering leadless pacemakers," *Journal of Intelligent Material Systems and Structures*, vol. 29, pp. 438–445, Feb. 2018.

[172] Y. Ma, Q. Zheng, Y. Liu, B. Shi, X. Xue, W. Ji, Z. Liu, Y. Jin, Y. Zou, Z. An, W. Zhang, X. Wang, W. Jiang, Z. Xu, Z. L. Wang, Z. Li, and H. Zhang, "Self-Powered, One-Stop, and Multifunctional Implantable Triboelectric Active Sensor for Real-Time Biomedical Monitoring," Sept. 2016.

[173] Q. Zheng, H. Zhang, B. Shi, X. Xue, Z. Liu, Y. Jin, Y. Ma, Y. Zou, X. Wang, Z. An, W. Tang, W. Zhang, F. Yang, Y. Liu, X. Lang, Z. Xu, Z. Li, and Z. L. Wang, "In Vivo Self-Powered Wireless Cardiac Monitoring via Implantable Triboelectric Nanogenerator," June 2016.

[174] D. H. Kim, H. J. Shin, H. Lee, C. K. Jeong, H. Park, G.-T. Hwang, H.-Y. Lee, D. J. Joe, J. H. Han, S. H. Lee, J. Kim, B. Joung, and K. J. Lee, "In Vivo Self-Powered Wireless Transmission Using Biocompatible Flexible Energy Harvesters," *Advanced Functional Materials*, vol. 27, no. 25, p. 1700341, 2017.

[175] N. Li, Z. Yi, Y. Ma, F. Xie, Y. Huang, Y. Tian, X. Dong, Y. Liu, X. Shao, Y. Li, L. Jin, J. Liu, Z. Xu, B. Yang, and H. Zhang, "Direct Powering a Real Cardiac Pacemaker by Natural Energy of a Heartbeat," *ACS Nano*, vol. 13, pp. 2822–2830, Mar. 2019.

[176] H. Goto, T. Sugiura, Y. Harada, and T. Kazui, "Feasibility of using the automatic generating system for quartz watches as a leadless pacemaker power source," *Medical & Biological Engineering & Computing*, vol. 37, pp. 377–380, May 1999.

[177] L. Brancato, T. Weydts, W. Oosterlinck, P. Herijgers, and R. Puers, "Biocompatible Packaging of an Epicardial Accelerometer for Real-time Assessment of Cardiac Motion," *Procedia Engineering*, vol. 168, pp. 80–83, Jan. 2016.

[178] L. Brancato, T. Weydts, H. De Clercq, T. Dimiaux, P. Herijgers, and R. Puers, "Biocompatible Packaging and Testing of an Endocardial Accelerometer for Heart Wall Motion Analysis," *Procedia Engineering*, vol. 120, pp. 840–844, Jan. 2015.

[179] N. G. Stephen, "On energy harvesting from ambient vibration," *Journal of Sound and Vibration*, vol. 293, pp. 409–425, May 2006.

[180] J. Roos, T. W. A. Blad, and J. Spronck, "Benchmarking of a Vibration Energy Harvester with Real-world Acceleration Measurements," (Virtual, Online), 2021. (In-press).

[181] D. Reynolds, G. Z. Duray, R. Omar, K. Soejima, P. Neuzil, S. Zhang, C. Narasimhan, C. Steinwender, J. Brugada, M. Lloyd, P. R. Roberts, V. Sagi, J. Hummel, M. G. Bongiorni, R. E. Knops, C. R. Ellis, C. C. Gornick, M. A. Bernabei, V. Laager, K. Stromberg, E. R. Williams, J. H. Hudnall, and P. Ritter, "A Leadless Intracardiac Transcatheter Pacing System," *New England Journal of Medicine*, vol. 374, pp. 533–541, Feb. 2016.

[182] O. J. H. Grymyr, E. W. Remme, A. Espinoza, H. Skulstad, O. J. Elle, E. Fosse, and P. S. Halvorsen, "Assessment of 3D motion increases the applicability of accelerometers for monitoring left ventricular function," *Interactive Cardiovascular and Thoracic Surgery*, vol. 20, no. 3, pp. 329–337, 2015.

[183] E. W. Remme, L. Hoff, P. S. Halvorsen, E. Naerum, H. Skulstad, L. A. Fleischer, O. J. Elle, and E. Fosse, "Validation of cardiac accelerometer sensor measurements.," *Physiological measurement*, vol. 30, no. 12, pp. 1429–1444, 2009.

[184] M. R. Krogh, G. M. Nghiem, P. S. Halvorsen, O. J. Elle, O. J. Grymyr, L. Hoff, and E. W. Remme, "Gravity Compensation Method for Combined Accelerometer and Gyro Sensors Used in Cardiac Motion Measurements," *Annals of Biomedical Engineering*, vol. 45, no. 5, pp. 1292–1304, 2017.

[185] M. Vogel, M. R. Schmidt, S. B. Kristiansen, M. Cheung, P. A. White, K. Sorensen, and A. N. Redington, "Validation of myocardial acceleration during isovolumic contraction as a novel noninvasive index of right ventricular contractility: comparison with ventricular pressure-volume relations in an animal model," *Circulation*, vol. 105, pp. 1693–1699, Apr. 2002.

[186] M. Toyono, K. Harada, M. Tamura, F. Yamamoto, and G. Takada, "Myocardial acceleration during isovolumic contraction as a new index of right ventricular contractile function and its relation to pulmonary regurgitation in patients after repair of tetralogy of Fallot," *Journal of the American Society of Echocardiography: Official Publication of the American Society of Echocardiography*, vol. 17, pp. 332–337, Apr. 2004.

[187] A. D. Margulescu, D. E. Thomas, T. E. Ingram, V. D. Vintila, M. A. Egan, D. Vinereanu, and A. G. Fraser, "Can Isovolumic Acceleration Be

Used in Clinical Practice to Estimate Ventricular Contractile Function? Reproducibility and Regional Variation of a New Noninvasive Index," *Journal of the American Society of Echocardiography*, vol. 23, no. 4, 2010.

[188] S. L. Roche, M. Vogel, O. Pitknen, B. Grant, C. Slorach, C. Fackoury, D. Stephens, J. Smallhorn, L. N. Benson, P. F. Kantor, and A. N. Redington, "Isovolumic acceleration at rest and during exercise in children: Normal values for the left ventricle and first noninvasive demonstration of exercise-induced force-frequency relationships," *Journal of the American College of Cardiology*, vol. 57, no. 9, pp. 1100–1107, 2011.

[189] B. Cifra, L. Mertens, M. Mirkhani, C. Slorach, W. Hui, C. Manlhiot, M. K. Friedberg, and A. Dragulescu, "Systolic and Diastolic Myocardial Response to Exercise in a Healthy Pediatric Cohort," *Journal of the American Society of Echocardiography*, vol. 29, no. 7, pp. 648–654, 2016.

[190] L. B. Pauliks, M. Vogel, C. F. M, R. Ian Williams, N. Payne, A. N. Redington, and A. G. Fraser, "Regional Response of Myocardial Acceleration During Isovolumic Contraction During Dobutamine Stress Echocardiography: A Color Tissue Doppler Study and Comparison with Angiocardiographic Findings," tech. rep., 2005.

[191] A. T. T. Nguyen, F. Tjulkins, E. Knut, Aasmundtveit, N. Hoivik, L. Hoff, O. J. Grymyr, P. S. Halvorsen, and K. Imenes, "Packaging of a multifunctional implantable heart monitoring device," in *DTIP 2014 - Symposium on Design, Test, Integration and Packaging of MEMS/MOEMS*, Institute of Electrical and Electronics Engineers Inc., 2014.

[192] R. Andosca, T. G. McDonald, V. Genova, S. Rosenberg, J. Keating, C. Benedixen, and J. Wu, "Experimental and theoretical studies on MEMS piezoelectric vibrational energy harvesters with mass loading," *Sensors and Actuators A: Physical*, vol. 178, pp. 76–87, May 2012.

[193] P. Biswal, S. K. Kar, and B. Mukherjee, "Design and Optimization of High-Performance Through Hole Based MEMS Energy Harvester Using PiezoMUMPs," *Journal of Electronic Materials*, vol. 50, pp. 375–388, Jan. 2021.

[194] A. Cowen, G. Hames, K. Glukh, and B. Hardy, "PiezoMUMPs™ Design Handbook," p. 28.

[195] M. A. Hopcroft, W. D. Nix, and T. W. Kenny, "What is the Young's Modulus of Silicon?," *Journal of Microelectromechanical Systems*, vol. 19, pp. 229–238, Apr. 2010.

[196] J.-H. Zhao, T. Ryan, P. S. Ho, A. J. McKerrow, and W.-Y. Shih, "Measurement of elastic modulus, Poisson ratio, and coefficient of

thermal expansion of on-wafer submicron films," *Journal of Applied Physics*, vol. 85, pp. 6421–6424, May 1999.

[197] G. Carlotti, L. Doucet, and M. Dupeux, "Comparative study of the elastic properties of silicate glass films grown by plasma enhanced chemical vapor deposition," *Journal of Vacuum Science & Technology B: Microelectronics and Nanometer Structures Processing, Measurement, and Phenomena*, vol. 14, pp. 3460–3464, Nov. 1996.

[198] S. M. Spearing, "Materials issues in microelectromechanical systems (MEMS)," *Acta Materialia*, vol. 48, pp. 179–196, Jan. 2000.

[199] A. Numic, T. W. A. Blad, and F. van keulen, "Effect of matching buckling loads on post-buckling behavior in compliant mechanisms," in *Proceedings of ASME 2021 International Design Engineering Technical Conferences and Computers and Information in Engineering Conference IDETC/CIE2021*, 2021. (In-press).

[200] A. Numic, T. W. A. Blad, and F. van Keulen, "Stiffness Compensation Through Matching Buckling Loads in a Compliant Four-Bar Mechanism," *Journal of Mechanisms and Robotics*, vol. 14, Sept. 2021.

ACKNOWLEDGEMENTS

Although the PhD is a very individual journey, it can safely be said that thesis is a product of collaboration too. I have had the pleasure to work with many people and in this section I would like to acknowledge their contributions to this thesis. In the first place I want to thank my (co)promotors Just, Ron and Nima for giving me the opportunity to pursue a PhD and for their guidance and support along the way. I consider all of you excellent mentors from which I have learned a great deal. In particular I would like to thank Nima for his commitment to offer guidance and support even after he went to pursue a career outside of the university.

Secondly, I would like to thank the students with whom I have had the pleasure to work as a supervisor. Armin, Joeri, Luc, Paulus, Johan, Rutger, Max, Stefan, Kylian, Erik, Robin, Marsha, Rajiv, Stijn, Joep, your work has contributed greatly to this thesis, and even more so to my journey as a PhD. I'm happy to have had such a large number of students interested in my project, such that we could build a community in which we could share our enthusiasm and creativity.

Next up are my colleagues at the department of Precision and Microsystems Engineering. These include my direct colleagues from the Mechatronic System Design group, Davood, Freek, Joep, Stefan, Niranjan, Werner, Ad, Andres, Nima, both Jelles and both Alis, the scientific staff with whom I have shared the supervision of students or otherwise collaborated, Fred, Urs, Peter, Farbod, Murali, Hassan, Richard, Ivan, Jo, Alejandro, and the (technical) support staff on whom I could always count, Eveline, Gaby, Lisette, Patrick, Rob, Gideon, Bradley, Spiridon. I would like to thank all of you for being there for me during this journey and for all the help you gave me along the way.

Finally I would like to thank my friends and my family. In particular I would like to thank Marcel, Marlize, Koen, Emma, Peter, Annemieke, Jeroen and Elies. A final and most special word of thanks goes out to my partner Marit: thank you for your love and support during this journey, for pushing me to work hard to achieve my goals and for giving meaning to my work.

Thijs Willem Albert Blad
Delft, October 2021

CURRICULUM VITÆ

Thijs Willem Albert BLAD

19 - 04 - 1994 Born in Oranjestad (Aruba), The Netherlands.

EDUCATION

2006 – 2012 **VWO** Natuur en Techniek
Atheneum College Hageveld
Heemstede, The Netherlands

2012 – 2015 **B.Sc.** in Mechanical Engineering (Werktuigbouwkunde)
Delft Univeristy of Technology
Delft, The Netherlands

Minor in Healthcare for Engingeering Students
Medical Delta (Delft Univeristy of Technology, LUMC, Erasmus MC)
Delft, Leiden and Rotterdam, The Netherlands

2015 – 2017 **M.Sc.** in Mechanical Engineering
Delft Univeristy of Technology
Delft, The Netherlands
Specialization: Precision and Microsystems Engineering
Thesis: Vibration Energy Harvesting from Human Motion

2017 – 2021 **Ph.D.** in Precision and Microsystems Engineering
Delft Univeristy of Technology
Delft, The Netherlands
Thesis: Micro Energy Harvesting from Low-Frequency Vibrations
Promotor: Prof. dr. ir. J.L. Herder

AWARDS AND DISTINCTIONS

2015 **B.Sc.** Degree Cum Laude

2017 **M.Sc.** Degree Cum Laude

THESIS PROJECT OUTPUT

PATENTS

1. **T.W.A. Blad**, *A compliant structure*, Dutch Patent, Application Number. NL2028025 (Pending).

JOURNAL PUBLICATIONS

2. **T.W.A. Blad**, N. Tolou, *On the efficiency of energy harvesters: A classification of dynamics in miniaturized generators under low-frequency excitation*, Journal of Intelligent Material Systems and Structures **16**, 30 (2019).

3. **T.W.A. Blad**, R.A.J. van Ostayen, N. Tolou, *A method for tuning the stiffness of building blocks for statically balanced compliant ortho-planar mechanisms*, Mechanism and Machine Theory 126 (2021).

4. **T.W.A. Blad***, M. Mariello*, V.M. Mastronardi, F. Madaro, F. Guido, U. Staufer, N. Tolou, M. De Vittorio, *Flexible piezoelectric AlN transducers buckled through package-induced preloading for mechanical energy harvesting*, Nano Energy 85 (2021).

5. **T.W.A. Blad**, R.A.J. van Ostayen, J.L. Herder, N. Tolou, (In-press) *Statically Balanced Compliant Ortho-Planar Mechanism for Low-Frequency Energy Harvesting*, Journal of Mechanical Design, (2021).

6. **T.W.A. Blad***, J. Nijssen*, F. Broeren, B. Boogaard, S. Lampaert, S. van den Toorn, J. van den Dobbelsteen, *A Rapidly Deployable Test Suite for Respiratory Protective Devices in the COVID-19 Pandemic*, Applied Biosafety **3**, 25 (2020).

7. A. Numic, **T.W.A. Blad**, F. van Keulen, *Stiffness compensation through matching buckling loads in a compliant four-bar mechanism*, Journal of Mechanisms and Robotics,**2**, 14 (2021).

8. E. van de Wetering, **T.W.A. Blad**, R.A.J. van Ostayen, *A stiffness compensated piezoelectric energy harvester for low-frequency excitation*, Smart Materials and Structures **11**, 30 (2021).

CONFERENCE PAPERS

9. **T.W.A. Blad**, D. Farhadi Machekposhti, J.L. Herder, A.S. Holmes, N. Tolou, *Vibration Energy Harvesting from Multi-Directional Motion Sources*,

*Co-first author

International Conference on Manipulation, Automation and Robotics at Small Scales (MARSS), Nagoya, Japan (2018).

10. **T.W.A. Blad**, D. Farhadi Machekposhti, N. Tolou, *Design of a Motion Energy Harvester based on Compliant Mechanisms: a Bi-stable Frequency Up-converter Generator*, IFToMM World Congress on Mechanism and Machine Science, Krakow, Poland (2019).

11. J.A. Brans, **T.W.A. Blad**, N. Tolou, *A Review of Design Principles for Improved Mechanical Reliability of Cantilever Piezoelectric Vibration Energy Harvesters*, 7th International Conference on Control, Mechatronics and Automation (ICCMA), Delft, The Netherlands (2019).

12. P. Schaap, **T.W.A. Blad**, M.P. Lustig, F. Alijani, *Design of a Vibration Energy Harvester based on Coupled Oscillators*, 7th International Conference on Control, Mechatronics and Automation (ICCMA), Delft, The Netherlands (2019).

13. A. Numic, **T.W.A. Blad**, F. van Keulen, (In-press) *Effect of matching buckling loads on post-buckling behavior in compliant mechanisms*, ASME International Design Engineering Technical Conferences & Computers and Information in Engineering Conference (IDETC/CIE), Virtual conference (2021).

14. E. van de Wetering, **T.W.A. Blad**, R.A.J. van Ostayen, (In-press) *On the mechanical behavior in stiffness compensated piezoelectric beams - an experimental investigation towards energy harvesting*, ASME International Design Engineering Technical Conferences & Computers and Information in Engineering Conference (IDETC/CIE), Virtual conference (2021).

15. J. Roos, **T.W.A. Blad**, J.W. Spronck, (In-press) *Benchmarking of a Vibration Energy Harvester with Real-world Acceleration Measurements*, IEEE 30th International Symposium on Industrial Electronics (ISIE), Kyoto, Japan (2021).

16. J.A. Brans, **T.W.A. Blad**, T.R. Mahon, W.A. Groen, N.Tolou, (In-press) *Reliability of Tapered Bimorph Piezoelectric Energy Harvesters – an Experimental Study*, IEEE 30th International Symposium on Industrial Electronics (ISIE), Kyoto, Japan (2021).

17. K. van Puffelen, **T.W.A. Blad**, R.A.J. van Ostayen, *Tuning the dynamics of bistable mechanisms by introducing travel limits*, Proceedings of the XII International Conference on the Theory of Machines and Mechanisms, Librec, Czech republic (2021).

MSc THESIS PROJECTS SUPERVISED

- L. Hogervorst, *System design and control of a novel ocean wave energy converter array* (2019).
- P. Schaap, *Design of a Vibration Energy Harvester based on Coupled Oscillators* (2019).
- J.A. Brans, *Piezoelectric Vibrational Energy Harvesting: Mechanical reliability of piezoelectric cantilevers* (2020).
- J. Roos, *Correct examination of vibration energy harvester perfromance* (2020).
- A. Numic, *Manipulating post-buckled compliant mechanisms: Buckling mode interaction as a novel method of stiffness compensation* (2021).
- S.T. Molenaar, *Examination of large amplitude vibrations of a nonlinear oscillator for energy harvesting* (2021).
- E. van de Wetering, *Stiffness compensation for piezoelectric energy harvesting: Improving the efficiency at low-frequency vibrations* (2021).
- R. Bastiaanse, *Energy Harvesting for Pacemakers: Combining Cardiac Measurement Techniques to Improve Testing* (2021).
- M. Wouters, *On the efficiency of coupled vs uncoupled vibration energy harvesters under transient excitations* (2021).
- K. van Puffelen, *Design of travel limits for bistable vibration energy harvesting* (2021).
- R. Ham, *A plucking based frequency up-converted vibration energy harvesting method: Design and model of a new frequency up-converted energy harvesting method* (2021).
- M. Nieuwland, *Thesis not yet finished* (2021).
- R. Kapildewsing, *Thesis not yet finished* (2021).
- S. Rietmeijer, *Thesis not yet finished* (2021).
- J. Meij, *Thesis not yet finished* (2021).

BSc THESIS PROJECTS SUPERVISED

- M. de Jong, K. van Puffelen, J. Roos, E. van de Wetering, *Motion energy harvester optimization by implementing ferrofluid* (2018).
- K. van den Berg, M. Broeren, Y.V. Kipping, L.S. Omar, *Tuning the efficiency curve of a human motion energy harvester: going from translation to rotation* (2018).
- J.P. Bos, J.L.D. van Eesteren, T.S.W. Genis, H.A. Schaab, *The impact of impact characteristics on piezoelectric energy harvesters* (2019).
- E.A. Lock, F.C.J. Lycklama à Nijeholt, N. Korzilius, F.M.C. Kraakman, *Harvesting energy from a heartbeat motion: comparing two different piezoelectric energy harvesting systems* (2019).
- A. Sinke, L. Samuels, A. Soltész, A.D. Wassenaar, *A two-degree-of-freedom piezoelectric energy harvester using impact-based frequency up-conversion* (2020).
- A. Detailleur, H.L.J. Van Even, P.C. de Groot, S.R. de Leeuw, *Modelling the*

characteristics of a quasi-zero stiffness vibration energy harvester utilising fixed-fixed Euler buckled beams (2020).

- G. de Bakker, N.M. Beaufort, A.H. Bom, H.J.H.M. van Brandenburg, M. Jankie, *Manipulating the stiffness of post-buckled flexures by tuning the boundary conditions* (2021).
- P.V.M. van den Bent, A.E. Koryakin, J. Wijnja, R.P. Breure, *Pigeon-powered GPS Tracking using Energy Harvester* (2021).

SUMMARY OF RESEARCH OUTPUT

- 1 patent pending
- 7 journal papers published/accepted
- 9 conference papers published/accepted
- 2 unsubmitted manuscripts/chapters
- 11 MSc students supervised (4 additional still being supervised)
- 8 BSc thesis groups supervised